



**Laser Image Cytometer  
for Analysis of Circulating Tumor Cells**



**Frederik Schreuder**



Laser Image Cytometer for Analysis of Circulating Tumor Cells

Frederik Schreuder





# LASER IMAGE CYTOMETER FOR ANALYSIS OF CIRCULATING TUMOR CELLS

Frederik Schreuder

## **Promotiecommissie**

Prof. dr. ing. M. Wessling	Universiteit Twente (voorzitter)
Prof. dr. J. Greve	Universiteit Twente (Promotor)
Prof. dr. L.W.M.M. Terstappen	Universiteit Twente (Promotor)
Prof. dr. C.G. Figdor	Universiteit Twente
Prof. dr. A.G.J.M. van Leeuwen	Universiteit Twente
Prof. dr. D. Lohse	Universiteit Twente
Prof. dr. med. K. Pantel	Universitätsklinikum Hamburg-Eppendorf
Prof. dr. H.J. Tanke	Universiteit Leiden

## **Acknowledgement**

This research was carried out at the Biophysical Engineering Group of the University of Twente, Enschede, The Netherlands in collaboration with Immunicon Corp., Huntingdon Valley, PA, USA.

## **Cover illustration**

Brighfield and fluorescent image of a whole blood sample spiked with SKBR-3 breast cancer tumor cells, illustrating the presence of tumors cells in the blood.

F. Schreuder

LASER IMAGE CYTOMETER FOR ANALYSIS OF CIRCULATING TUMOR CELLS

Proefschrift Universiteit Twente

ISBN 978-90-365-2610-4

Copyright © F. Schreuder, 2008

Printed by Wöhrmann Print Service, Zutphen, The Netherlands, 2008

# LASER IMAGE CYTOMETER FOR ANALYSIS OF CIRCULATING TUMOR CELLS

## PROEFSCHRIFT

ter verkrijging van  
de graad van doctor aan de Universiteit Twente,  
op gezag van de rector magnificus,  
prof.dr. W.H.M. Zijm,  
volgens besluit van het College voor Promoties  
in het openbaar te verdedigen  
op vrijdag 1 februari 2008 om 16.45 uur

door

**Frederik Schreuder**

geboren op 4 november 1975  
te Rijssen



**Dit proefschrift is goedgekeurd door:**

Prof. dr. J. Greve (Promotor)

Prof. dr. L.W.M.M. Terstappen (Promotor)

**Voor Nienke en mijn ouders**





# Contents

<b>1</b>	<b>Part I Introduction.....</b>	<b>1</b>
<b>1.1</b>	<b>Introduction cell analysis .....</b>	<b>3</b>
1.1.1	Introduction.....	3
	Blood.....	3
	Cancer.....	4
	Circulating tumor cells (CTCs).....	4
	CTC recognition and characterization.....	6
1.1.2	CTC enumeration – Flow cytometry.....	9
	Introduction.....	9
	Flow cytometric CTC analysis.....	10
1.1.3	CTC enumeration– Image cytometry.....	12
	Introduction.....	12
	Image cytometry and CTC detection.....	12
	CellTracks analyzer II.....	13
	CellTracks TDI.....	13
1.1.4	CTC Analysis and enrichment.....	14
	Immuno magnetic enrichment.....	15
	Fluorescent labeling.....	16
	Sample cartridge.....	16
1.1.5	The CellTracks Project.....	17
	Project objective.....	17
	The initial CellTracks.....	17
	TDI.....	18
	Achromatic lens.....	18
	Microscope objective.....	18
	Cell alignment.....	19
	No Cell alignment.....	20
	CellTracks TDI.....	20
<b>2</b>	<b>Part II Instrumentation .....</b>	<b>23</b>
<b>2.1</b>	<b>Instrument – Hardware.....</b>	<b>25</b>
2.1.1	Introduction.....	25
2.1.2	Optical layout.....	26
	Microscope objective.....	27
	Detection efficiency.....	28
	Total detection efficiency.....	28
2.1.3	Excitation.....	30
	Spectra.....	30
	Irradiance.....	31
2.1.4	Beam homogenizing.....	32

Introduction .....	32
Beam homogenizer optics .....	33
Beam profile .....	34
2.1.5 TDI Imaging .....	36
Introduction .....	36
CCD camera .....	36
Comparison TDI and frame transfer imaging .....	37
TDI scanning .....	39
TDI scan speed .....	40
Nonuniformity reduction .....	40
TDI image degradation .....	41
Modulation transfer function .....	42
2.1.6 Scanning system .....	45
Position control .....	45
Focus control .....	47
Counter .....	48
Stage-camera synchronization .....	49
Integration time .....	51
<b>2.2 Instrument – Control .....</b>	<b>53</b>
2.2.1 Introduction .....	53
2.2.2 Software control .....	53
TDI Measurement .....	55
Preview image .....	58
2.2.3 Feed forward steering and focusing .....	59
Introduction .....	59
Feed forward .....	59
TDI Focus method .....	60
Focus score .....	62
Multi-camera control .....	64
Auto focus .....	64
2.2.4 Data analysis .....	65
Introduction .....	65
Image analysis of rare cells .....	65
Image analysis triggering (A) .....	66
Image analysis measuring (B) .....	66
Image analysis displaying (C) .....	69
2.2.5 3D Imaging .....	69
Deconvolution .....	70
<b>2.3 Instrument – Characterization .....</b>	<b>71</b>
2.3.1 Theory: Signal to noise ratio (SNR) .....	71
Photon noise .....	71
Readout noise .....	71
Dark current noise .....	72
Background noise .....	72

Signal to noise ratio .....	73
Integration time .....	73
2.3.2 Theory: Dynamic range/Detection limit .....	74
Detection limit .....	75
Dynamic range .....	75
2.3.3 Theory: Fluorescence emission .....	77
Kinetic behavior .....	79
Fluorescence signal .....	79
Typical values .....	81
2.3.4 Signal throughput .....	81
2.3.5 Measurements: Noise .....	82
Noise factors for CTC samples .....	82
Noise and images .....	84
2.3.6 Measurements: Bleaching and SNR .....	86
Bleaching .....	86
Signal to noise ratio (SNR) .....	87
2.3.7 Measurements: Sensitivity, linearity and dynamic range .....	88
Sensitivity and dynamic range .....	88
Linearity and system variation .....	91
2.3.8 Optimal scan speed and acquisition times .....	92
Optimal scan speed .....	92
Acquisition time .....	93
Reducing overhead time .....	94
Reducing acquisition time .....	94
2.3.9 Specificity of CTC Identification .....	96
Identification by specific probes .....	96
Classification of CTCs by size and staining pattern .....	96
<b>3 Part III Applications .....</b>	<b>101</b>
<b>3.1 Characterization of Circulating Tumor Cells by Image Cytometry .....</b>	<b>103</b>
3.1.1 Summary .....	103
3.1.2 Introduction .....	103
3.1.3 Materials and methods .....	104
Sample preparation .....	104
CellTracks Analyzer II .....	104
CellTracks TDI analyzer .....	104
3.1.4 Results .....	106
Images of events after immunomagnetically enrichment for EpCAM expression ..	106
CellTracks TDI data analysis .....	107
Comparison of CTC analysis by CellTracks and CellTracks TDI .....	110
3.1.5 Discussion .....	114
<b>3.2 Identification of aneuploidy in Circulating Tumor Cells by a Laser Image Cytometer .....</b>	<b>117</b>
3.2.1 Summary .....	117



3.2.2	Introduction.....	117
3.2.3	Materials and methods .....	118
	Cell Spiking.....	118
	Tumor cell isolation and staining .....	118
	Tumor Cell Analysis by CellTracks TDI.....	118
	Sample preparation for FISH analysis.....	119
	Enumeration of FISH probes by CellTracks TDI.....	120
	Analysis of reexamined events.....	120
3.2.4	Results.....	120
	Identification of SKBR cells.....	120
	Revisiting events of interest .....	122
	Revisiting events for evaluation of FISH results .....	123
	Assessment of aneuploidy .....	126
3.2.5	Discussion.....	126
<b>3.3</b>	<b>Qdots as an alternative labeling strategy for Circulating Tumor Cell characterization.....</b>	<b>129</b>
3.3.1	Summary.....	129
3.3.2	Introduction.....	129
3.3.3	Materials and methods .....	130
	Bead labeling.....	130
	Cell Spiking.....	130
	Qdot labeling of MCF-7 and SKBR-3cells.....	130
	Imaging by CellTracks TDI.....	130
3.3.4	Results.....	131
	Qdot Crosstalk.....	131
	Qdot labeling of cells.....	133
3.3.5	Discussion.....	135
<b>4</b>	<b>Conclusions and outlook.....</b>	<b>137</b>
<b>4.1</b>	<b>Conclusions.....</b>	<b>137</b>
	CellTracks TDI.....	137
	Automated scanning and image analysis .....	137
	CTC characterization.....	138
	Reexamination.....	138
<b>4.2</b>	<b>Outlook.....</b>	<b>138</b>
	Illumination .....	138
	Ferrofluid.....	139
	Alignment structures .....	139
	Parallel Multi Color Setup.....	139
	Dynamic focusing.....	140
	Multi probe fluorescent assay.....	140
	Cell removal .....	140

<b>References .....</b>	<b>141</b>
<b>Summary .....</b>	<b>147</b>
<b>Samenvatting.....</b>	<b>149</b>
<b>Nawoord .....</b>	<b>151</b>
<b>Curriculum Vitae.....</b>	<b>153</b>





# Part I

# Introduction



# 1.1 Introduction cell analysis

## 1.1.1 Introduction

### *Blood*

Blood analysis plays an important role in the diagnosis of many illnesses. This is due to the different functions blood has in the body. Blood is the long distance mass transport medium of the body. It transports many elements and plays a role in body temperature regulation. It is a major component of the human body, the amount of blood forms in the order of 8 % of the total body mass.

Key components of blood are: Plasma mainly composed of water, blood proteins, and inorganic electrolytes. The cellular constituents (Figure 1.1.1) fulfill specific tasks.

Peripheral Blood Cells		
Cell Number	Cell Type	Cell Frequency (WBC)
$10^6$ ml	Erythrocytes	1 in $10^{-2}$
$10^5$ ml	Platelets	1 in $10^{-1}$
$10^4$ ml	Reticulocytes	1 in $10^0$
$10^3$ ml	Neutrophils	1 in $10^1$
$10^2$ ml	Lymphocytes	1 in $10^2$
$10^1$ ml	Monocytes	1 in $10^3$
$10^0$ ml	Eosinophils	1 in $10^4$
$10^2$ ml	Basophils	1 in $10^5$
$10^1$ ml	CD34 <sup>+</sup> Cells	1 in $10^6$
$10^0$ ml	Nucleated Erythrocytes	1 in $10^7$
$10^2$ L	CD34 <sup>+</sup> CD38 <sup>-</sup> Cells	1 in $10^8$
$10^1$ ml	Epithelial Cell Derived Tumor Cells	1 in $10^7$
$10^0$ ml		1 in $10^8$

**Figure 1.1.1** Frequency of cell types in peripheral blood: Tumor cells are extremely rare.

Erythrocytes take care of the essential oxygen transport; platelets or thrombocytes are responsible for blood clotting. Leukocytes (neutrophils, lymphocytes, monocytes, eosinophils, and basophils) are the basis of the immune system. The number of cells in the different subclasses of leukocytes in blood is very

informative as an indicator of disease. It is therefore common practice in hospitals to analyze the frequency of cellular components in blood to assist in diagnosis. Besides the typical blood cells, some rare cells may be present in the (peripheral) bloodstream, e.g. cells of the baby in a pregnant woman. In this thesis we will focus on the analysis of Circulating Tumor Cells (CTCs) that may be present in the blood of cancer patients.<sup>1-2</sup>

## ***Cancer***

In the last 25 years, many advances were made in cancer research. Nowadays tumors can often early be detected and located in the body and sometimes the cancer can be treated in a way that leads to complete recovery. The stage of the tumor and early diagnosis are important aspects for the chance to survive. For this purpose, sensitive and specific techniques are required to detect and follow the stage of the tumor. Nowadays tumor cells in the body can be detected and staged by biopsy, blood screening or MRI/CT imaging techniques. These techniques are very important, yet they have their limitations. Preferably one would like to have a system that can follow the disease status on a regular basis. This would create the option to react quickly on changes in the disease status and would make a better planning for the treatment possible.

## ***Circulating tumor cells (CTCs)***

The “invasive behavior” of tumor cells is the hallmark for cancer related death. Patients mainly die due to secondary tumors and not directly from the primary tumor. This means that the tumor cells have to migrate from one place in the body to a different one. J.C.A. Récamier<sup>3</sup> first postulated this metastatic behavior in 1829. Malignant cells leave a primary tumor, penetrate into lymphatic- and blood vessels, and circulate through the bloodstream. The Reticuloendothelial system filters out these cells, but some may metastasize into healthy tissues elsewhere in the body and form distant tumors. The presence of these circulating tumor cells (CTCs) was first described by T.R. Ashworth<sup>4</sup> in 1869. He noted the presence of cells similar to the tumor in the blood after death. According to Paget's ‘seed and soil’ hypothesis (1889), the metastatic process is a highly inefficient one. To metastasize in a distant location it has to complete the entire cascade of the metastatic process as shown in figure 1.1.2. Increasing tumor growth is initially assisted by angiogenesis to obtain new blood vessels and supply the tumor with nutrients and oxygen. During tumor growth the cells undergo several genetic mutations which may give them the capacity to loose the cell to cell adhesion and detach from the surrounding extracellular matrix (ECM). As a consequence tumor cells may enter the blood stream (intravasation). It is estimated from model systems that 10<sup>6</sup> tumor cells/g tumor tissue enter daily into the blood stream. However, a tumor cell has to survive in the blood in order to metastasize. In the blood they can die due to necrosis induced by the shear stress of the vessel walls

and apoptosis (programmed cell death) induced by anoikis. Furthermore these cells are also attacked by the immune system. Therefore, most tumor cells do not survive and die during this journey.

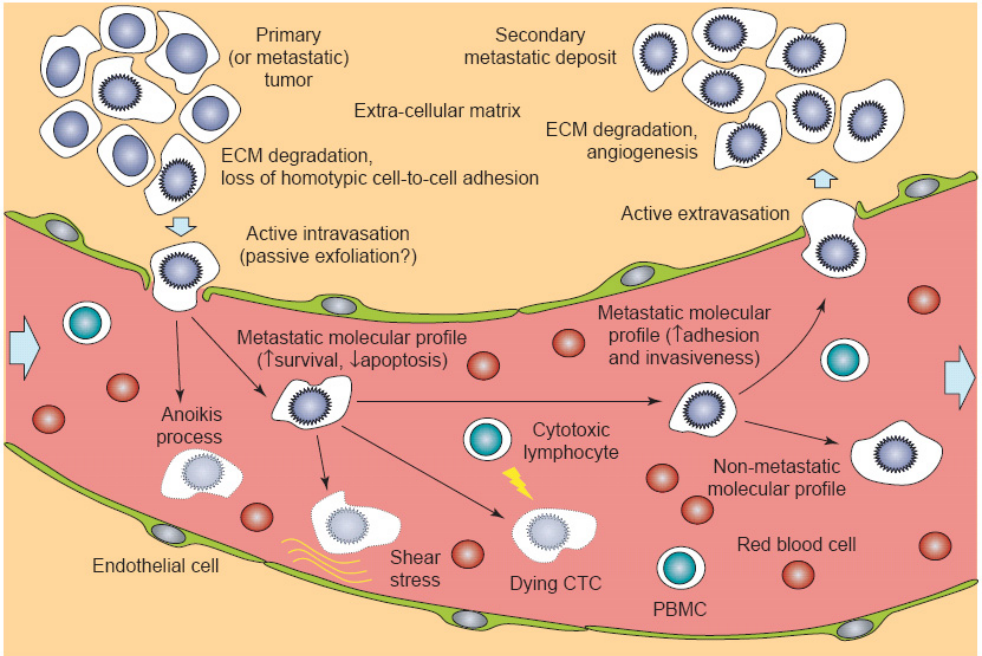


**Figure 1.1.2** The metastatic process is highly inefficient; most tumor cells do not survive. To generate a metastatic deposit the cell should have a metastatic molecular profile to complete the entire cascade. (Source image: Trends in Molecular Medicine, Simone Mocellin, vol.12 No.3 March 2006)

However some tumor cells with a metastatic molecular profile may survive and exit the bloodstream entering healthy tissue. These tumor cells may be present as isolated tumor cells or as a small cluster of tumor cells resistant to apoptosis. Some remain in dormancy for years with a limited proliferation where others proliferate quickly and form a secondary tumor. These properties also explain the recurrence of cancer many years after radical removal of the primary tumor even without any clinical or histopathological signs of metastasis.

The metastatic proliferating CTCs pose a great threat to a patient. Detection and characterization of these circulating tumor cells may therefore lead to a better planning for treatment of the disease. It may lead to development of a strong sensitive tool, a “blood biopsy”, for prognosis, anti-cancer drug development and personal cancer therapy. Furthermore, blood draw can be performed frequently and provides limited patient compliance.

This has led to several studies about the enumeration of CTCs<sup>5-12</sup>. From these studies it is clear that CTCs have a prognostics value. For breast- and prostate cancer patients it is shown that the number of CTCs correlates with disease status and overall survival of patients<sup>13-18</sup>. Furthermore the studies show that the specificity of CTC detection is ~100% whereas the false- positive rate among healthy patients is extremely low.

Several difficulties and contra dictionary results exist however among the studies. The biological significance of CTC biology is therefore still debated. The conflicting results among the studies may be accounted for in several ways. A major aspect is a high degree of variability among the studies. The tumor type, stage of disease, timing of blood draw (before and/or after treatment) varies for these studies. Furthermore different technologies and platforms are used for CTC detection. Some use PCR based methods (different/multiple primer targets) where others use a cytometric approach (Different cell enrichment procedures/multiple markers/CTC criteria, etc.).

It is therefore essential for proper CTC enumeration to use a highly standardized method with high sensitivity and specificity. Typical, peripheral blood contains on average 5 million erythrocytes, 250.000 thrombocytes and 7000 leukocytes per  $\mu\text{l}$ . CTCs are in this environment extremely rare and are usually present in very low frequencies (1 per ml), degenerate fast and a substantial population of the detected CTCs is apoptotic.<sup>19,20</sup> Due to the low number of CTCs each single CTC in a sample should be detected and errors can not be tolerated. Therefore enrichment of the sample is necessary with a well defined and highly automated labeling and selection protocol. A detailed description will be given later in this chapter.

### ***CTC recognition and characterization***

A wide variety of analysis methods has been developed to determine the cellular composition of blood. Typically, specific CTC detection methods can be classified into two different classes: The Reverse-Transcriptase Polymerase Chain Reaction<sup>5,21</sup> (RT-PCR) based ones and the cytometric methods. RT-PCR is the most widely used method for CTC detection. It uses DNA or mRNA isolation to amplify specific gene(s) of interest. This gives the ability to determine quantitatively the expression level of a specific gene. The method can detect one CTC in 1-10 ml of blood. However to detect CTCs a highly specific marker gene for a tumor cell is required and detection is limited by illegitimate low-level transcription of the corresponding genes in normal cells. A drawback of this method is that the cells are lost in such an approach and morphological data is not obtained. Although the method is gene specific, it doesn't discriminate between free nucleic acids or nucleic acids from intact or apoptotic CTCs.

Our method is a cytometric approach. For this discussion and the rest of the thesis I will focus on cytometric detection and characterization of tumor cells of epithelial origin. These are the majority of most common occurring cancer types.

Cytometric approaches have the advantage that from a sample, each individual event or cell can be characterized and that morphological information is obtained. To this end, these methods use labeling techniques and brightfield imaging to detect and characterize circulating tumor cells. To recognize CTCs, antibodies are used against epitopes that are commonly expressed on cells of epithelial origin. These cells should not occur in the blood stream and they are selected as Circulating Tumor Cells. That this is indeed a valid identification is justified by the fact that the false-positive rate among healthy donors is extremely low as was mentioned before. Cytokeratins are cytoskeleton proteins present in cells of epithelial origin and are not present in blood or blood cells. Typically, one applies multiple types of anti-cytokeratin antibodies with a fluorescent label for identification. To increase specificity of the CTC detection a negative immunofluorescent marker CD45 is used to label all leukocytes in the sample. This improves the discrimination of the CTCs from blood cells. The nucleus of the cells is stained with a nucleic acid dye to determine the DNA content. This assists to identify a specific event as a cellular object and to discern it from debris or other artifacts. Furthermore it may already indicate cancer related aneuploidy by means of an increase or decrease of DNA content. Besides positive/negative labeling of CTCs, the staining pattern for these labels also gives additional information about the morphology of a specific event. Cells have a typical round to oval morphology and for CTCs the size may vary from 4 to 40 micron. Leukocytes in contrast vary from 6 to 11 micron. They are in most cases slightly smaller than a CTC. Another aspect for identification of a cell is that the nucleus is surrounded by the cytoskeleton. CTCs tend to have a relatively large ratio between the cytoplasm/nucleus sizes. All the mentioned aspects above are taken into account to classify a specific event as a CTC or a specific new subclass. Typically a whole range of cellular objects related to CTCs can be detected.<sup>22</sup> Detected events range from small apoptotic bodies to intact CTCs. Some cells show more or less specific cellular staining patterns such as punctuated cytokeratin staining, cell/nucleus shrinkage, nuclear condensation and fragmentation which are all signs of apoptosis and cause a large heterogeneity among the detected CTCs.

Besides these characteristics, further identification and characterization of a CTC is possible by labeling specific antigens or apoptosis related markers<sup>23-25</sup>. Antigen density of tumor related markers on CTCs can be determined with the use of fluorescent probes conjugated against specific monoclonal antibodies such as Her2/neu, EGFr, MUC-1, IGF1R-1, and Bcl-2. These parameters may give valuable information about a specific tumor and relevant information regarding the anti-cancer therapy.

Apart from immunofluorescent methods, a different powerful tool applicable to cytometric identification is fluorescent in situ hybridization (FISH). In this method a specific gene of interest is labeled. It gives the possibility to measure genetic abnormalities and subtle alterations in DNA, as may appear in tumor cells.<sup>26,27</sup>

With our system we can determine a change in the number of chromosomes (aneuploidy) and over-expression, translocation and deletion of specific genes. In figure 1.1.3 a breast cancer tumor cell image is shown. It shows a typical tumor cell with a clear nucleus surrounded by cytokeratin. In this image the cytokeratin is colored green and the nucleus is colored blue. Furthermore chromosome Xq12 is labeled with a gene specific FISH probe (Red dots) which shows an abnormal copy number of 3 times chromosome X.

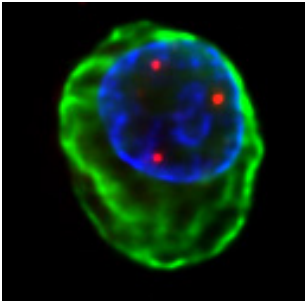


**Figure 1.1.3** Breast cancer tumor cells (SKBR-3) labeled in green for cytokeratin which is specific for cells of epithelial origin. The cell nucleus stains blue fluorescent with the nuclear acid dye DAPI. The red dots in the image are gene specific probes for Xq12 and indicate that this particular cell has an abnormal copy number three for chromosome X.

As indicated, several morphological parameters and a broad set of labeling techniques can be used to identify and characterize CTCs. The applicability and combined use of these techniques is however limited and depends on the cytometric analysis platform. In the next paragraph the traditional cell analysis platform, flow cytometry, will be compared to image cytometry. The latter may be more specific, but also has its drawbacks. The comparison will be done in the context of CTC analysis.

A general drawback of applying cytometric CTC evaluation is the need to enrich the sample to be able to acquire enough data in a reasonable amount of time. Enrichment will inevitably result in cell loss and consequently in a lower sensitivity.



## 1.1.2 CTC enumeration – Flow cytometry

### *Introduction*

Flow cytometry (FCM) is generally considered as the gold standard system for automated cell analysis.<sup>28</sup> It determines from individual cells in a population a number of quantitative fluorescent parameters and/or some light scattering derived morphological parameters. Nowadays flow cytometers are capable of analyzing large amounts of cells (10.000 cells/sec) and about 100 to 160 blood samples per hour. This type of hematology analyzer can e.g. perform a 5-part differential leukocytes count based on light scatter. With the use of immunofluorescent probes it is also possible to differentiate the leukocytes further into many subclasses. The technique used in a flow cytometer (figure 1.1.4) is based on hydrodynamic focusing of the cells due to a laminar sheath flow in a small flow chamber. The cell sample is injected in the core of the fluid stream. This forces the cells to follow the fluid stream in the middle of the chamber and by consequence they pass one by one through the focus of a laser beam.

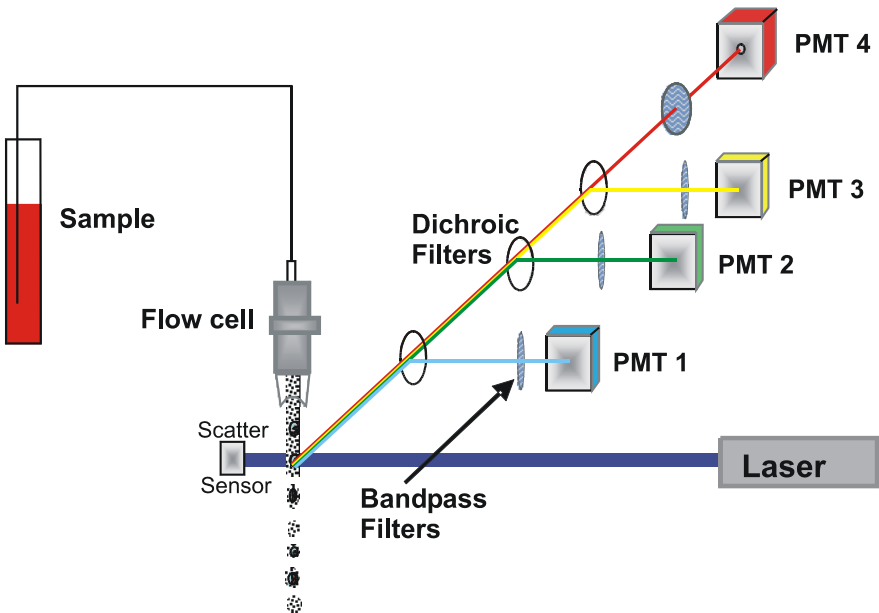


**Figure 1.1.4** Heart of a flow cytometer: The scattering and fluorescence is detected with photodiodes and PMTs. Cells are hydrodynamically focused in the core of the fluid stream and pass one by one through the focused laser beam. (Source image: J. Paul Robinson, Purdue University)

A FCM detects for each cell the light scattered intensity and the emitted fluorescence. The measured parameters depend on the fluorescent staining, cell size, granularity, complexity and lobularity of the cells. The sensitivity of commercial systems is high and in the order of 100 molecules of soluble fluorescein can be detected.<sup>28</sup> This limit may even be lowered further by a decrease of flow speed and sample stream diameter.<sup>29</sup>

### ***Flow cytometric CTC analysis***

Flow cytometric analysis has been used for CTC enumeration<sup>30,31</sup> and is capable of detecting epithelial cells, as is shown in figure 1.1.5. Although it is possible to detect and enumerate cell types by flowcytometry which are present in frequencies as low as  $1$  in  $10^7$ , the time needed to perform such an analysis becomes practically unacceptable when no pre-enrichment procedures are used.<sup>30</sup> Furthermore FCM has several disadvantages, especially regarding enumeration of rare cell populations like occur for CTCs. FCM is, in its nature, a high throughput system that relies on statistics. Large populations can be counted accurately but a few or even one single event cannot be easily discriminated from debris and artifacts. It lacks the specificity to completely characterize a specific event; from that point of view, FCM is not able to accurately enumerate rare cells. Accurate enumeration requires a specificity that can only be reached by analysis of a detailed image of each event. It should be noted that now there exists one commercial flowcytometer<sup>32</sup> (Amnis Corporation, Seattle, WA, USA) that uses a flow system and images the cells in flow with TDI CCD technology. This machine is a great improvement and gives the specificity needed. The system has shown to be as sensitive as traditional FCM but is remarkably slower,  $\sim 170$  cells per second can be detected. Another drawback is that the cells used for the FCM analysis are generally lost. Even when the FCM is equipped with a cell sorter, reexamination of a specific event is not always possible. Therefore revisiting an identified specific event, to obtain further details, or to perform further analysis like 3D imaging, or to apply a multiple re-labeling strategy, is not possible.

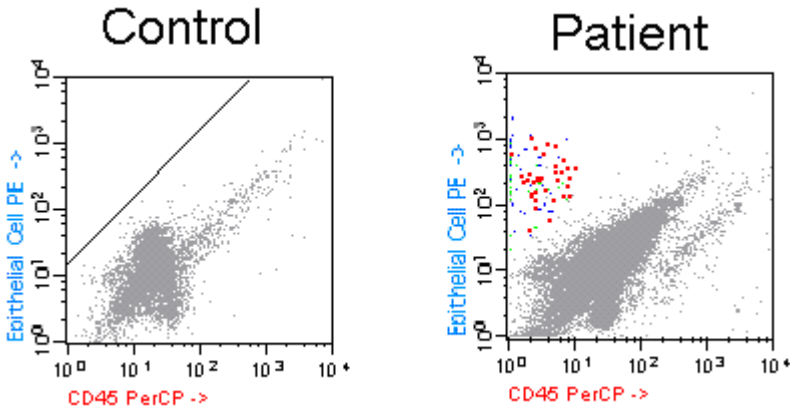


**Figure 1.1.5** Flow cytometric CTC enumeration of the cells isolated from 20 ml blood, by immunomagnetic sample enrichment. Blood was drawn from a healthy donor and from a patient with breast cancer with known bone metastasis, respectively. The figure shows the immunofluorescent staining by CD45 PerCP and anti-Epithelial Cell PE. Cells which are located above the line indicated in the left panel and display light scattering characteristics and nucleic acid characteristics typical for ferrofluid selected epithelial cells, are depicted in red. Before assignment of an event as a cell of the epithelial cell lineage, the event should have specific light scatter characteristics as well as be appropriately stained by the nucleic acid dye. All events in the sample, not found in a location that is expected to be characteristic for epithelial cells, are depicted in gray. Those events that fall above the line after appropriate nucleic acid staining, but outside the light scatter region typical for ferrofluid selected epithelial cells, are depicted blue. Events above the line lacking the typical nucleic acid staining and light scattering characteristics, are depicted green. The figure shows that in the 20 ml of blood of the normal donor no events can be found typical for epithelial cells, whereas in the 20 ml of blood from the patient, red, blue and green events can be detected. This dot plot directly indicates the limitations of a flowcytometer. Although a specific population appears, it is not certain that these are indeed CTCs due to the lack of morphological information. An event represented by a single dot may indeed be a CTC but could also represent debris. This cannot be revealed from this data. (Source data: Leon WMM Terstappen)<sup>31</sup>

### 1.1.3 CTC enumeration– Image cytometry

#### *Introduction*

Automated fluorescent microscopy has made rapid advances in the last 10 years. This was possible because computing power; disk storage and high-speed sensitive cameras became widely available. This resulted in several platforms that can image cells, store the data and interpret brightfield or fluorescent images automatically<sup>33,34</sup>. The excitation of the fluorescent probes is in general done with a mercury arc lamp (HBO) or a xenon lamp (XBO) and some systems use lasers or LEDs for illumination. The cells to be analyzed are usually stained with fluorescent dyes and are randomly spread over a microscope slide or a specific chamber. The labeling by specific fluorescent probes yields cell images with a high resolution and makes it possible to investigate and to enumerate many cell types. Basically all these systems use an X-Y stage and an automated focusing system to scan a large surface area of the slide. A camera gathers the individual images and a computer performs the image analysis. The parameters determined are based on morphological and fluorescence parameters. Of this systems the specificity with regard to morphology, is very high. Specific staining patterns and optical density can be determined for each individual cell at the level of the diffraction limit. Furthermore, if acquisition time is not a limit, a high sensitivity can be obtained that may reach even one molecule of soluble fluorescein. Of course, this is all dependent on the particular sample and on the image quality, resolution and other settings used.

#### *Image cytometry and CTC detection*

The amount of automated image cytometers for CTC detection is at the moment still limited. Only a few systems have the appropriate software which is dedicated for CTC/rare event analysis.<sup>35-37</sup> Nevertheless image cytometric analysis for CTC enumeration is already used in several studies. It was shown that these systems are capable to detect epithelial cells which are present in frequencies as low as 1 in  $10^7$ . Furthermore image cytometers are extremely specific whereas an image gives morphological information for each specific event. This makes it possible to discriminate CTCs from debris and cellular constituents of the blood. Besides discrimination, the morphology gives also additional parameters which can be used to characterize a specific CTC. Another advantage of image cytometry is that cells remain at there initial position. Each specific event can be revisited to obtain a 3D image and it is even possible to revisit cells after re-labeling. This makes it possible to investigate “positive” samples further for specific antigens or genes.

However there are some drawbacks regarding image cytometry. Just as in the case for flowcytometry, the time needed to perform such an analysis is unacceptable

when no pre-enrichment procedures are used. In the case of image cytometry it is even worse, because of the low throughput.

The important aspects of an image cytometer are therefore specificity, sensitivity, dynamic range acquisition time and image processing. These parameters are all closely related. A high specificity regarding morphology and a larger dynamic range is obtained when using a higher resolution. However, these advantages come at the cost of overall acquisition time when compared to a low resolution system. Therefore a proper choice is needed for CTC analysis. Increasing resolution only makes sense if the application requires more specificity and dynamic range. A more formal discussion will be given in chapter 2.3. In short I will compare the differences between a high resolution and a low resolution system. To this end I will make a comparison between the current “CellTracks Analyzer II” (Immunicon Inc, Huntingdon Valley, USA) developed by Immunicon and compare it to the CellTracks TDI setup.

### ***CellTracks analyzer II***

The “CellTracks Analyzer II” is a fully automated microscope system<sup>38</sup>. The images are sampled at a resolution of 0.645  $\mu\text{m}$ . In this instrument, an immunomagnetic enriched sample is used that is inserted in a sample chamber to present the CTCs to the detection system. The dimensions of this chamber are 2.7x29.7 mm. A frame transfer camera acquires images frame by frame to cover the complete microscope chamber. It uses a 10X 0.45 NA microscope objective and a mercury arc lamp. Such a low magnification system is relatively fast, it is able to scan a complete sample chamber within 9 minutes for 4 different markers.

### ***CellTracks TDI***

The design of the CellTracks TDI system allows detecting and analyzing the same samples as used in the CellTracks analyzer II, but now at a higher resolution. Therefore it uses a 40X NA 0.6 microscope objective to increase resolution and has a final magnification of 32.25x with a sampling resolution of 0.2  $\mu\text{m}$ . However, increasing magnification results in a reduced scan speed. If for the CellTracks TDI no further adjustments had been made, as compared to the CellTracks analyzer II, scan times could take more than 1.5 hours. Therefore other parameters determining scan speed and sensitivity have to be improved. Apart from the increased light gathering power of the NA 0.6 objective, image acquisition has been optimized using a TDI imaging CCD. This effectively reduces overhead time due to stage repositioning. Hence, it results in a shorter scan time yet using the same integration time. Effectively TDI saves 40 minutes due to reduction of overhead time with ~90%. Furthermore the sensitivity is increased and the integration time is reduced by using multiple lasers for excitation. Effectively the total scan time with this system is ~ 40 minutes including overhead time. This scan speed is currently limited by the maximum acquisition speed of the camera and the acquisition width.

At present only 67% of the camera width is used and extending the illumination profile could bring this setting to acquisition times of ~26 minutes. Further increase of scan speed is still possible and can be obtained with a faster camera system whereas the amount of emission light can be increased by the controlled laser excitation. The sensitivity of this instrument at the maximum scan speed is approximately 300 PE molecules measured for beads with  $\phi \approx 7.3$  micron. For smaller probes like tiny FISH probes the sensitivity is higher because fewer pixels are used to obtain the same signal. Increasing sensitivity is still possible by reducing the scan speed which results in an increase of the integration time. However; the full well capacity of the pixels is limited and would result in a saturated signal for brighter signals. Typically 4 logs of dynamic range can be obtained with this system. But dynamic range depends on particle size and increases for larger particles. The coefficient of variation (CV) that could be obtained with the CellTracks TDI using  $\phi \approx 3$  micron RLP-30 rainbow calibration beads (Spherotec, Libertyville, IL, USA) is ~4-5%.

### **1.1.4 CTC Analysis and enrichment**

As mentioned before CTCs are extremely rare. To enumerate the CTCs an enrichment step is necessary to reduce the overwhelming amount of cellular constituents of the blood. Several methods can be used to enrich the sample. Some of these methods are based on density gradient separation, like (OncoQuick).<sup>39</sup> It enriches the CTCs based on their density that is higher than from the cellular constituents of the blood. Another method is filtration (ISET).<sup>40</sup> In this method CTCs are filtered out based on size. Most CTCs are slightly larger than the average cellular component in the blood. A recently introduced method is FAST<sup>41-43</sup>, this method “enriches” the sample with a fast pre scan of the complete sample to detect possible events of interest based on cytokeratin labeling. We use immunomagnetic enrichment. In this method CTCs are enriched based on the expression of an epithelial surface marker EpCAM. This will be described in more detail in the next paragraph. All of the methods mentioned have their specific limitations. In general each method will loose some CTCs and is not 100% efficient. Furthermore manual preparation of the samples is prone to errors due to the extensive amount of preparation steps which are involved in these enrichment procedures. To obtain a consistent and reliable enrichment it is therefore an absolute necessity to use a well defined and highly automated labeling and selection protocol.

## ***Immuno magnetic enrichment***

Immunicon developed a labeling strategy for the immunomagnetic enrichment of CTCs. The company developed the CellSave™ and Autoprep™ technology<sup>44-47</sup> to label and to enrich CTCs from a 7.5 ml blood sample. After blood draw the sample is stored in a CellSave tube that contains preservatives to store the CTCs up to 96 hours before processing. Before processing, 7.5ml of the sample is centrifuged to remove the plasma and to replace it by system buffer. Further processing and enrichment is done by an automated system (Autoprep™). Several labeling and enrichment steps are applied as shown in figure 1.1.6. This results in an enriched sample with a volume that has been reduced from 7.5ml to 320 µl. Typically a recovery rate of 85% of the CTCs is obtained.

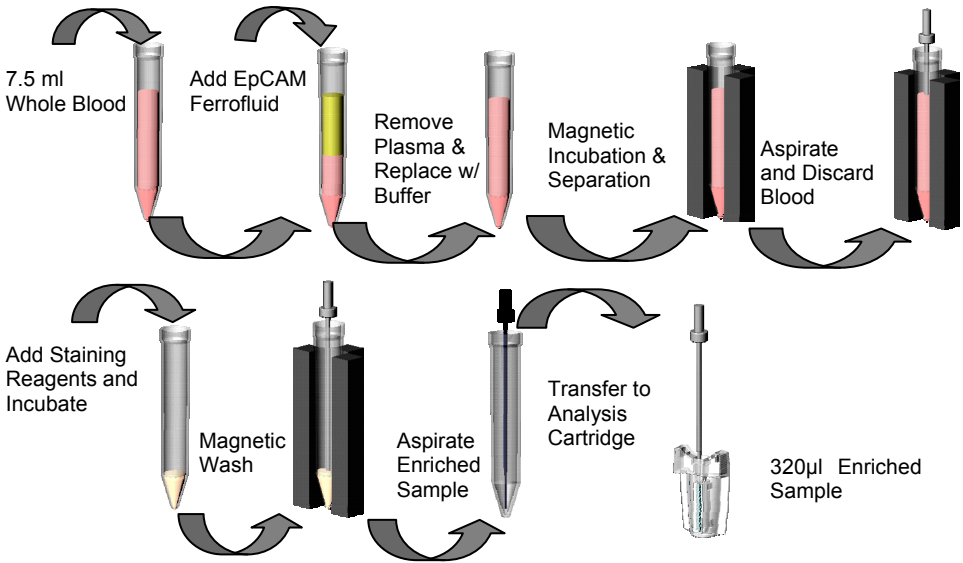


**Figure 1.1.6** Sample enrichment by the autoprep system. CTCs are enriched by means of multiple magnet washing steps. At the end of the process the sample is fluorescently labeled, aspirated and transferred to the sample cartridge. The sample preparation is then finished. Analysis of the concentrated sample will take place in the CellTracks TDI system.

### ***Fluorescent labeling***

The (anti-EpCAM) ferrofluid binds specifically to the CTCs and is used to select these cells. A drawback is that  $\sim 0.01\%$  of the leukocytes will either stain non-specifically label with EpCAM or are simply carried over during the enrichment. To identify the CTCs in the enriched sample, the sample is stained with the nucleic acid dye DAPI. Monoclonal antibodies directed against cytokeratin 8, 18, 19 (PE-CK) are labeled with Phycoerythrin, and monoclonal antibodies against CD45 (APC-CD45) are labeled by Allophycocyanin. Cytokeratins are cytoskeleton proteins present in cells of epithelial origin and CD45 is specific for leukocytes. This labeling therefore enables us to discriminate between CTCs and non-specific selected leukocytes.

The absorption and emission spectra<sup>48</sup> of the fluorophores used in the CTC enumeration assay are shown in figure.1.1.7.

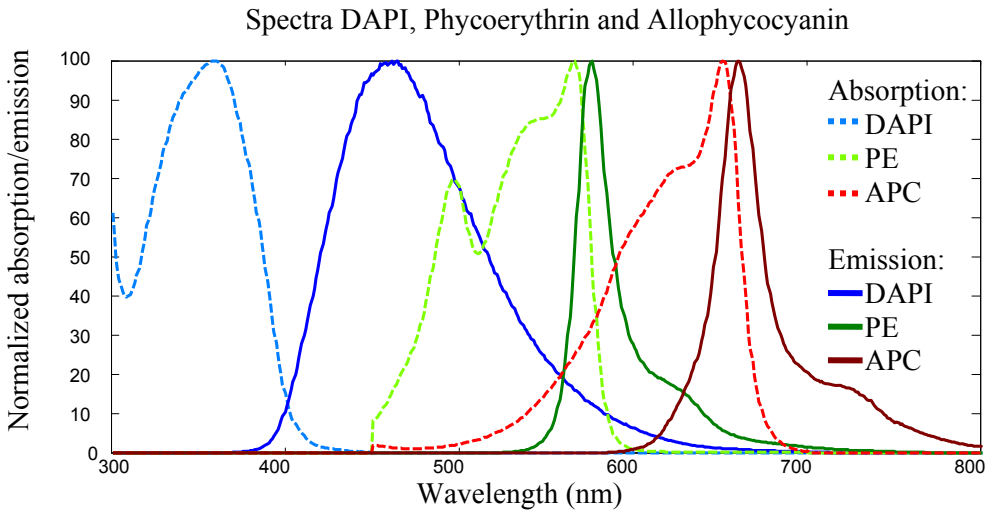


**Figure 1.1.7** Emission- and absorption spectra of DAPI, Phycoerythrin and Allophycocyanin used in the CTC enumeration assay.

### ***Sample cartridge***

The immunomagnetic selected cells are presented at the upper surface of a sample cartridge<sup>49</sup> with the use of a special set up, MagNest<sup>®</sup> (Immunicon). The MagNest is shown in figure 1.1.8a. Due to the field gradient, the cells rise to the top surface of the sample chamber. The cells follow a straight trajectory because of the shape of the magnetic field gradient, as shown in figure 1.1.8b



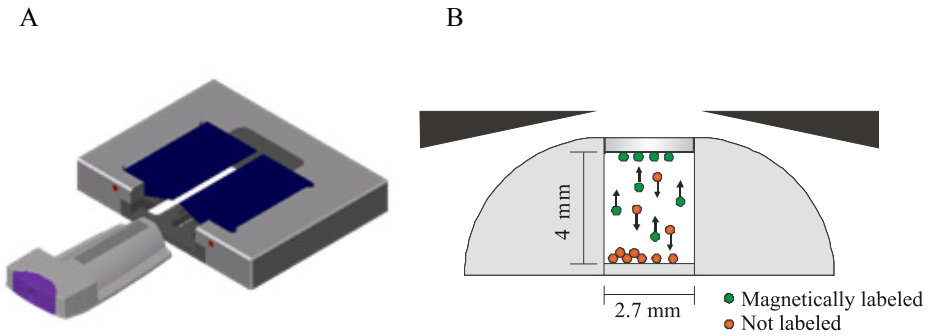


**Figure 1.1.8** A) Sample cartridge and MagNest. B) Cross-section of sample chamber. Magnetically labeled objects move along a straight trajectory along the field gradient and are distributed at the glass surface.

## 1.1.5 The CellTracks Project

### *Project objective*

The objective of this PhD project is to generate ideas and develop an instrument that can follow up of the current CellTracks analyzer II. The instrument should be capable to detect and analyze rare events from an immunomagnetic enriched blood sample. These detected CTCs should be analyzed completely at high resolution and for many markers, to make the “best” possible identification of the cell in the least amount of time. However the “best” possible identification and the least amount of time do not really go side by side. Therefore a proper criterion is needed. High quality 3D confocal images for lots of probes and for all cells is probably overdone and would not add much more specificity and would rather be a very time consuming approach. Increasing resolution and adding more markers only makes sense if the application really benefits from more specificity. The CellTracks TDI system introduced here was therefore specifically designed to improve the enumeration and identification of CTCs by increasing resolution, sensitivity and minimizing acquisition time. Further more it incorporates the possibility to reexamine and to re-label specific events of interest if more detail is essential.

### *The initial CellTracks*

The first CellTracks system was developed several years ago in our group by Tibbe et al.<sup>50</sup> It combines an immunomagnetic selection of the target cells, followed by an optical characterization and detection of these cells. To this end the target cells were loaded with both immunomagnetic labels (beads) and specific immunofluorescent labels. The instrument is a kind of no-flow cytometer. It uses a sample chamber with nickel lines to align the immunomagnetically selected target cells at the surface of an analysis chamber. These cells were then scanned by a small laser beam. The fluorescent signal was picked up with a CD-player lens system and detected by photomultipliers (PMT). Apart from the PMT signals this

system was also capable to make images of specific events. The CellTracks system strongly reduced the complexity normally involved in FCM. However, the instrument was initially designed for the enumeration of leukocytes and after the project the focus shifted from the analysis of leukocytes to cancer cell detection, in particular the analysis of circulating tumor cells (CTCs). Analysis of these cells is performed by analyzing images of target cells. Due to this shift, major modifications and improvements of the CellTracks system were necessary. An important aspect concerned the image quality that could be obtained with the CellTracks system from selected cells. The CD-player objective was not sufficient to obtain the high quality images for multiple fluorophores now required. Furthermore the CellTracks used a line illumination profile, which makes it difficult to use a traditional frame transfer camera

### ***TDI***

This situation led to the introduction of a TDI camera for image acquisition<sup>51,52</sup>, which is a suited approach when using line illumination. As shown in figure 1.1.9a it is possible to obtain good images with a CD-player objective, because the CD player lens has a numerical aperture (NA) of 0.45. However, the CD-player objective lens is an aspherical lens, specifically designed to create a small diffraction limited spot at 780 nm. Therefore a relatively large chromatic aberration can be observed. This results in a difference of the focal distance of 15 micron for green and red. Hence, an achromatic lens is required.

### ***Achromatic lens***

The achromatic lens to be used should be small and have a mass comparable with the original spherical lens to prevent a reduction of the bandwidth of the voice coil system. Therefore a small achromatic lens was glued into the voice coil system of the CD-player objective; this resulted in an overlap of the two focal planes. Consequently two fluorophores could be imaged in the same focal plane as shown in figure 1.1.9b. The bandwidth (~20 Hz) of the system was slightly reduced due to the increased mass, but was still sufficient. However the NA of this lens was 0.27 and resulted in a reduction of the collection efficiency.

### ***Microscope objective***

To overcome these problems a decision has been made to remove the CD-player objective system and to replace it with a high quality microscope objective with a NA of 0.6. Consequently a new method was needed to steer the microscope objective. This resulted in a system that operates in feed forward. The skew of the nickel lines and the offset of the focus position were determined prior to scan. A piezo element was used to steer the axial position of the microscope objective. The lateral position was adjusted by two controlled stacked XY stages. This resulted in

a system that obtained high quality images (figure 1.1.9c) without chromatic aberrations and with a high numerical aperture. Furthermore it could measure the fluorescence intensity using multiple photomultipliers.

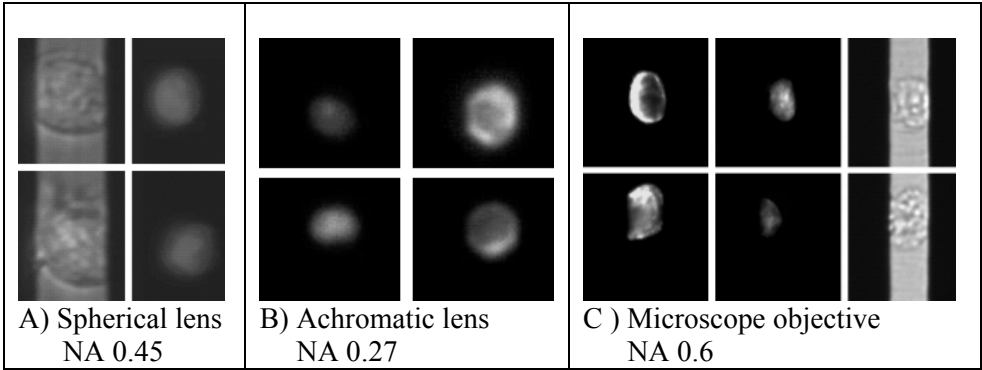


**Figure 1.1.9** Images obtained with the CellTracks system: **A)** equipped with a spherical CD-player lens. **B)** equipped with a small achromatic lens. **C)** equipped with a high quality microscope objective. (Apparent from these images is that the nickel line structure partly blocks the cells.)

### ***Cell alignment***

Although the images obtained between the nickel lines could be detected with a high resolution, it is clearly visible from figure 1.1.9 that a part of the cells is sometimes obstructed by the nickel lines which make imaging of the complete cell impossible. Hence, a structure was desired that aligns the cells but which doesn't obstruct the light path as with the nickel lines. This led to the design of several types of grooved Polydimethylsiloxane (PDMS) structures by T.M. Scholtens. These structures (figure 1.1.10b) mechanically align the cells<sup>53,54</sup> and reduce effectively the total surface area to reduce scan time. Although good cell alignment could be achieved, for optimal detection of the CTCs it is required to obtain 100% alignment and therefore optimization of these structures is still in progress.

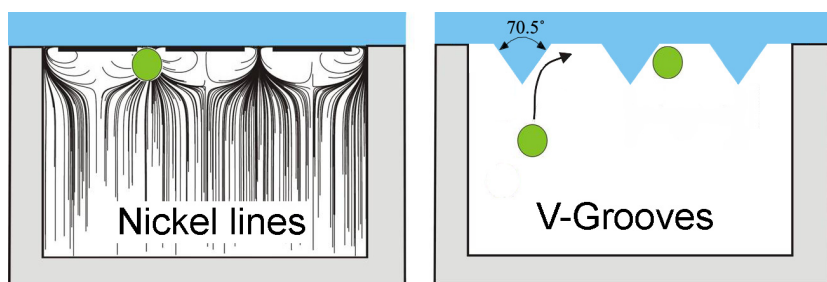


**Figure 1.1.10** Cell alignment: **A)** Sample cartridge with Nickel line structure to align the cells magnetically. **B)** Sample chamber with V-grooved PDMS structure to aligns the cells mechanically, without obstructing the light path.

### ***No Cell alignment***

To overcome the alignment and cell obstruction problems, we decided to use sample chambers with a flat glass surface without an alignment structure. This consequently resulted in a system where the photomultiplier could not be used in the way it was done previously. Therefore we had to omit the previously designed laser scanning system using PMTs. Although this system could rapidly scan a complete chamber, for CTC analysis images are still desired. Therefore such a system still needs reexamination of all events based on the initial scan. Reexamination of a few hundred events is time consuming. For each possible candidate an image should be acquired. Basically it is a balance of sensitivity and total acquisition time. Hence, a fast laser scanning system with reexamination is only faster if the amount of reexaminations is limited.

### ***CellTracks TDI***

In this thesis I will describe the advances that have been made in developing the new CellTracks system. The optics and the detection system were completely redesigned. The immunomagnetic selection remained almost the same, but now without a nickel line structure. The instrument operates under control of a LabView program that can also store and handle the (massive amount of) data obtained during analysis of a sample. In its current state the new CellTracks system can better be described as an image cytometer that uses wide field laser illumination. For clarity our new system will be called the “CellTracks TDI” and we will refer to the Immunicon system as “CellTracks Analyzer II”

The system uses multiple laser lines for optimal excitation in combination with beam homogenizing optics. Increased sensitivity and scan speed is obtained with a scientific grade dual mode TDI/frame transfer CCD camera. Furthermore dedicated software programs have been written for automated instrument control and image

analysis. These programs are dedicated to CTC analysis and are able to handle the massive amount of data which is obtained for each measurement. Besides initial sample analysis the CellTracks TDI is also capable to revisit and to reexamine specific events of interest. This can be done after image analysis and/or after re-labeling the sample with different probes. During reexamination it can make 3D images of a cell to obtain more detail of a specific event and further image enhancement is obtained with deconvolution software.

As a final remark we can say that the overwhelming amount of cellular objects in peripheral blood makes it a real challenge to find a single event and confirm that it is indeed a “CTC”.



# Part II

# Instrumentation





## **2.1 Instrument – Hardware**

### **2.1.1 Introduction**

Flowcytometry is the technology of choice for identification of cell populations when a large number of cells are available and the population of interest forms a distinct cluster in the multidimensional space created by the acquisition of multiple parameters. In contrast microscopy is the technology of choice when the cell number is limited and high resolution is needed to characterize the cell of interest. Fluorescently labeled probes that identify specific cellular components are widely used for cell analysis. By flowcytometry cells can be analyzed at high speed and antigens can be detected when present at relatively low levels (~100), whereas the throughput in microscopy is low but single molecule detection can be achieved. For identification of rare cells the detection of a few events by flowcytometry is not sufficient as one has no assurance that the event detected is indeed the cell of interest or represents debris. To overcome this problem, more information is needed about such a rare event. An imaging technique is more adequate to solve this problem. Current image cytometers capture a sequence of images, frame by frame over a large surface area, and make use of image analysis to enumerate the cell populations and quantify the expression of specific cell markers. Frequently the light sources of these systems are mercury arc lamps. The advantage of these lamps is the availability of multiple emission lines for excitation and a homogenous illumination profile. A major drawback of the mercury arc lamp in a fully automated image cytometer is the limited lifetime (~200 hours) and the heat production. Also the lamp requires frequent replacement and alignment by an operator. Furthermore the total illumination area of the lamp is much larger than the detection plane, resulting in unnecessary bleaching of the fluorescent probes in adjacent areas.

The system that will be introduced in this thesis is a fully automated image cytometer that scans large surface areas using a time delay integration (TDI) camera. For illumination multiple lasers are used in combination with beam homogenizing optics to obtain an adequate profile. This type of illumination and detection results in optimal quantification of fluorescence signals and the fluorescent probes are only illuminated when the cells are in the plane of the detector. The lifetime of lasers is much longer (~20000 hours) as compared to mercury arc lamps, they can be switched on and off rapidly, produce less heat, have an intensity that is constant in time and the irradiance can be much higher. The drawback of the use of a laser in an imaging system is the coherence property

of the laser light, resulting in unwanted interference effects. To obtain a quality image with laser illumination the coherence needs to be reduced.

The optical system of the cytometer introduced here provides an image and quantifies the information for each specific event. An initial scan is used to identify events of interest and these are revisited to make a 3D Z-stack or a time laps series of the specific event. This results in a better specificity for characterization of the cells of interest.

## 2.1.2 Optical layout

The setup shown in figure 2.1.1 is a schematic representation of the CellTracks TDI image cytometer. For the excitation of the sample 4 laser lines are available that can be controlled separately, or in combination, to excite a wide range of fluorophores.

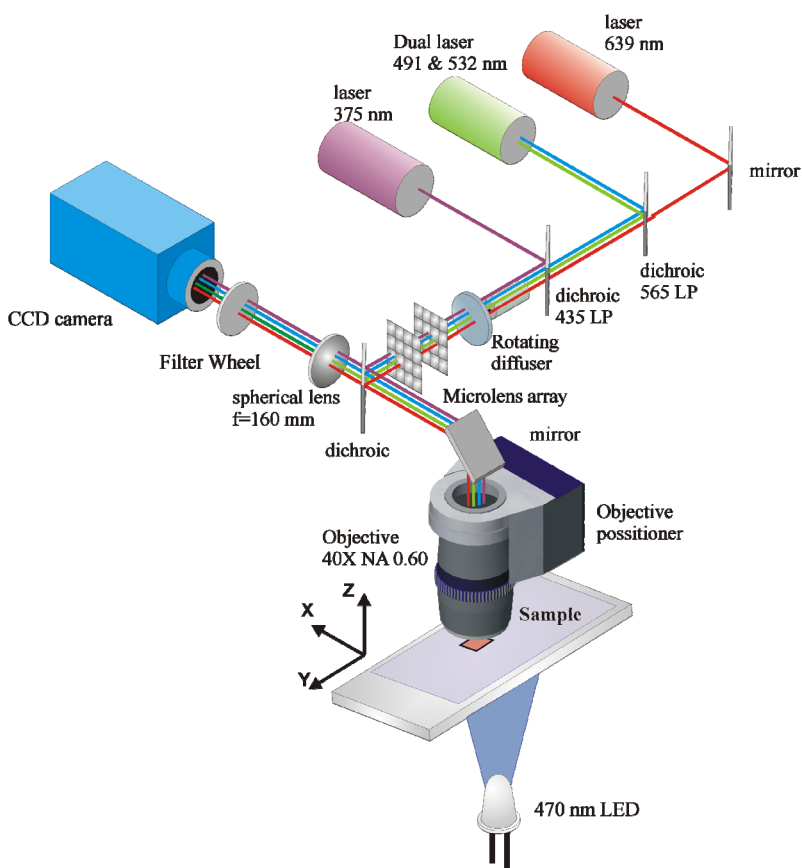


**Figure 2.1.1** Schematic representation of setup showing the major components.

To merge the output of the 4 lasers into 1 parallel beam that enters the objective, we use multiple dichroic filters (Omega Optical Inc. Brattleboro, VT). The first laser shown in figure 2.1.1 is a 16 mW 375-nm laser diode (Power Technologies, Little Rock, AR) that is coupled in with a 435 drlp (dichroic longpass mirror). The second laser is a dual line diode-pumped solid state laser with an output of 20mW at 490 nm and 20mW at 532nm (Cobolt AB, Stockholm, Sweden) and is coupled in with a 565 drlp. The third laser is a 30 mW 639-nm laser diode (Power Technologies, Little Rock, AR) coupled in directly, it passes through the 435 drlp and the 565 drlp. All beams are overlaid at the point where they pass the beam homogenizing optics (Suss-MicroOptics, Neuchatel, Switzerland). These optics create a square homogeneous illumination profile. This beam homogenizer consists of a rotating diffuser and two microlens arrays. After the last microlens array the laser light is redirected with a triple dichroic mirror (400-535-635TBDR) into the 40X 0.6 NA infinity corrected microscope objective (Nikon, Tokyo, Japan) to focus the laser light as a square ( $180 \times 180 \mu\text{m}^2$ ) homogeneous illumination area onto the sample. The resulting fluorescent light emitted by the cells is picked up with the microscope objective. It then passes through the dichroic mirror, and is focused onto the TDI camera (Hamamatsu, Hamamatsu city, Japan) by an achromatic lens with a focal length  $f = 160 \text{ mm}$  (LINOS Photonics GmbH, Göttingen, Germany). The final magnification is 32.25 X. Before the fluorescent light is detected by the camera the light first passes through a motorized filter wheel (Thorlabs, Newton, NJ) to select the proper band pass filter for each fluorescent probe. A blue 470 nm LED is used for bright field illumination and is located underneath the sample.

### ***Microscope objective***

The efficiency and resolution of the collection optics is primarily determined by the numerical aperture of the used microscope objective. It would be favorable to use a high NA objective to maximize detection efficiency and resolution. However the limiting factor is that a water/oil immersion objective is not practical in a scanning system. The working distance should also be larger than 2.2 mm to make the system compatible with an Immunicon analysis chamber in its magnetic holder. A high magnification/sampling resolution results in excessively long scanning times and trade offs need to be made between NA/working distance and magnification. We have chosen for an air immersion 40 X NA 0.6 CFI Plan Fluor ELWD objective (Nikon, Tokyo, Japan). This infinity corrected objective provides the highest numerical aperture in combination with a long working distance that ranges from 3.7 – 2.7 mm. The objective is optimized for transmission in the UV region. The 40 X objective magnification in combination with a 200 mm tube length and an imaging lens with a focal length of 160 mm results in a total magnification of 32.25 times.

### ***Detection efficiency***

An important parameter of the instrument is the photon collection efficiency. The solid angle of the microscope objective has a major effect in this efficiency. Its efficiency is given by equation 2.1

$$\frac{\Omega}{4 \cdot \pi} = \frac{2 \cdot \pi \cdot (1 - \cos(\theta))}{4 \cdot \pi} = \sin^2\left(\frac{\theta}{2}\right) \quad (2.1)$$

Where  $\Omega$  is the solid angle and  $\theta$  (Eq. 2.2) is defined as the half angle of light (figure 2.1.2) that is collected by the objective with  $n_i$  the index of refraction of the sample medium.

$$\theta = \arcsin\left(\frac{NA}{n_i}\right) \quad (2.2)$$

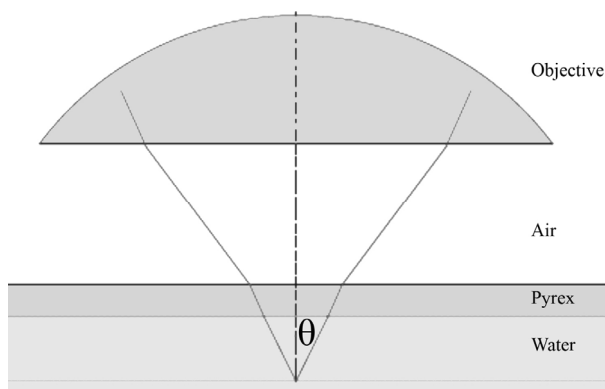


**Figure 2.1.2** Schematic representation of the half angle of the cone of light that is captured by the objective.

### ***Total detection efficiency***

The total detection efficiency of the instrument depends on the product of the transmission efficiencies of the objective and the other optical components. These efficiencies are determined by the absorption and scattering from optical elements like lenses and filters and the quantum efficiency (QE) of the detector. In table 2.1 an overview of the efficiencies at a wavelength of 585 nm is shown.

Optical Element	Efficiency at 585 nm	
Detection efficiency objective (Collected solid angle)	NA 0.45 air	2.9 %
	NA 0.60 air	5.2 %
	NA 1.40 oil	30 %
Transmission efficiency objective	89 %	
Filter Transmission dichroic	80 %	
Filter Transmission bandpass-filter	90 %	
Reflecting mirror	95 %	
Transmission imaging lenses	95 %	
QE efficiency CCD (peak)	70 %	
CCD Fill factor	70 %	
Transmission Pyrex glass (0.5 mm)	93 %	
<b>Total detection efficiency</b>	<b>1,4 % (NA 0.6 air objective)</b>	
Refractive index		
Air	1,008	
Immersion medium (oil)	1,515	
Pyrex	1,470	
Medium ( Water)	1,350	

**Table 2.1.1** Detection efficiencies and refractive indexes of the major optical components.

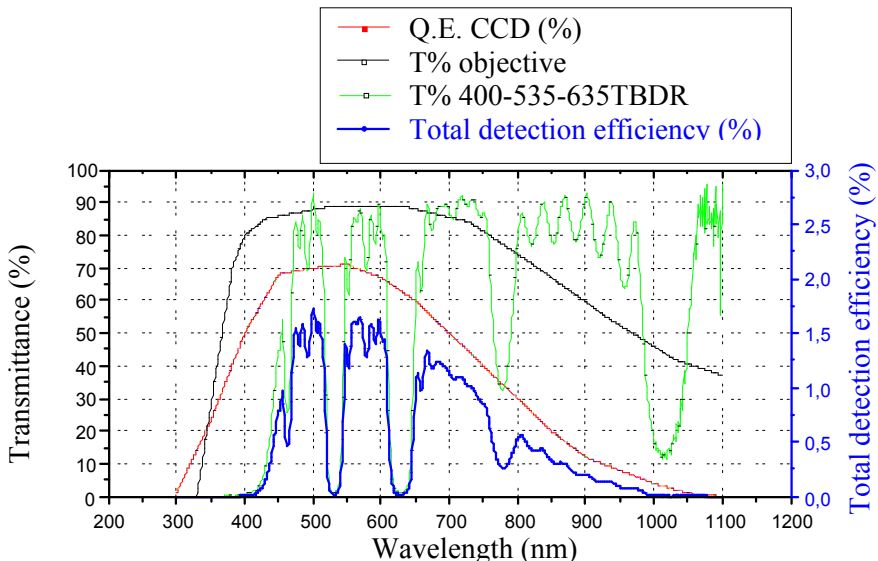


**Figure 2.1.3** Detection efficiency for the wavelength ranges from 300 to 1100nm. The transmission of the fluorophore specific bandpass filters has been omitted.

From the data shown in table 2.1.1 we calculated a total detection efficiency of 1.4% when a 580DF30 (Omega Optical Inc. Brattleboro,VT) is used.

As shown in figure 2.1.3 the detection efficiency is wavelength dependent and is going down above 600nm due to the lower transmission efficiency of the objective and the lower QE of the camera. The detection efficiency is primarily determined by the microscope objective where the solid angle is limiting the detection.

## 2.1.3 Excitation

### *Spectra*

In the present commercial CellTracks Analyzer II the cells are illuminated with a mercury arc lamp, an HBO 100 W with an arc size of 0.25x0.25 mm. Therefore a comparison with the current laser illumination system and the mercury arc based system is important. For the application envisaged multiple fluorophores are used: DAPI, Fluorescein (FITC), R-Phycoerythrin (PE) and Allophycocyanin (APC). In the case of a traditional fluorescence microscope usually the strong mercury arc bands are used to excite the corresponding fluorophore. These spectral bands measured with a USB4000 spectrometer (OceanOptics, Dunedin,FL) for 4 different filter cubes are shown in figure 2.1.4. The 4 laser lines available in the CellTracks TDI are also shown in the figure. The resulting excitation bands of the mercury arc lamp are relatively broad when compared with the 4 laser lines (half width ~2nm).

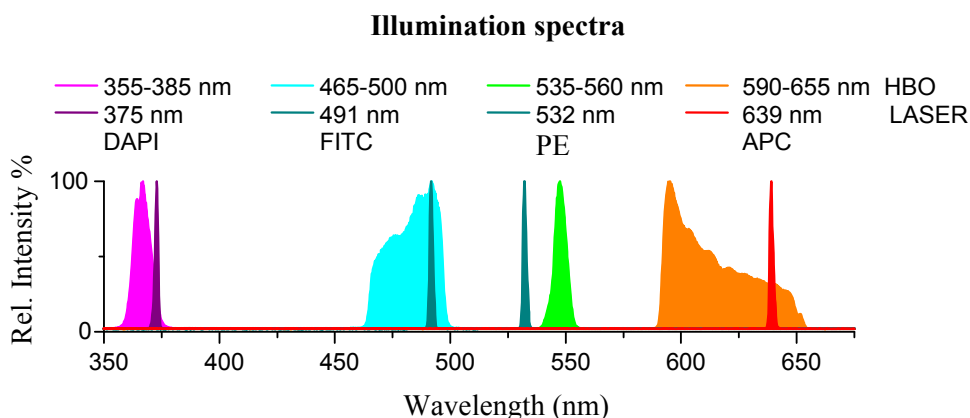


**Figure 2.1.4** Spectral output of a mercury arc lamp, equipped with DAPI, FITC, PE respectively APC filter cube, compared to the 4 laser lines available in the CellTracks TDI setup. Spectra were measured with a USB4000 spectrometer.

As shown in figure 2.1.4 the excitation spectrum of the APC filter cube is broad to obtain a higher excitation power at this band. This is necessary due to the lack of a high emission of the mercury arc lamp in this region. It shows that excitation with

a laser line is preferred when a high excitation power at a specific wavelength is needed. Lasers do not possess broad excitation bands that may cause the excitation of other fluorophores used in the assay.

### ***Irradiance***

To measure the irradiance of the sample with a mercury arc lamp in a fluorescence microscope like the CellTracks Analyzer II a 200 micron aperture was used. This partly obscures the illumination area and only a small region in the center of the object plane (0.0314 mm<sup>2</sup>) is measured. The used detector is an 840C handheld optical power meter (Newport, Irvine, CA) with an 818-ST-UV/CM sensor. This detector measures the total intensity through the pinhole in the center of the object plane. To calculate the transmitted energy, we used the central wavelength of the excitation spectra of each filter cube and laser line. Especially the red laser line has a much higher excitation power available to increase the irradiance and consequently reduce the integration time for the APC fluorophore. One has to be careful not to saturate the fluorophores. The 50% saturation level<sup>55</sup> of the fluorophores is given by equation 2.3 where  $\sigma_a$  is given by equation 2.4

$$I_{sat} = \frac{h \cdot c}{\sigma_a \cdot \tau_{fl} \cdot \lambda} \quad (2.3)$$

$$\sigma_a = \frac{1000 \cdot \ln(10) \cdot \epsilon_\lambda}{N_A} \quad (2.4)$$

For APC the molar absorption coefficient<sup>56,57</sup> is  $\epsilon_\lambda = 700.000 \text{ M}^{-1} \cdot \text{cm}^{-1}$  and it has a lifetime of  $\tau_{fl} = 1.8\text{ns}$ ,  $N_A$  is Avogadro's number ( $6.022 \cdot 10^{23}$ ). This results in a 50 % saturation level at  $65 \text{ kW} \cdot \text{cm}^{-2}$ . In figure 2.1.5 the irradiance is shown for the CellTracks TDI (Laser) and the CellTracks analyzer II (Mercury arc) setup. The irradiance of the red laser diode is  $32 \text{ W} \cdot \text{cm}^{-2}$  which is far below the 50 % saturation level of APC. Further increase of the laser excitation power is therefore still useful. As shown in figure 2.1.5 the 491nm laser line of the CellTracks TDI system is not measured. Although the 491 nm laser line is available, it can not be used because the 400-535-635TBDR triple band pass filter is not reflecting this wavelength. To make use of this laser line a quad band filter or a filter changer should be used.

## Irradiance

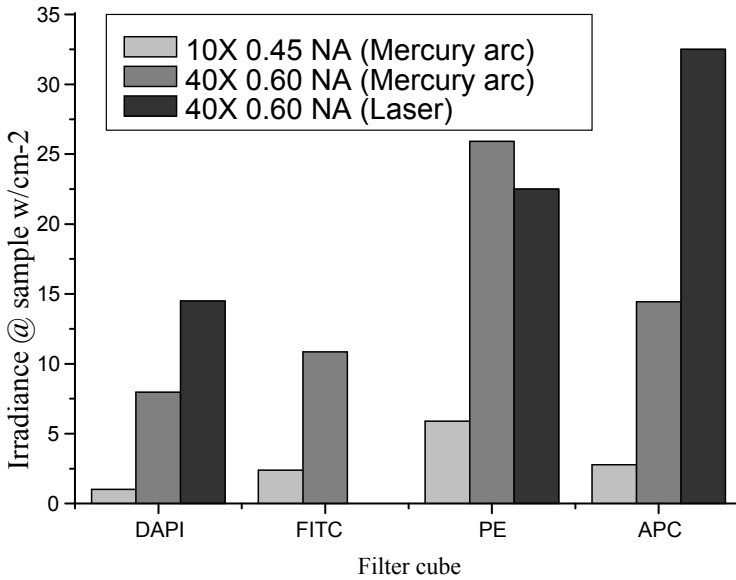


**Figure 2.1.5** Irradiance of the CellTracks analyzer II compared with the CellTracks TDI system. The CellTracks analyzer uses a mercury arc lamp with DAPI, FITC, PE and APC filter cubes with a 10X 0.45 NA or a 40X 0.60 NA microscope objective. The irradiance of the corresponding laser lines used in the CellTracks TDI setup is also shown. These are coupled in with a 400-535-635TBDR triple band pass filter. The irradiance was measured at a circular aperture of 200 micron in the center of the object plane.

## 2.1.4 Beam homogenizing

### *Introduction*

A homogeneous illumination of the sample is critical for an image cytometer to illuminate each cell with the same intensity when it passes through the laser spot. Inhomogeneous illumination leads to a variation of the fluorescence signal detected for cells with different positions in the object plane. To prevent unnecessary bleaching and maximize the signal collection of the sample, the illumination area should match the size of the CCD detector. To achieve this; a beam homogenizer (Suss-MicroOptics, Neuchatel, Switzerland) is used as shown in figure 2.1.6. It consists of a pair of microlens arrays<sup>58-63</sup> in combination with a rotating diffuser<sup>64</sup> and is creating a square homogeneous profile.



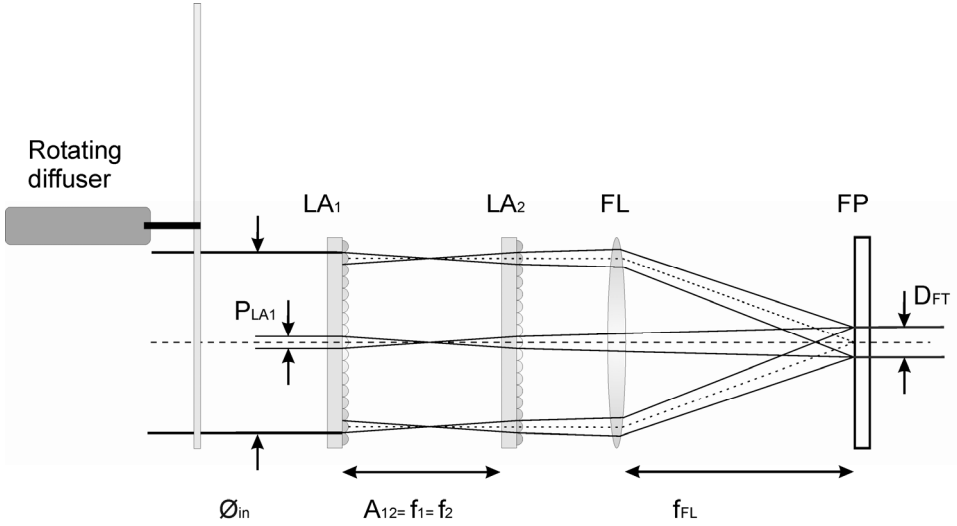


Figure 2.1.6 Beam homogenizing optics used to create a flat top profile.

### Beam homogenizer optics

The rotating diffuser in front of the homogenizer (Figure 2.1.6) is necessary to reduce the coherence length of the laser beams and to prevent interference effects at the two microlens arrays. While each microlens array consists of a periodic structure and acts like a diffraction grating it will generate diffraction spots with a period  $\Delta_{FP}$  and a spot diameter  $\delta_x$  in the Fourier plane<sup>65</sup>.

$$\Delta_{FP} = \frac{f_{FL} \cdot \lambda}{P_{LA1}} \quad (2.5)$$

$$\delta_x = \frac{2 \cdot f_{FL} \cdot \lambda}{D_{FL}} \quad (2.6)$$

The first square microlens array LA<sub>1</sub> (Figure 2.1.6) focuses the incoming beam at the next micro lens array LA<sub>2</sub>, resulting in multiple point sources. All these quadratics lens apertures (Figure 2.1.7) are imaged with the microscope objective and overlaid in the Fourier plane where they form a quadratic flat top. The size of the flat top is defined by:

$$D_{FT} = \frac{P_{LA1} \cdot f_{FL}}{f_1 \cdot f_2} \cdot ((f_1 + f_2) - a_{12}) \quad (2.7)$$

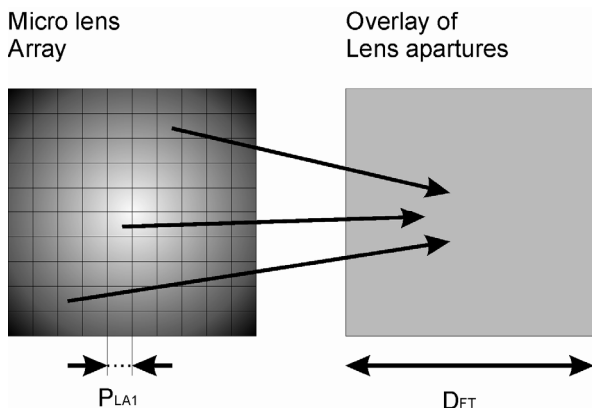


**Figure 2.1.7** Quadratic lens apertures create a flat top profile and are overlaid in the Fourier plane of the microscope objective, resulting in a homogeneous illumination area.

The details of the beam homogenizer are given in table 2.1.2.

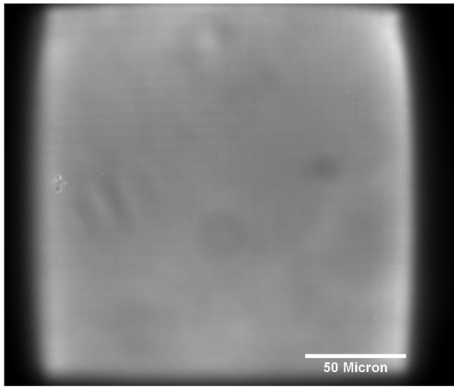
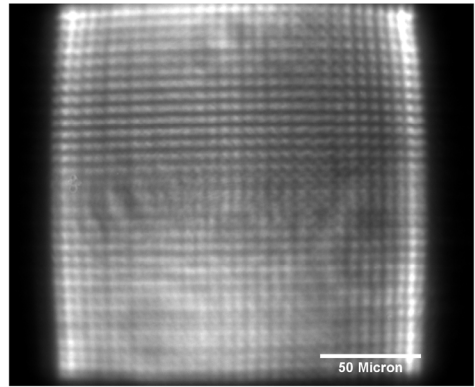
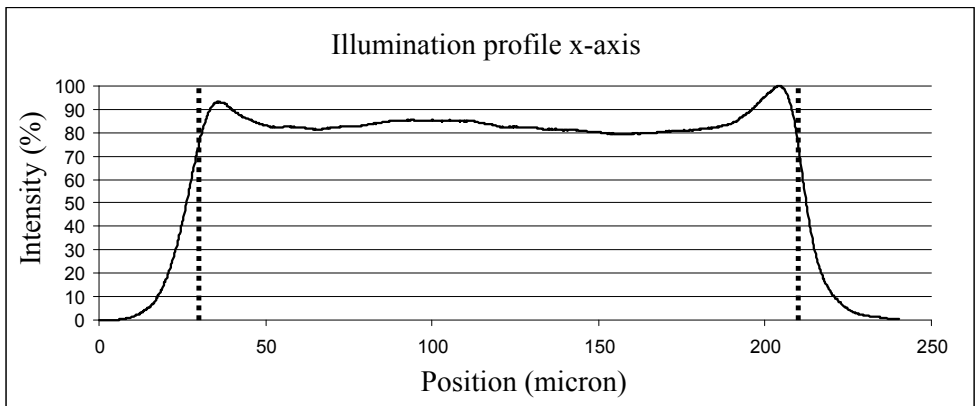
Parameter	Description	Value
$P_{LA1} = P_{LA2}$	pitch of the quadratic lens apertures	0.50 mm
$f1 = f2$	focal length quadratic lens aperture ( 532 nm)	15.54 mm
$f_{FL}$	focal length Fourier lens	5 mm
$a_{12}$	distance between $L_{A1}$ $L_{A2}$	15.54 mm
$D_{FT}$	flat top size $f1 = f2 = a_{12}$	0,161 mm

**Table 2.1.2** Beam homogenizer parameters

Slightly varying the distance between the two microlens arrays provides the ability to adjust the size of the flat top. Care should be taken not to overfill the aperture of the second microlens lens array. Overfilling results in crosstalk between the lenslets and a less sharply defined border of the flat top profile. As the focal length of an objective is inversely proportional with the magnification, the size of the flattop can also be adjusted by using a different microscope objective. This is useful to make the flat top approximately the size of the CCD in the object plane at different magnifications.

### ***Beam profile***

A homogeneous layer of acridine orange was used to determine the beam profile perpendicular to the forward scanning direction. The resulting profile is approximately  $180 \times 180 \mu\text{m}^2$  (Figure 2.1.8). The dotted lines indicated in this figure are the limits used for the illumination. All adjacent images of 180 micron width (See figure 2.1.10) are illuminated with this profile.

**(A)****(B)****(C)**

**Figure 2.1.8** Image captured of a homogeneous layer of Acridine Orange. **A)** Coherence length reduced with a rotating diffuser. **B)** Periodic structure in the Fourier plane created due to interference of coherent light source, without rotating diffuser. **C)** Illumination profile perpendicular to the scanning direction. The used area is 180 micron width. The coefficient of variation in this area is 5%.

Consequently the borders of each image are to some extent illuminated twice due to illumination of the previous scan, since the borders of the flattop are not infinitely steep. A grooved alignment structure as mentioned in the introduction (figure 1.1.6b) could prevent this. Furthermore it would limit the illumination area, to the central region of the profile which is even more homogeneous. It should be noted that the current illumination area is slightly smaller than the full width of the CCD camera (1344 pixel) and effectively only 900 pixels are used. The current flattop width is chosen to match with a grooved alignment structure. When scanning a chamber without an alignment structure it is preferable to increase the illumination profile and effectively make use of the complete CCD width.

## 2.1.5 TDI Imaging

### *Introduction*

Time delay integration (TDI) charge-coupled devices followed the development of the frame transfer camera and were introduced in the mid 1970's. The first applications were primarily in airborne and satellite imaging systems, nowadays they are also used for civilian applications like document scanning and industrial product inspection. Recently these types of CCD cameras have been introduced in flow- and image cytometry.<sup>32,33,66,67</sup> In our cytometer we make use of a CCD in TDI transfer mode, this provides the possibility to continuously scan large surface areas. There is no significant difference in the sensitivity and the data acquisition time between a CCD operating in frame transfer mode and a CCD in TDI transfer mode. The total acquisition time is however significantly decreased when using a TDI CCD for scanning large surfaces areas. TDI Acquires the images in continuous fashion, therefore overhead time is only introduced at the start and end position of a scan and not for each frame.

### *CCD camera*

The TDI camera used in our setup is a high sensitivity 12-bit Peltier cooled ORCA C4742-95-12ERT (Hamamatsu, Hamamatsu City, Japan) and is an interline transfer CCD that operates in frame transfer mode or in TDI mode. The CCD has an effective number of 1344(H) x 1024(V) pixels with a size of 6.45x6.45  $\mu\text{m}^2$ . More details are shown in table 2.1.3. The CCD element of such a camera consists of a 2 dimensional array with photosensitive elements and a masked V-CCD to transfer the collected charges as shown in figure 2.1.9a. When the camera is operating in interline transfer mode the charges collected at the photo diodes are transferred to the V-CCD at the end of the integration time and are shifted pixel by pixel to the H-CCD and transferred further to the on- chip amplifier and A/D converter. As shown in figure 2.1.9b, this CCD chip uses a microlens array to increase the effective fill factor, which is reduced in an interline CCD due to the masked V-CCD structure.

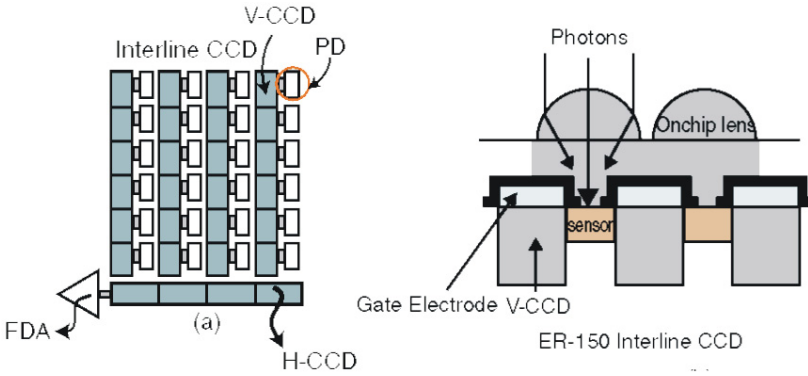


**Figure 2.1.9** Layout Interline transfer CCD (Source image: Hamamatsu technology primer.)

Parameter	Description	Value
$N_{HOZ}$	# Pixels horizontal	1344
$N_{VERT}$	# Pixels vertical (TDI Stages)	1024
$\delta p$	Pixel size	$6.45 \times 6.45 \mu m^2$
$L_{Time-minimum}$	Minimum readout time for each line	113 $\mu s$
$L_{Time-maximum}$	Maximum readout time for each line	56 ms
$\delta_s$	Sampling resolution	0.2 $\mu m$
$SNR_{max}$	Maximum SNR	43 dB
A/D converter		12 Bit
Readout Noise (r.m.s)		8 electrons
Full well capacity		18000 electrons
Amplifier gain conversion factor		4.6 electrons/ADcount

**Table 2.1.3** Major TDI camera parameters of the Orca ER-150 sensor

### ***Comparison TDI and frame transfer imaging***

#### *Frame transfer mode*

In conventional automated microscope scanning systems, images are acquired frame by frame as illustrated in figure 2.1.10a. For proper image alignment the stages need time to start and stop to go to each position. When an interline or a frame transfer camera is used the effective acquisition time for each frame is:

$$T_{Frame} = T_{ill} + T_{pos} \quad \text{and} \quad T_{readout} \leq T_{ill} + T_{pos} \quad (2.8)$$

Where  $T_{Frame}$ ,  $T_{ill}$ ,  $T_{readout}$ ,  $T_{pos}$  are the total acquisition time, illumination time, camera readout time and positioning time respectively.

For precise positioning with the motorized stages in the object plane the positioning time  $T_{\text{pos}}$  is about 0,2 – 1 sec depending on the stages, the desired accuracy and displacement. In contrast, in a camera operating in TDI mode the readout is continuous and there is no overhead due to positioning. Additional overhead is only introduced at the start and end position.

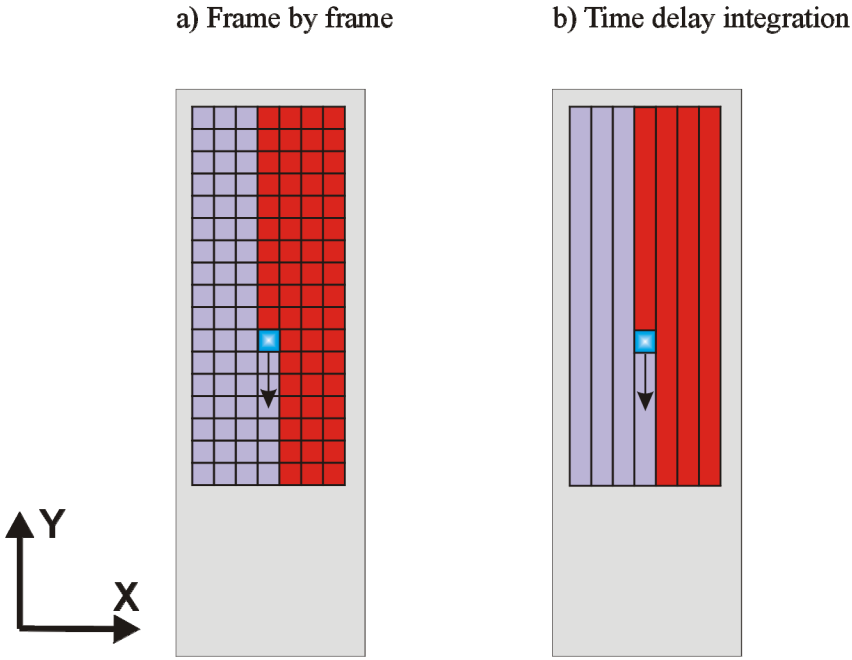


**Figure 2.1.10** Frame by frame imaging versus continuous motion TDI imaging.

### *TDI mode*

When the camera is operating in TDI mode the collected charges are transferred directly to V-CCD and shifted in parallel one row down towards the H-CCD when an external line trigger is applied. This is repeated for each row until the V-CCD reaches the H-CCD, and the total collected charge for each pixel is moved by the H-CCD to the amplifier and A/D converter. This stepwise integration of the parallel charge shift of the CCD is synchronized with the continuous motion of the stages. As the object moves, the accumulated charges also move in the same direction, with the same average velocity. This makes light integration and CCD readout a continuous process as shown in figure 2.1.11. The resulting image is  $1344 \times N_{\text{pixels}}$  and can be infinitely long. In order to obtain workable images the number of  $N_{\text{pixels}}$  in the scanning direction is set by the frame grabber to cut the “long” image in pieces. The total acquisition time of a single stroke in TDI mode is

therefore equal to the total integration/scan time and additionally time needed to accelerate and decelerate and stage motion.

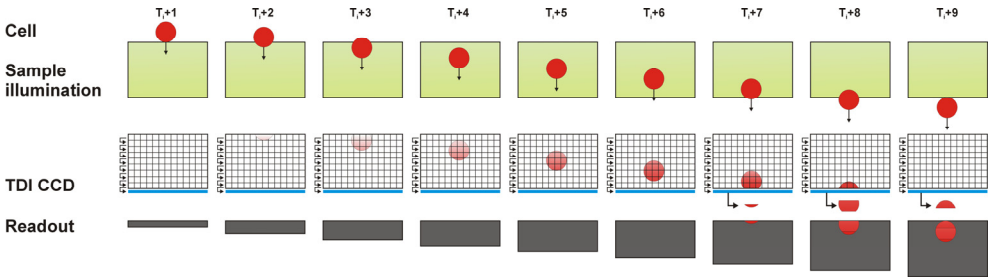


**Figure 2.1.11** CCD operating in TDI mode, the charge is accumulated and transferred at the same rate as the object movement.

### ***TDI scanning***

To prevent blurring and to obtain sharp images with a TDI camera precise alignment between the stage direction and the parallel shift of the CCD is essential. In addition the average speed of the moving object should be matched with the line transfer rate to achieve a square pixel image. The camera and the stage movement are synchronized with the encoder measuring the stage displacement in the scan direction. Although it is possible to synchronize the camera directly by a function generator that matches the average scan speed, optimal resolution can only be obtained when using an encoder. Small variations in the scan speed are synchronized with the camera line transfer for each position. The encoder of the stages, used to synchronize the camera with the stage position, has a resolution of  $0.1\mu\text{m}$ . It constrains the setup to a fixed magnification. Therefore the magnification should be adjusted to achieve a square pixel image according to:

$$M = \frac{\delta p}{\delta e \cdot k}, k = 1,2,3,4,5 \quad (2.9)$$

Where  $\delta p$  is the pixel size and  $\delta e$  the encoder resolution. With the use of a counter the required object pixel resolution can be obtained as a multiple of the encoder resolution. In our setup a sampling of  $\delta_s = 0.2 \mu\text{m}/\text{pixel}$  is used requiring a magnification of 32.25x. A perfect adjustment is required while a mismatch of this magnification results in blurring of the image. In case the magnification is too large or too small the image will be stretched respectively in the forward or reverse direction.

## ***TDI scan speed***

For TDI the acquisition time for each frame is equal to the total integration

$$T_{Frame} = T_{int} = L_{Time} \cdot N_{TDI} = \frac{\delta_S \cdot N_{TDI}}{v_{stage}} \quad (2.10)$$

and

$$L_{Time} \geq L_{Time-min}$$
$$L_{Time} \leq L_{Time-max}$$

and the scan speed can be calculated according to

$$v_{Stage} = \frac{\delta_S}{L_{Time}} \quad (2.11)$$

The line time ( $L_{Time}$ ) is the duration of each line before the data is transferred to the next TDI row. With a sampling resolution  $\delta_S$  of  $0.2\mu\text{m}/\text{pixel}$  and a minimum line time ( $L_{Time-min}$ ) of  $113.6 \mu\text{s}$  the maximum velocity is  $1.76 \text{ mm/s}$ . This results in a minimum integration time of  $116 \text{ ms}$  determined by the minimum readout time for each line and the number of TDI stages ( $N_{TDI}$ ). Shorter integration times are not possible when our camera is in TDI mode, this would require a camera with a faster readout. To prevent saturation of the camera the excitation power should be chosen appropriately. A more sophisticated approach could be achieved with a TDI camera using on-chip electronic exposure control that reduces the number of TDI stages. Data read out in these systems may occur before a separate line has reached the end of the CCD.

## ***Nonuniformity reduction***

Besides the reduction in total acquisition time the TDI operation also results in a more uniform overall photon response.<sup>68</sup> The averaging over  $N_{TDI}$  stages results in averaging down pixel photo response nonuniformity, that is caused by small differences in the quantum efficiency of different pixels and gives a reduction by a factor  $\sqrt{N_{TDI}}$ . The same effect holds for the dark current which is also averaged over multiple TDI stages. Next to these specific averaging effects for the CCD, similar effects arise from the optical parts of the instrument. While an object is moving through the illumination spot and imaged on the CCD, all non uniformities in the light path are averaged in the scan direction. These may appear due to a non uniform illumination profile. Also local variations in the transmission efficiency of the optics, (objective, imaging lens, dichroic mirrors, bandpass filters) due to small differences in the materials and interfering dust particles, may result in variations. These are all diminished by a factor.  $\sqrt{N_{TDI}}$



### ***TDI image degradation***

There are several sources of image degradation that are specific for TDI. A relative difference in motion between the TDI CCD and the object, results in an increase of the effective aperture.<sup>69,70</sup> Such an effect may be due to:

- Angular misalignment of the CCD and the stage scan direction.
- Mismatch between the velocity of the object plane and the velocity of the charge transfer of the TDI CCD in the image plane.
- Discrete movement of the signal charge of the TDI CCD while object movement is almost linear.

All these factors provide an increase of the effective aperture and result in blurring of the images.

#### *Angular misalignment*

The angular misalignment affects the resolution perpendicular to the scan direction. A small angular misalignment  $\theta$  results in a pixel overlap  $L_{align}/\delta p$

$$L_{align} = N_{TDI} \cdot \delta p \cdot \tan(\theta) \quad (2.12)$$

Blurring of the image due to angular misalignment is not significant and can be reduced to 0.5 - 1 pixels due to simple alignment of the stage direction and CCD position within an accuracy of 0.03 degrees or better.

#### *Velocity mismatch*

The mismatch between the velocity of the object and the velocity of the charge transfer of the TDI CCD is much more critical and it requires a smooth motion of the stages. As shown in figure 2.1.16 the stage position is not moving linear in time and is oscillating with a standard deviation of 0.8 micron around the commanded position. The use of a fixed line rate results in excessive blurring of the images and pixel overlap, and is therefore not desirable. The pixel overlap is given by  $L_{velocity}/\delta p$  which is equal to 8 pixels where:

$$L_{velocity} = \frac{\Delta V}{V} N_{TDI} \cdot \delta p \quad (2.13)$$

To prevent blurring of the images by a velocity mismatch an encoder is used to measure the stage position continuously. The encoder triggers the camera when the stage position has moved over 0.2 micron and ensures complete synchrony between stage motion and CCD charge transfer.

To obtain a 1:1 relation between stage movement and CCD charge transfer, the magnification should be 32.25x (Eq. 2.14) and accurate adjustment of the magnification is required to prevent blurring. A mismatch in magnification results in  $M_{\text{Magnification}}/\delta_p$  pixels overlap and is approximately 1 pixel.

$$M = \frac{\delta p}{\partial s} \quad (2.14)$$

$$L_{\text{Magnification}} = \frac{\Delta M}{M} \cdot N_{\text{TDI}} \cdot \delta p \quad (2.15)$$

### *Discrete charge transfer*

The charges of the TDI-CCD are moved step wise while the movement of the object is linear. This discrete movement of the signal charge of the TDI CCD also results in 1 pixel blur in the TDI scan direction and can not be prevented.

### *Modulation transfer function*

The MTF or spatial frequency response (SFR) is the magnitude of the optical transfer function (OTF) of the scanning system and is defined as.

$$|\text{OTF}| = \text{MTF} = \frac{|\mathbb{F}\{s(f)\}|}{|\mathbb{F}\{s(f=0)\}|} \quad (2.16)$$

The reduction of the total MTF due to pixel overlap can be calculated<sup>69</sup> with the product of all MTFs equation 2.18. Considering the Fourier transform  $S(f)$  of the spread function  $s(x)$  of the detector effective sampling aperture

$L$  ( $L_{\text{aperture}}$ ,  $L_{\text{align}}$ ,  $L_{\text{velocity}}$ ,  $L_{\text{magnification}}$ ,  $L_{\text{discrete}}$ )

$$\text{MTF}(f) = \frac{\sin(\pi \cdot f \cdot L)}{\pi \cdot f} \quad (2.17)$$

$$\begin{aligned} \text{MTF}_x &= \text{MTF}_{\text{apertureX}} \cdot \text{MTF}_{\text{magnification}} \cdot \text{MTF}_{\text{discrete}} \\ \text{MTF}_y &= \text{MTF}_{\text{apertureY}} \cdot \text{MTF}_{\text{align}} \end{aligned} \quad (2.18)$$

To determine the degradation of the resolution due to all these factors the modulation transfer function (MTF) was measured for the entire optical system. It shows the difference in degradation between the camera operating in frame transfer mode, TDI mode with fixed line rate triggering, TDI mode with encoder, and the theoretical model of the OTF.

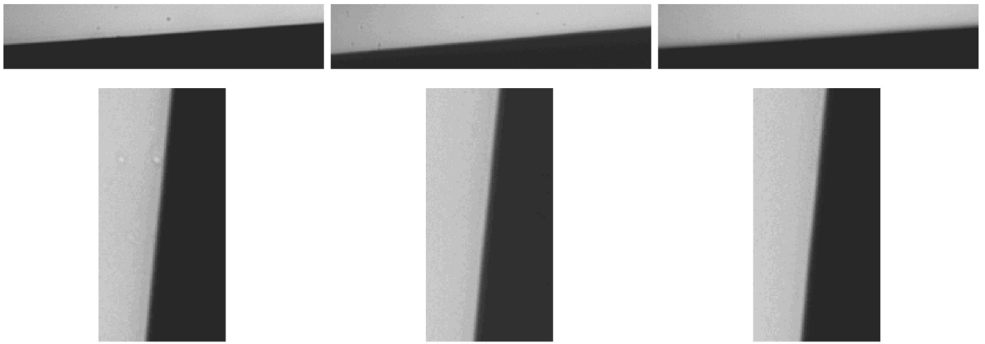


**Figure 2.1.12** First row slanted step edge forward scan direction, second row slanted step edge horizontal direction. Correspondingly for frame transfer mode, TDI mode with encoder triggering and TDI mode with fixed line rate triggering. The images show a reduction of the high frequency content which are filtered out by the complete optical system. This results in a reduction of the resolution. Based on these images the modulation transfer functions can be calculated.

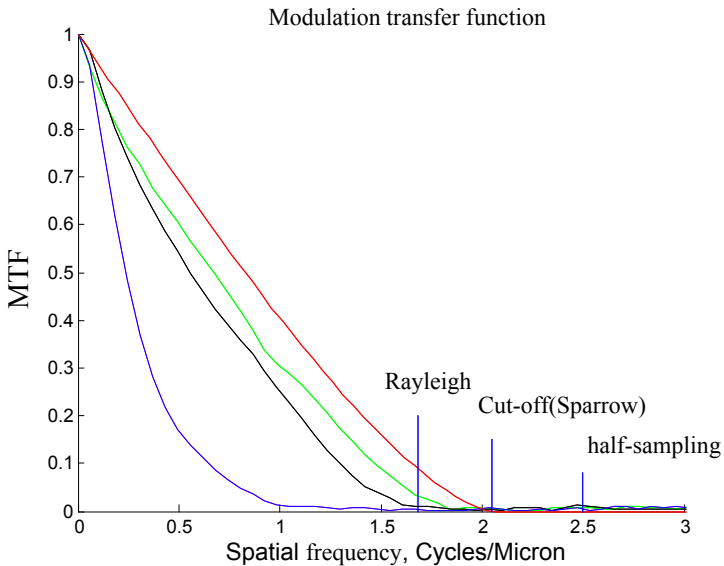


**Figure 2.1.13** MTF of the optical system in the forward (scan) direction.  
 Red line: Theoretical MTF of a 0.6 NA objective at 580 nm.  
 Green line: MTF with camera in area scan mode 205 ms integration.  
 Black line :MTF with camera in TDI mode and encoder triggering at 1 mm/s  
 Blue line : MTF with camera in TDI mode and fixed triggering at 1 mm/s.

To obtain the MTF<sup>71,72</sup> of the TDI scanning system a cartridge with a slanted step edge was imaged. This cartridge was filled with an Acridine Orange solution and the upper surface had nickel lines to mask the fluorescence of the Acridine Orange. The slanted step edge as shown in figure 2.1.12 is imaged under an angle of ~5 degrees parallel and perpendicular to the scan direction to determine the MTF in both directions. To image the Acridine Orange layer the green laser line was used for illumination in combination with a 580DF30 (Omega Optical Inc. Brattleboro,VT) band pass filter. The images were analyzed with Matlab and a Slant Edge Analysis Tool sfrmat 2.0<sup>73-75</sup> resulting in an MTF curve of the optical system at a wavelength of 580 nm as shown in figure 2.1.13 and 2.1.14.

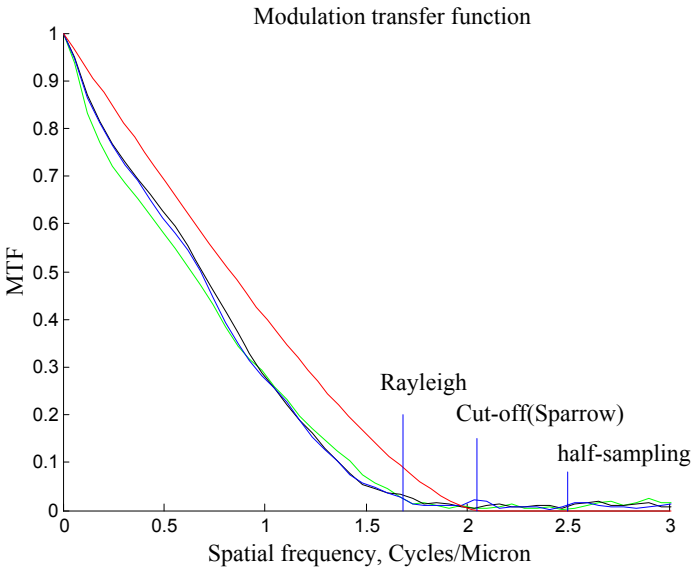


**Figure 2.1.14** MTF of the optical system in the horizontal direction.  
 Red line: Theoretical MTF of a 0.6 NA objective at 580 nm.  
 Green line: MTF with camera in area scan mode at 205 ms integration per frame.  
 Black line :MTF with camera in TDI mode and encoder triggering at 1 mm/s  
 Blue line : MTF with camera in TDI mode and fixed triggering at 1 mm/s.  
 At 1mm/s each TDI row is integrated/illuminated for 204.8ms.

As shown in figure 2.1.13 the scanning system has a slightly lower MTF in the vertical direction when scanning in TDI mode (black line) with encoder triggering as compared to the images acquired in frame transfer mode (green line). This is due to the pixel blurring. This results in approximately 10% decrease of resolution and is hardly visible. Scanning with a fixed line rate of 5 KHz at an average speed of 1 mm/s shows already severe degradation and results in approximately 60% decrease in resolution. This is primarily caused by a mismatch between stage and

camera position. The MTF in the horizontal direction is approximately equal for all camera modes. It shows some minor deviations, probably caused by small variations in focus position, and slight variations and impurities of the nickel line-acridine orange step edge.

## 2.1.6 Scanning system

### *Position control*

The CellTracks TDI system was primarily designed to analyze cell samples positioned in an Immunicon magnetic sample presentation cartridge (MagNest). However traditional fluorescence microscope slides with labeled cells may also be used to present the cells in the focal plane of the objective. To scan the complete analysis surface, the sample is moved in the X and Y direction with the use of two stacked M-605.2DD servo stages (Physik Instrumente, Karlsruhe, Germany). These stages have a maximum speed of 50 mm/s and a travel range of 50 mm resulting in a total area of 2500 mm<sup>2</sup> that can be covered with the use of both stages. This is sufficient to cover the complete area of a microscope slide or an Immunicon sample cartridge as shown in figure 2.1.15a and b

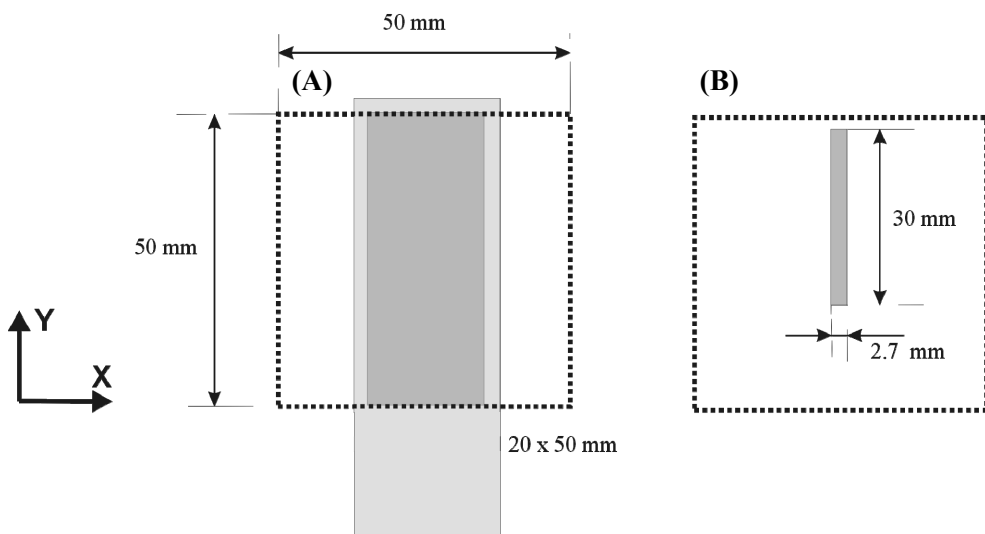


**Figure 2.1.15** Scanning area; The dotted line indicates the limits of the XY stages and the dark gray area the location of the sample.

**A)** Microscope slide

**B)** Immunicon magnetic separation sample cartridge

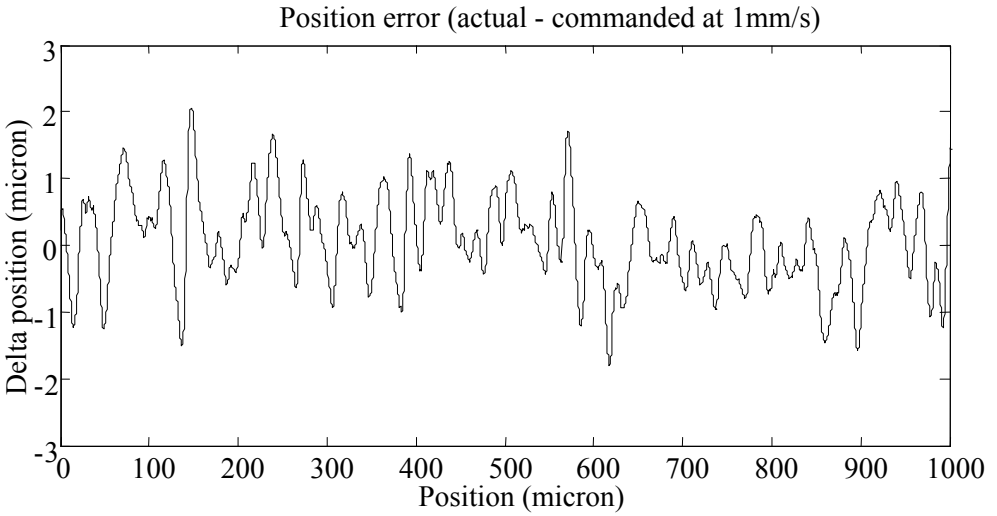


**Figure 2.1.16** Position error during a linear movement of the stages at 1 mm/s. The actual position fluctuates around the commanded position with a standard deviation of 0.8 micron. At a lower scan speed this variation is reduced and has an absolute positioning repeatability of 0.2 micron (Static).

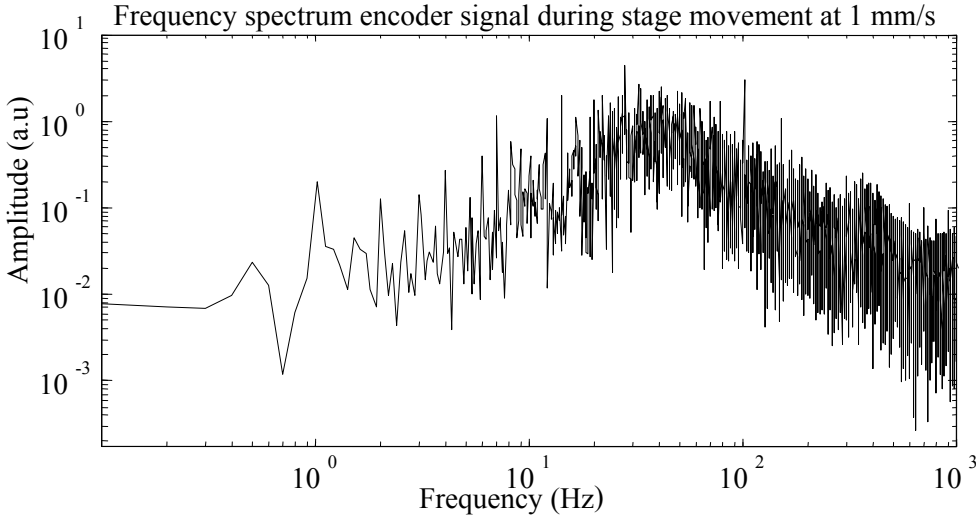


**Figure 2.1.17** Frequency spectrum during a linear movement of the stages at 1 mm/s. The system has a resonance peak around 40 Hz.

The initial positions of the stages are determined with a build in reference position at the center position of the stages. The actual vertical and horizontal positions of the stages are determined with two built in encoders with a resolution of 0.1 micron. Each stage has an absolute positioning repeatability of 0.2 micron over the complete scanning range. The encoder signals are used to control the servo motors of the stages with a PID – controller C-843.20 (Physik Instrumente) to follow a precise trajectory. As shown in figure 2.1.16 and 2.1.17 the stage moves around the commanded position with a standard deviation of 0.8 micron and a frequency of 40 Hz during a linear movement.

**Focus control**

The cartridge surface where the cells are presented does not lie perfectly horizontal. The chamber surface may be skewed, as result of which a different focus is needed for each position. To maintain a proper focus in the Z-direction during a scan of a complete chamber the focus should be adjusted. Prior to a scan the focus is determined at 9 or more positions and a 2<sup>nd</sup> order fit is used to estimate the proper focus for the complete scanning area. To adjust the Z-position a piezo microscope objective positioner MIPOS 500 (Piezosystem Jena GmbH, Jena, Germany) shown in figure 2.1.18b, is used.

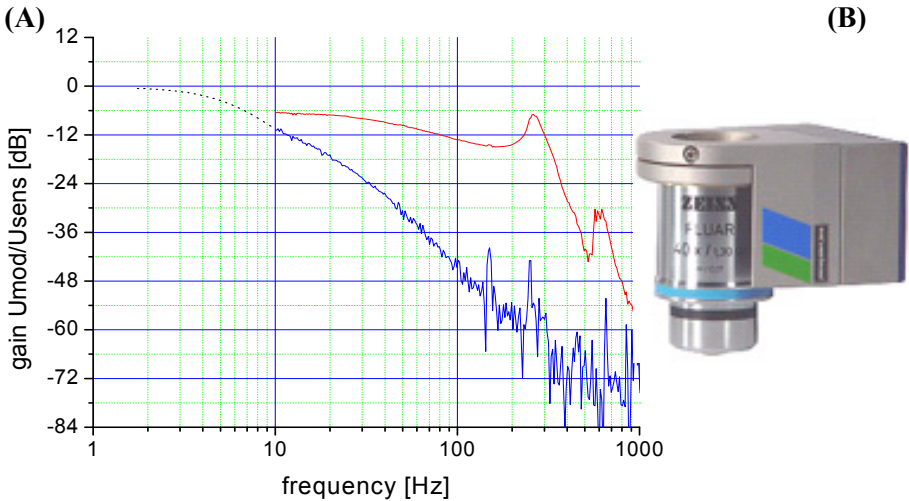


**Figure 2.1.18** Characterization of piezo microscope objective positioner.

**A)** Frequency response of the piezo objective positioner. Red line in open loop mode and blue line in closed loop mode, both with microscope objective (~202 gram). **B)** Piezo microscope objective positioner MIPOS 500

The measured frequency response shown in figure 2.1.18a has a resonance peak at 275 Hz in open loop. In closed loop a strain gauge measures the position and the actuator NV40/1CL (Piezosystem Jena GmbH, Jena, Germany) uses a PID feedback loop to produce a linear output. The range is 0 - 400  $\mu\text{m}$ , with 35 nm precision and a non-linearity of 0.06% in closed loop, The precision and accuracy are much smaller than the depth of field of 1.6  $\mu\text{m}$ . (Equation 2.2.21 ( $\lambda=580$ )). The maximum positional change of the focus observed is 5  $\mu\text{m}/\text{mm}$  and is well within the bandwidth when scanning at a speed of 1 mm/s. The range is sufficient to cover a complete scanning area.

### Counter

During scanning of a sample the encoder signal is also used to synchronize the stage movement with the line trigger of the TDI CCD. The encoder signal of the stages has a resolution of 0.1 micron. However the sampling resolution should be smaller than the Nyquist rate<sup>76,77</sup>. This is twice the cut-off frequency in the lateral direction of the optical system and is defined as:

$$\frac{1}{2} \cdot \Delta_{cut-off} = \frac{\lambda}{4 \cdot NA} \quad (2.19)$$

This results in a minimal sampling distance of 0.242 micron at 580 nm. To obtain a square pixel image with the used TDI CCD and encoder an appropriate sampling distance of 0.2 micron is used. The total magnification of the setup is therefore set to 32.25X. To create a corresponding trigger pulse for the camera the encoder signal is counted with the counter<sup>78</sup> shown in figure 2.1.19. It generates 1 trigger pulse for k =1,2,3,4, or 5 encoder pulses resulting in a sampling resolution of 0.1, 0.2, 0.3, 0.4 or 0.5 micron whereas the resolution of the encoder is 0.1 micron. Therefore we used k=2 resulting in a sampling resolution of 0.2 micron.



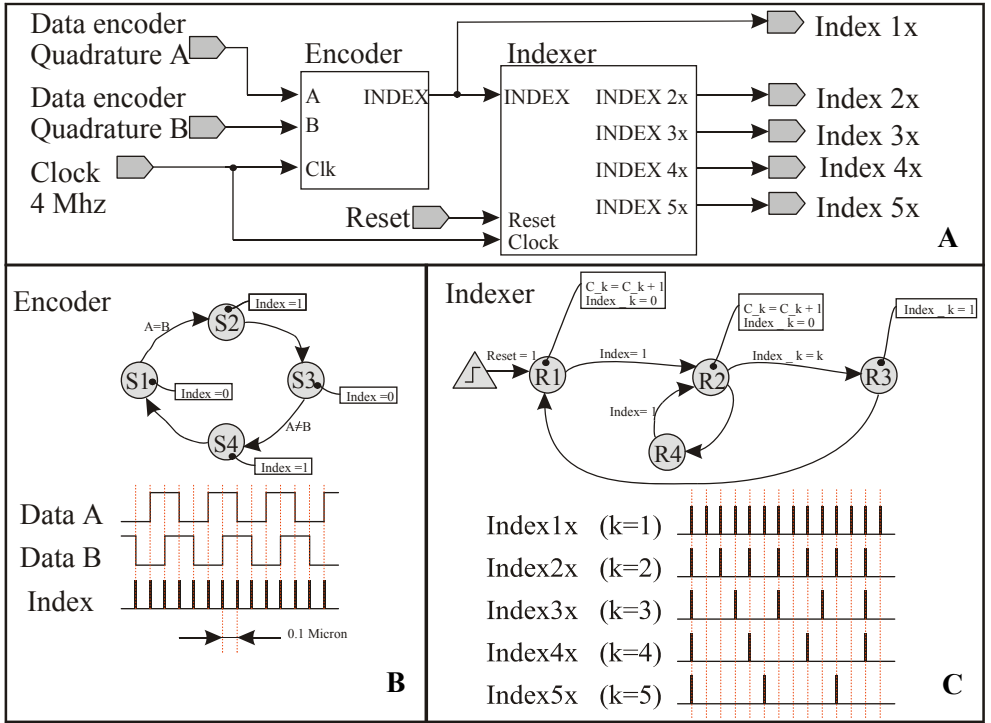


**Figure 2.1.19 a)** Counter logics overview **b)** encoder **c)** Indexer

The counter logics shown in figure 2.1.19 are programmed in an ispMACH4A M4A3-64 programmable lattice chip (Lattice Semiconductor Corporation, Hillsboro, OR) that uses a 4 Mhz clock to change the state. The state flow diagrams figure 2.1.19 b and c show the direction and the conditions to go to the next state and the corresponding output. To generate 5 different indexes the chip is programmed for 5 different index outputs, resulting in sampling resolutions  $\delta s$

$$\delta s = \delta e \cdot k \quad k = 1, 2, 3, 4, 5 \quad (2.20)$$

where  $\delta e$  is the encoder resolution.

### ***Stage-camera synchronization***

To characterize the stage-camera synchronization the trigger signal is measured as shown in figure 2.1.20 directly from the counter with a DAQ card that measures the duration between each trigger pulse.

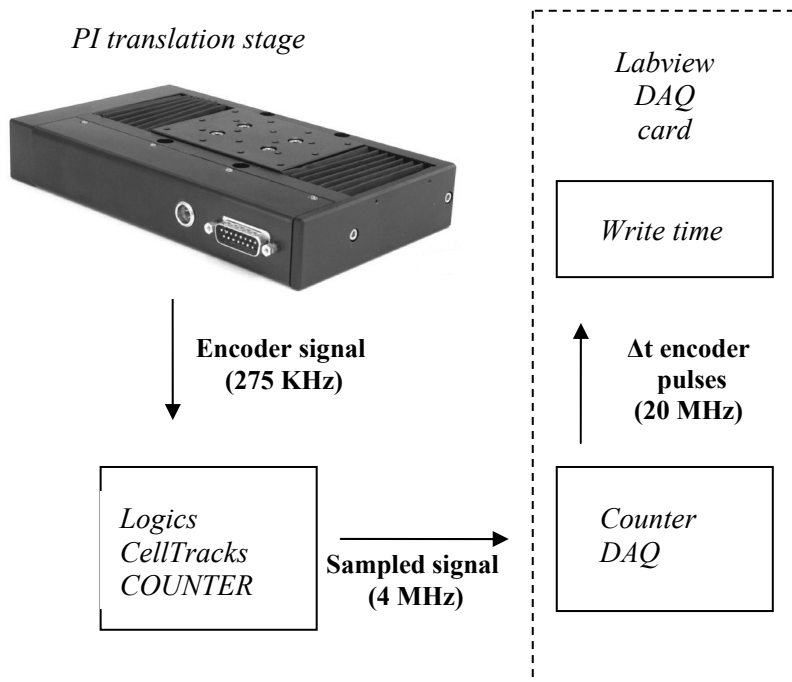
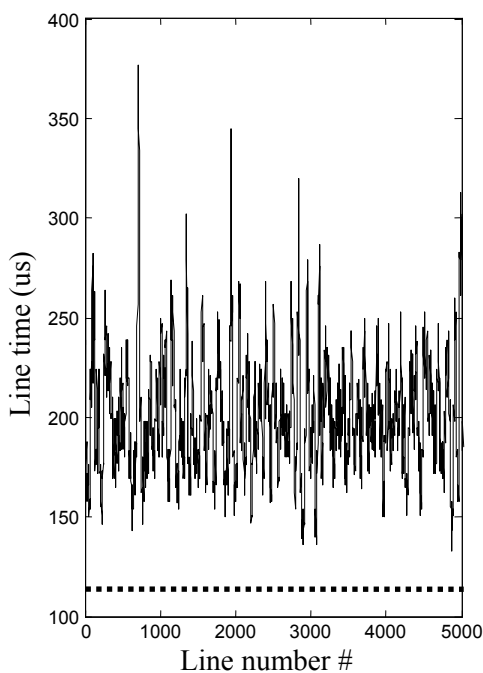
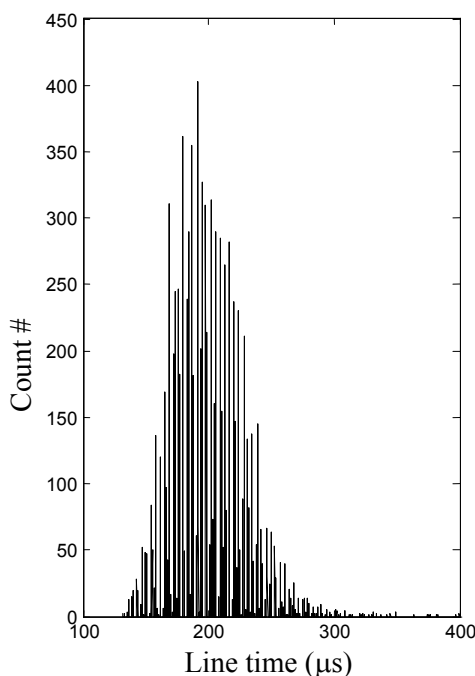


**Figure 2.1.20** Measuring encoder pulses to characterize stage camera synchronization. Encoder pulses are sampled with 275 KHz at the stage and re-sampled with 4 Mhz with a counter generating a pulse for k counts output. A DAQ card is used to measure the delay between each counter pulse with a sampling rate of 20 Mhz.

As shown in figure 2.1.21a and b the average line time is  $199.8 \mu\text{s}$  with a standard deviation of  $30 \mu\text{s}$ . The discrete steps in the histogram are caused due to the sampling at 275 KHz, 4 MHz and 20 MHz. The blue line in figure 2.1.21a indicates the lower limit of the line time which is at  $113.6 \mu\text{s}$ . Line times below the lower limit result in an incomplete readout of the camera and should be prevented, therefore the maximum scan speed when using an encoder is approximately 1-1.2 mm/s and is always below 1.76 mm/s which is the maximum speed which can be obtained when using our camera and a constant line trigger. To scan faster, while using an encoder, a smoother stage motion is required to minimize fluctuations in the line time.



**(A)** Line Time \ TDI stage at 1 mm/s



**(B)** Histogram line time at 1 mm/s

**Figure 2.1.21** Variations in the line time are caused by small variations in stage velocity, sampling uncertainty and non-uniformity of encoder grid.

**A)** Line time when scanning with a speed of 1mm/s.

**B)** Histogram of line time at 1 mm/s

### ***Integration time***

When the stage is moving at an average velocity of 1 mm/s the camera is triggered and the line times vary as shown in figure 2.1.21. As the total signal detection of the TDI camera is summed over 1024 TDI columns the resulting integration time is 204.6 ms  $\sim$  4.9 Frames /second (1024 x 1344) as shown in figure 2.1.22. The standard deviation of the moving average of the line time is 1 ms. A variation of 0.5% in the quantification of the signal due to variations in the integration time can therefore be expected when scanning at 1 mm/s.

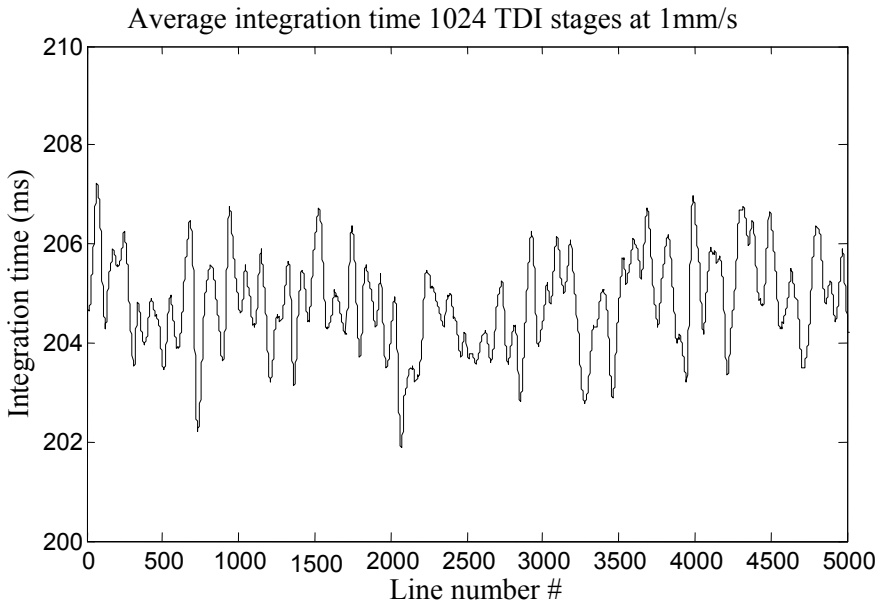


**Figure 2.1.22** Averaged integration time when scanning at a speed of 1mm/s, variations in the line time are averaged over NTDI stages resulting in a standard deviation of 1 ms and a mean integration time of 204.6 ms.

## 2.2 Instrument – Control

### 2.2.1 Introduction

The CellTracks TDI system introduced in the previous chapters, is a fully automated scanning image cytometer. To operate the system and let all different parts function in the proper manner, a dedicated software package is needed to control the hardware and the data acquisition. Several software packages are available on the market like Visual Basic, C++ and LabView. We have chosen to write the program in LabView (Lab Virtual Instrument Engineering Workbench) from National Instruments Corporation (TX, USA). LabView is a graphically oriented programming language that is highly flexible and intuitive. It has many mathematical subroutines and supports an extensive amount of instrument drivers to control hardware. These features make LabView an appropriate software programming language for our purposes. The program written is flexible and can easily be adjusted and improved to accommodate different hardware components. Image analysis is performed after data acquisition. We use the freeware Java program ImageJ<sup>79,80</sup>, which is more flexible than LabView to analyze the very large amount of image data. Typically a complete cartridge scan comprises 16.1 GB of raw data.

### 2.2.2 Software control

The flowchart shown in figure 2.2.1 gives an overview of the software control of the CellTracks-TDI image cytometer hardware (figure 2.2.4)

When the program is started it first displays a user interface to configure all the hardware settings. When started, the sample is manually inserted and stage positions are initialized according to a fixed reference position of these stages. After initialization the sample is moved to the expected position of the borders, respectively the right, left, top and bottom side of the sample chamber. For each of these positions the actual sample border is determined and the initial stage positions are reinitialized based on these values to exactly center the sample. After determination of the sample border it determines the focus position of the sample at multiple positions. This can be done manually or by an automated focusing procedure. The program next calculates a linear- or polynomial fit to this data. With the obtained data it is assured that images are acquired that cover the complete sample with a proper focus for each position.

After these initializations a front panel is shown with a user interface (figure 2.2.2) which can be used to adjust the scanning parameters and to display the measurement data and settings.

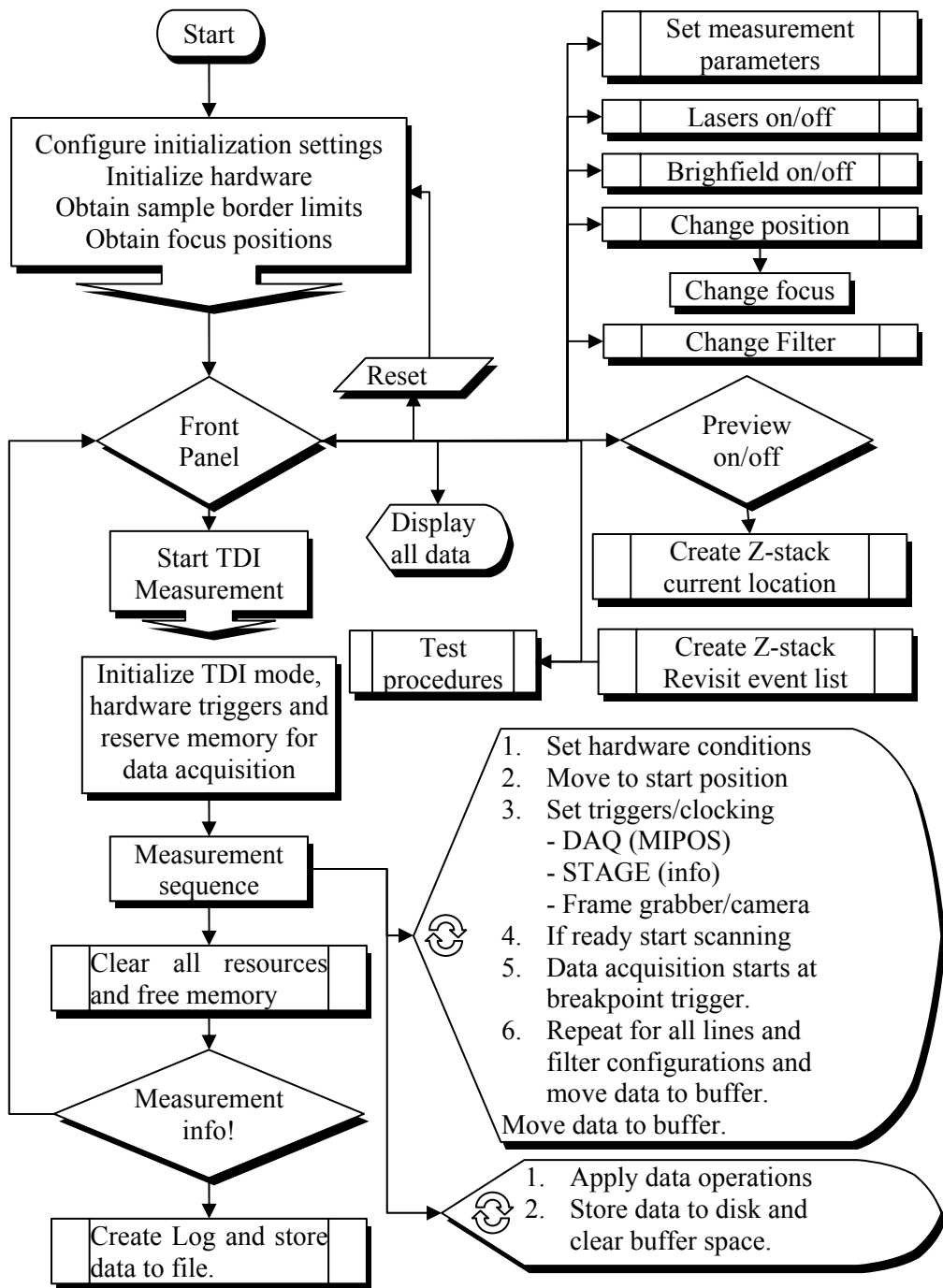


Figure 2.2.1 Flowchart CellTracks TDI scanning software.

By means of the interface shown in figure 2.2.2 the CellTracks TDI system is controlled. Multiple processes can be chosen by setting the parameters for hardware components, data storage and visualization of data.

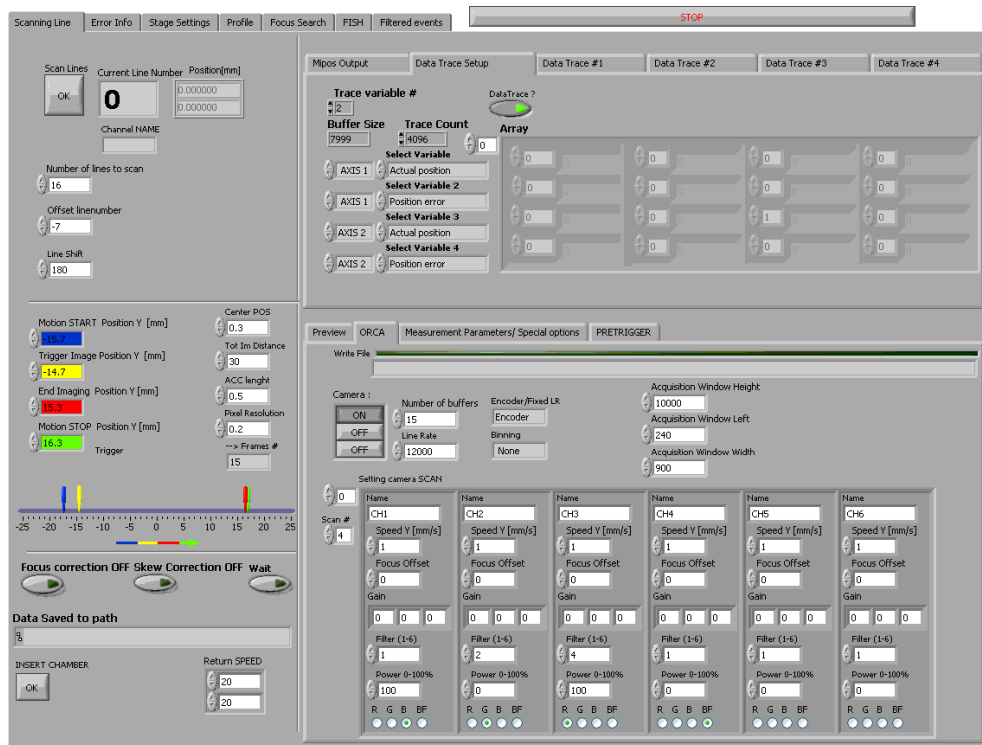


Figure 2.2.2 Front panel for system control and hardware settings.

## TDI Measurement

To perform a completely automatic scan of the entire sample, measurement parameters are chosen. Name, scanning speed, focus offset, camera gain, camera offset, filter setting, brightfield, laser selection and power regulation are all set on the front panel. The sample will be scanned in multiple adjacent strips with a spacing of 180 micron (900 pixels) to cover the complete sample. For each strip (figure 2.2.3a) movement starts in the scan direction from position  $P_1$  and image acquisition starts at  $P_2$ . At  $P_3$  and  $P_4$  image acquisition and movement is stopped respectively.

This scanning of the complete sample surface will be repeated multiple times according to the different parameters set for each channel. A channel is defined as a set of parameters used to obtain images for a specific fluorophore or a brightfield image.

Before the actual measurement starts all the hardware is initialized: A buffer for image data acquisition is reserved, a list with focus positions for the scanning range is generated, and a buffer is reserved to store position info of the stages. The DAQ card starts to generate a 3 kHz trigger signal that is used for the frame grabber and for camera triggering. The same trigger signal is used to clock the analog modulation of the DAQ card that controls the microscope piezo objective positioning system. From this point on, camera, frame grabber, DAQ card, counter and motion control card are waiting until all hardware is ready and all triggers are armed.

Stage movement is then initiated, the stage moves from its start position ( $P_1$ ) and a trigger rises (blue line in fig 2.2.3). This trigger rise indicates movement of the stage. It also indicates the switch from clocking by the DAQ frequency generator to clocking by the encoder signal. When the stage is not moving the encoder signal is not changing, and constant triggering of the camera with the DAQ frequency generator is then required to prevent timeouts and unpredicted behavior.

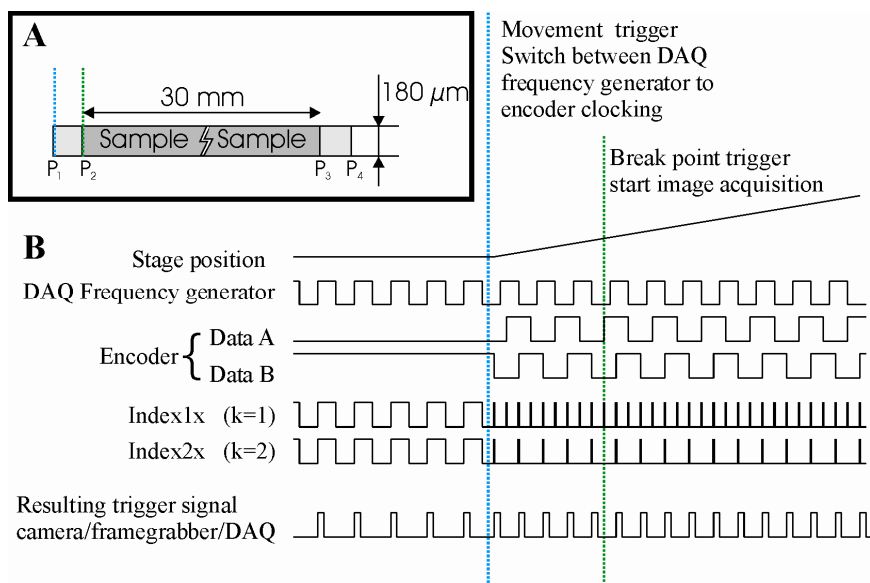


**Figure 2.2.3 A)** Image acquisition of a single stroke,  $P_1$  and  $P_4$  are the start and stop positions for stage movement and correspondingly  $P_2$  and  $P_3$  for image acquisition.

The gray area in this figure indicates the “true” sample area where the cells are located. Image acquisition starts at  $P_2$  this is  $\sim 150$  micron before the sample border and ends at  $P_3$   $\sim 150$  micron after the border of the sample chamber.

**B)** Trigger and clocking signals used to synchronize image acquisition, stage movement and focus position. For each CCD line the camera is triggered by a pulse that is generated when two pulses have been counted with a counter.



The blue line in figure 2.2.2 indicates stage movement at position ( $P_1$ ) and the green line indicates the breakpoint trigger that is initiated by the scanning stage when the desired image acquisition start position ( $P_2$ ) has been passed. Between  $P_1$  and  $P_2$  the stage is accelerating to the requested speed to obtain a constant velocity when passing  $P_2$ . Therefore the distance between the start position and the breakpoint trigger should be at least  $\sim 300$  micron to accelerate the stage to a constant velocity and to dump the first 1024 rows of data before triggering. These first rows contain data with a varying line transfer time resulting in overall larger integration time and should be omitted. When a complete strip of the sample has been scanned the stage shifts to the next strip and the process starts all over again. Subsequently the previously acquired data is rapidly copied into a temporary memory buffer. Simultaneously with the next scan the data of the previous scan is saved to disk to clear the temporary buffer space before the next scan is finished. In this way a continuous scanning of the sample is obtained with minimal overhead time.

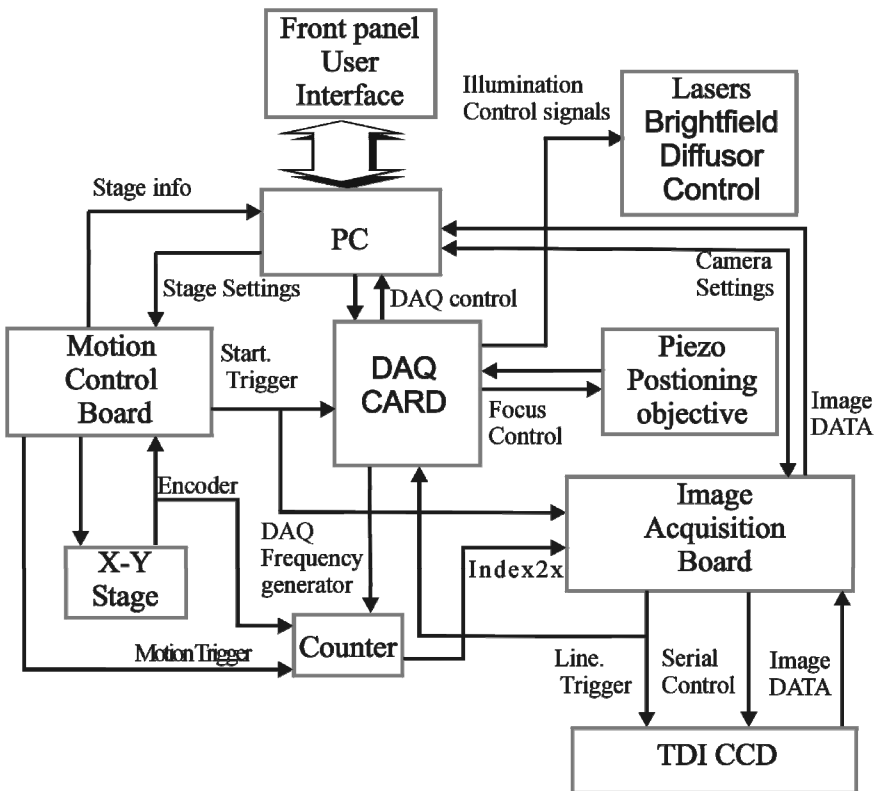


**Figure 2.2.4** Diagram with hardware control, trigger and clocking signals used to synchronize image acquisition, stage movement and focus position.

## Preview image

From the system control interface a preview panel (figure 2.2.5) can be opened. The system then operates as a microscope and the panel shows an image of the current sample location. This image can be used for alignment of the system and to examine the sample prior to, or after, a complete scan of the sample. In this mode a sample position is recorded continuously with the camera operating in frame transfer mode. During the preview lasers, brightfield LED, filters and sample position can be adjusted with the frontpanel menu to examine the complete sample at different laser excitation- and filter settings. From the preview window a snap shot of the current image can be captured and saved to disk. Also multiple images can be recorded, as needed for time laps studies, or to acquire a stack of images to generate a 3D image. During a time laps experiment images are recorded with a specified interval. The lasers can be turned on and off automatically when using large time intervals to prevent unnecessary bleaching. After a time laps experiment the images are stored to disk and the system returns to normal preview operation. To obtain a 3D image of an event the objective is moved along the Z-direction by the piezo positioning system in steps with a specific size. The distance above and below the predetermined focus position between which the scans have to be made, are also specified. An image is stored for each layer to create a Z-stack.

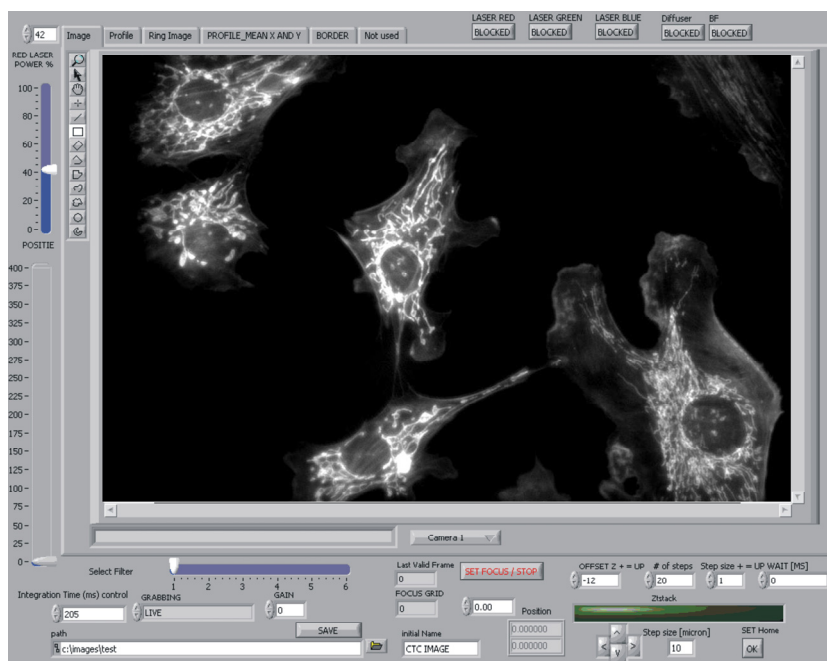


Figure 2.2.5 Panel with preview for manual inspection.

## 2.2.3 Feed forward steering and focusing

### *Introduction*

When a complete chamber is scanned, the focus position has to be continuously adjusted. Typically the chambers used show a linear variation of the focus position due to a small tilt of the glass surface. This ranges from 1 to 5  $\mu\text{m}/\text{mm}$  and 30 to 150  $\mu\text{m}$  for the complete chamber. The field of view of the homogeneous illumination area on the camera is 180x180 micron and therefore the maximum variation of the focus in a single image is 0.9 micron. The depth of field<sup>81,82</sup> or axial resolving power of a microscope objective is given by:

$$\Delta_{axial} = \frac{\lambda \cdot n}{NA^2} \quad (2.21)$$

In our “CellTracks-TDI” setup this results in a depth of field of 1.6 micron at 580 nm. The maximum variation of the focus is well within the depth of field, and the sample will look in focus over the whole field of view. Larger variations in cell images are more likely to arise from variations in cell/nucleus size than from the tilting glass surface.

### *Feed forward*

To ensure that each cell is properly in focus during a scan of a complete chamber, multiple (usually 9 or more) focus positions are determined (see below) at multiple locations on the chamber surface (figure 2.2.6). This dataset is interpolated by a 2<sup>nd</sup> order fit to obtain proper focus at each intermediate sample point, using a feed forward control while scanning.

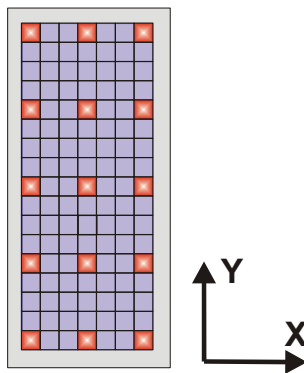


**Figure 2.2.6** Focus positions are determined along a linear grid over the sample surface.

### ***TDI Focus method***

For automated scanning microscopy a reliable and fast focusing system is desirable. Different systems are in use. Most of the automated microscopes make use of image contrast to determine a focus score (contrast as function of the Z direction). This is usually done by acquiring multiple images for a full range of focus settings. Then an algorithm is applied that first determines a coarse focus and next converges to a fine focus. At the peak of the focus score a linear or quadratic fit is used to estimate the correct focus position. The focus score measured in microscopy comes from the image contrast of the objects in brightfield/darkfield illumination and from fluorescence<sup>83-86</sup>. In the case of brightfield illumination the number of photons collected is high enough to achieve a high signal to noise ratio (SNR). The SNR is low for most images acquired with fluorescence, due to the relatively low light levels. They require longer integration times which slow down the focusing procedure.

A disadvantage of these methods is also the need of an object that can be imaged. When using larger magnifications and for specific samples, not all the positions may contain an object. Consequently focusing at a neighboring position is required until an object is found. This further slows down the focusing process.

The method that is introduced here makes use of the intrinsic properties of a camera operating in TDI mode. Instead of moving the sample to obtain a smooth image, the sample is kept standing still. A through focus series is made by continuously moving the microscope objective from 0 to 400 micron while the TDI camera is triggered with a fixed line rate. During this acquisition the actual position of the microscope objective is measured when a line of the TDI camera is triggered. Examples of images obtained are shown in figure 2.2.7 for different samples and illumination methods.

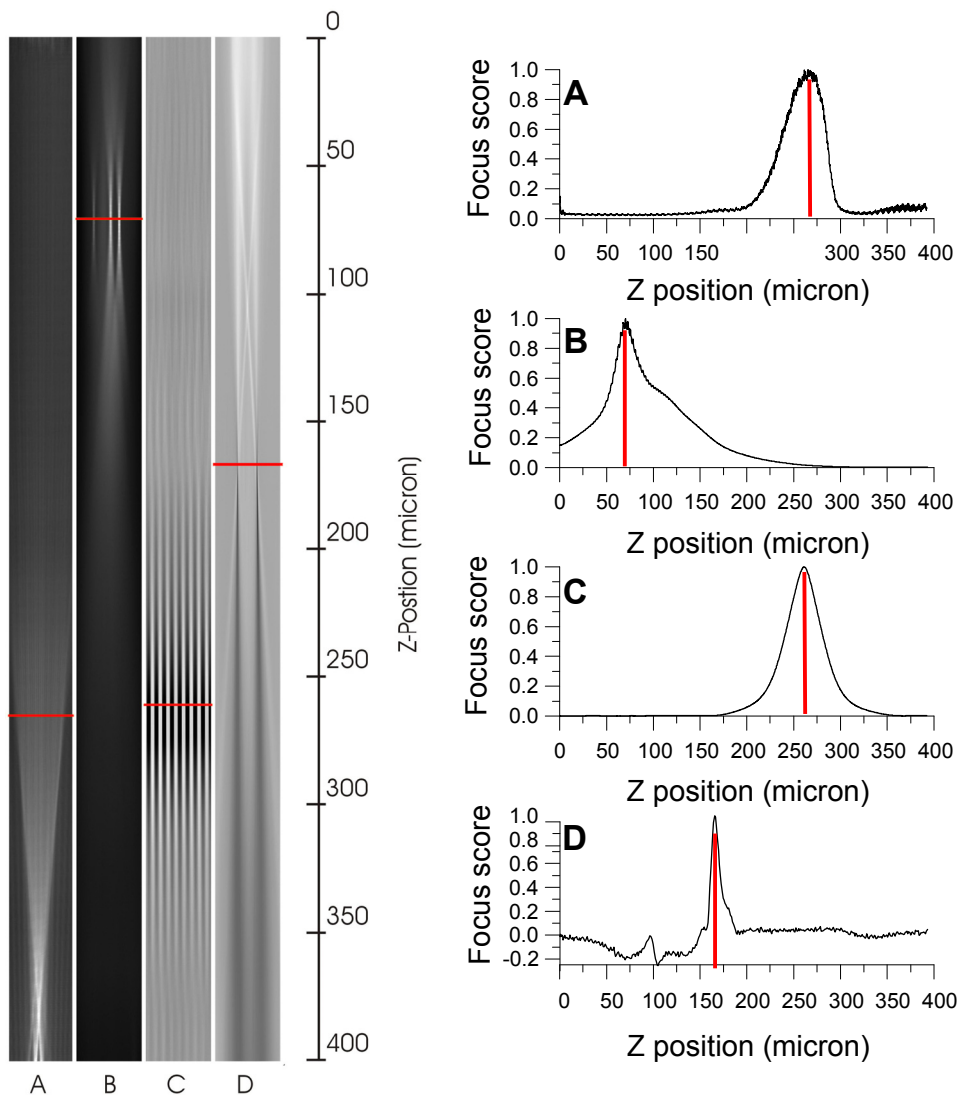


**Figure 2.2.7** Focus images acquired with a TDI camera while the microscope objective position is moving axially from 0 to 400 micron, and the sample is not moving in the lateral direction. Different ways of determining a focus score are shown. For each method the corresponding focus score is shown in the right hand figures. The red lines indicate the estimated focus positions. **A)** Reflection of the square laser spot on the glass surface where the cells are positioned. **B)** Fluorescence from nuclei stained with DAPI. **C)** Brightfield image of the parallel nickel lines structure. **D)** Brightfield image of a grooved structure.

The X direction shown in figure 2.2.7 contains the lateral image data sampled with a resolution of 0.2  $\mu$ m of the object. The Z-direction is sampled with 0.02

$\mu\text{m}$ . So for each line the microscope objective is moved with  $0.02 \mu\text{m}$ . Due to the TDI operation and a camera with  $N_{\text{TDI}} = 1024$  rows, each pixel line is the moving summation covering 1024 focus positions over a range of  $1024 \times 0.02 = 20.48 \mu\text{m}$ .

$$P_{X,Z} = \sum_{Z=i}^{i+N_{\text{TDI}}-1} p_{X,Z} \quad (2.22)$$

This principle was tested for 3 different chamber types. Figure 2.2.7c is a sample chamber with thin parallel nickel lines on the glass surface. Figure 2.2.7d is a sample chamber with a grooved surface that was made from PDMS. Both configurations are used to align cells in straight lines at the chamber surface. The data shows that for this cell orienting surface good contrast under brightfield illumination is obtained. Therefore each of these structures (without cells) may be used as a reference for the focus position. For most of the samples measured we used sample chambers with a flat glass surface. For these sample chambers focusing is done using the contrast of the fluorescence staining of the objects (figure 2.2.7b) or using the reflection of the square laser spot (figure 2.2.7a). This reflection from the square laser spot, as described in chapter 2.1, comes from the lower glass surface and ferrofluid particles at the top surface. When the laser spot is focused at this surface the reflection shows a steep edge at the sides of the flat-top. Using this reflection at the glass surface offers several advantages above the use of fluorescence. There is no need to have an object for the focusing procedure and it is a measure of the position of the glass surface rather than the position of the object used for focusing. Furthermore the focusing speed is limited by the maximum acquisition rate of the camera rather than by the amount of photons, as the amount of reflected photons is high enough to obtain a large SNR.

### ***Focus score***

The method finally used is based on the reflection of the laser spot. The focus score is calculated from figure 2.2.7a by averaging over 10 pixels in the Z-direction and calculating the variance in the X direction. For the calculation only a small part of the through focus series, of typically 60 micron around the fixed position of the steep edge, is used. This is repeated for each line in the Z-direction. The resulting variance for the entire range is normalized and a detection algorithm is used that fits a quadratic polynomial to the peak. This data point is related with the known position of the microscope objective. The actual position at the glass surface has an offset of  $(1024 \times 0.02)/2 = 10.24$  micron while the position readout is related to the last output line of the camera. This line is based on the previous summation of TDI rows and is therefore 512 lines delayed. Repeated measurements at two locations show typically a standard deviation of 0.3 micron for the focus estimation. The estimated focus position is based on the glass surface and the cells/objects of

interest are positioned underneath this surface. The diameter of leukocytes ranges from 6 to 10 micron and for CTCs from 4 to 40 micron. An optimal focus condition for these cells is approximately achieved when focus is at the center position of the cells. However this varies for each cell. Typically the (APC-CD45) leukocyte marker images were focused 5 micron underneath the glass surface and the PE-CK images 8 micron respectively, since most of the CTCs are slightly larger than the leukocyte population.

In figure 2.2.8 the position of the glass sample chamber is measured for 60x5 focus positions. The glass tilt is approximately 4.3 micron/mm in the Y-direction and 3.0 micron/mm in the X-direction.

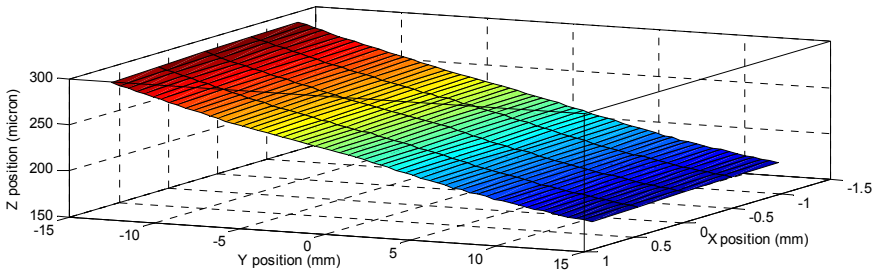


**Figure 2.2.8** Sample chamber surface measured for 60x5 focus positions.

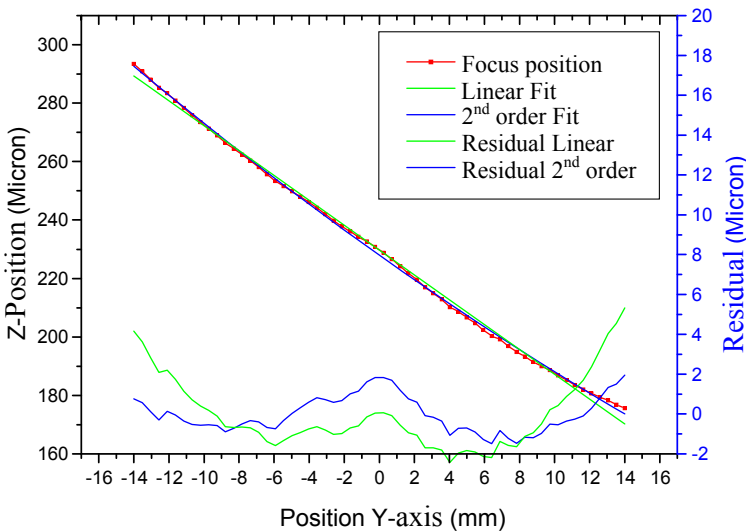


**Figure 2.2.9** Focus positions at the centerline of the cartridge and the residuals of linear and 2<sup>nd</sup> order polynomial fits of the measured position data.

The linear residual shown in figure 2.2.9 indicates that the glass surface is also slightly curved besides the initial tilt. Although the sample chambers are all a bit different, typically most chambers bend downwards in the center.

In order to scan a complete sample chamber and to minimize the amount of focus positions, a 3x3 focus position grid is used (fig. 2.2.6) and the focus positions are estimated with a 2<sup>nd</sup> order polynomial fit. This results in a standard deviation of the focus positions of approximately 1 micron. This is still within the depth of field of the microscope objective and variations due to object size. More accurate positioning would require a larger focus grid and interpolation with a higher order polynomial or spline fit; consequently this would take more focusing time and this is not always wanted. The time needed to measure, calculate and reposition is for a 3x3 grid approximately 30 seconds, where most of the time is consumed by the measurement itself, ~2.3 seconds for a single focus image. Further time reduction would be possible by measuring the focus score in multiple steps while converging to the focus position, using smaller frame sizes and a decreasing sampling resolution. Besides this a further reduction could be obtained, by minimizing the focus range, since only small variations in focus can be expected for neighboring positions.

### ***Multi-camera control***

In the current setting each channel is measured one after another and bandpass filters, laser excitation and focus settings are adjusted for each channel. Scanning multiple channels in parallel with multiple cameras could reduce the total acquisition time further. This requires the implementation of dichroic mirrors in the emission path to separate and steer the fluorescence emission of each probe to an additional camera. At moment the acquisition software is already modified to acquire image data of 3 cameras simultaneously. However, the cameras and additional dichroic mirrors are not implemented yet.

### ***Auto focus***

Focus positions are currently determined prior to a scan and focus is adjusted in feed forward. Preferably focus is obtained dynamically and adjusted continuously with a feedback loop. This requires a continuous measure of a focus score and preferably with a direction sign. For this purpose the reflected laser light could be used. In figure 2.2.7a the edges of the scattered laser light are moving inwards and outwards respectively above and below focus. The position of these edges could be used as focus measure. However, scattered laser light is effectively blocked by the emission filters and is not detected during image acquisition. This would require an additional sensor to detect focus variations based on the position of the scattered light. Alternatively dynamic focusing could be obtained with a bright field image using the grooved alignment structure. The structure gives clear contrast and is detected during the initial brightfield scan. Therefore it does not require an



additional sensor. For this purpose, the use of a TDI camera is also an advantage, readout is continuously and small blocks (a small number of lines) of the brightfield image could be processed during image acquisition in real time to obtain a focus score continuously. After the initial brightfield scan the obtained focus values can be re-used to scan the remaining channels with feed forward. Specifically dynamic focusing would be very useful for the Polydimethylsiloxane (PDMS) groove structures. The PDMS is less rigid than the Pyrex glass surface of the traditional cell presentation chambers. This results in a larger and non linear variation of the focus positions. This would require much more focus positions to obtain a reliable and consistent focusing of the sample in feed forward.

## 2.2.4 Data analysis

### *Introduction*

Proper image analysis is one of the most critical aspects for an image cytometer and programming a flawless image analysis procedure can be a very laborious task. In the CellTracks TDI system image analysis is performed with a freeware Java program, ImageJ, which is flexible and easy to adjust. ImageJ contains a large collection of plugins, simplifying the task to write an adequate image analysis algorithm for the large amount of image data from a scan. Typically a complete cartridge scan contains 16.1 GB of raw data.

### *Image analysis of rare cells*

The image analysis program was primarily written to obtain quantitative information for infrequent events, which simplifies data analysis.

This is e.g. the case in the analysis of CTC containing samples, which are stained with Cytokeratin-PE (CK-PE). The Cytokeratin-PE signal is only expressed for a few events in the analysis chamber, typically (~50 to 4000 events). These events are randomly scattered over the complete sample surface. The majority of the image data then consists out of background and a large quantity of non-specifically selected leukocytes. Therefore most image data can be neglected.

The amount of leukocytes that are non-specifically selected may vary a lot from person to person. Whereas “clean” samples may contain only 2000-3000 leukocytes, it may happen that the complete surface is covered by 60.000-70.000 leukocytes. A few of these leukocytes appear to have non-specifically bound dye or are auto-fluorescent.<sup>87,88</sup> But most of the leukocytes primarily have a negative staining for CK-PE and a positive staining for CD45-APC and DAPI. Therefore they are easily discriminated from circulating tumor cells that stain positively with cytokeatin-PE and are negative for CD45-APC.

### ***Image analysis triggering (A)***

The image analysis procedure can be separated in 3 distinct steps as shown in the diagram in figure 2.2.10. The images are first corrected for the background and the illumination profile<sup>89-91</sup>. Each image is multiplied by the inverse of the illumination profile (The average intensity of the profile is normalized to 1). Since these images have been acquired with a TDI camera only a correction is needed perpendicular to the scanning direction which further simplifies this operation. After the image corrections, the images are partly stitched together. Total  $4 \times 15 = 60$  images with a size of  $3600 \times 10000$  pixels are obtained. An adjustable low level threshold is used for the trigger channel to detect all events of interest. Based on the locations and size criteria each event is boxed and stored separately into a multipage TIFF file. The locations detected by the trigger channel are used to box and store the corresponding images in the remaining channels. Furthermore each event position is stored to be used later, as a reference for revisiting when reexamination of a specific event is needed. Typically when analyzing a CTC sample the CK-PE signal is used as trigger, with a threshold level of 50 DN and a minimum size of 3  $\mu\text{m}$  for an object. This drastically reduces the amount of data and filters out all possibly CTC-related candidates. The resulting multipage TIFF files for this type of sample contain respectively the DAPI, PE-cytokeratin, CD45-APC and brightfield images. They usually contain only single events. Doublets or cleaved cells were almost never observed, therefore in CTC analysis there was no need to apply a segmentation algorithm to separate closely spaced cells.

### ***Image analysis measuring (B)***

The following image analysis step creates a mask for each event and channel. Prior to thresholding the image, a Gaussian blurring filter is applied with a radius of 10 pixels to smooth the image. Sub sequentially the image is thresholded with a histogram based Otsu thresholding algorithm<sup>92</sup>. This algorithm determines a threshold level by maximizing the between-class variance of pixel intensity. The resulting binary image is filled and used as a mask for the original image, to define the edges.

The trigger channel, which always contains an event, is used as a template for the remaining channels. Although all channels are treated in the same way, several mask criteria are necessary to assign an appropriate mask for each event in all channels. Typically the DAPI mask should be located within or very close to the cytokeratin in the event. Nuclei from nearby events/leukocytes should be neglected. Furthermore the DAPI perimeter should be smaller than the perimeter of the cytokeratin. Approximately the same criteria hold for the CD45-APC channel.

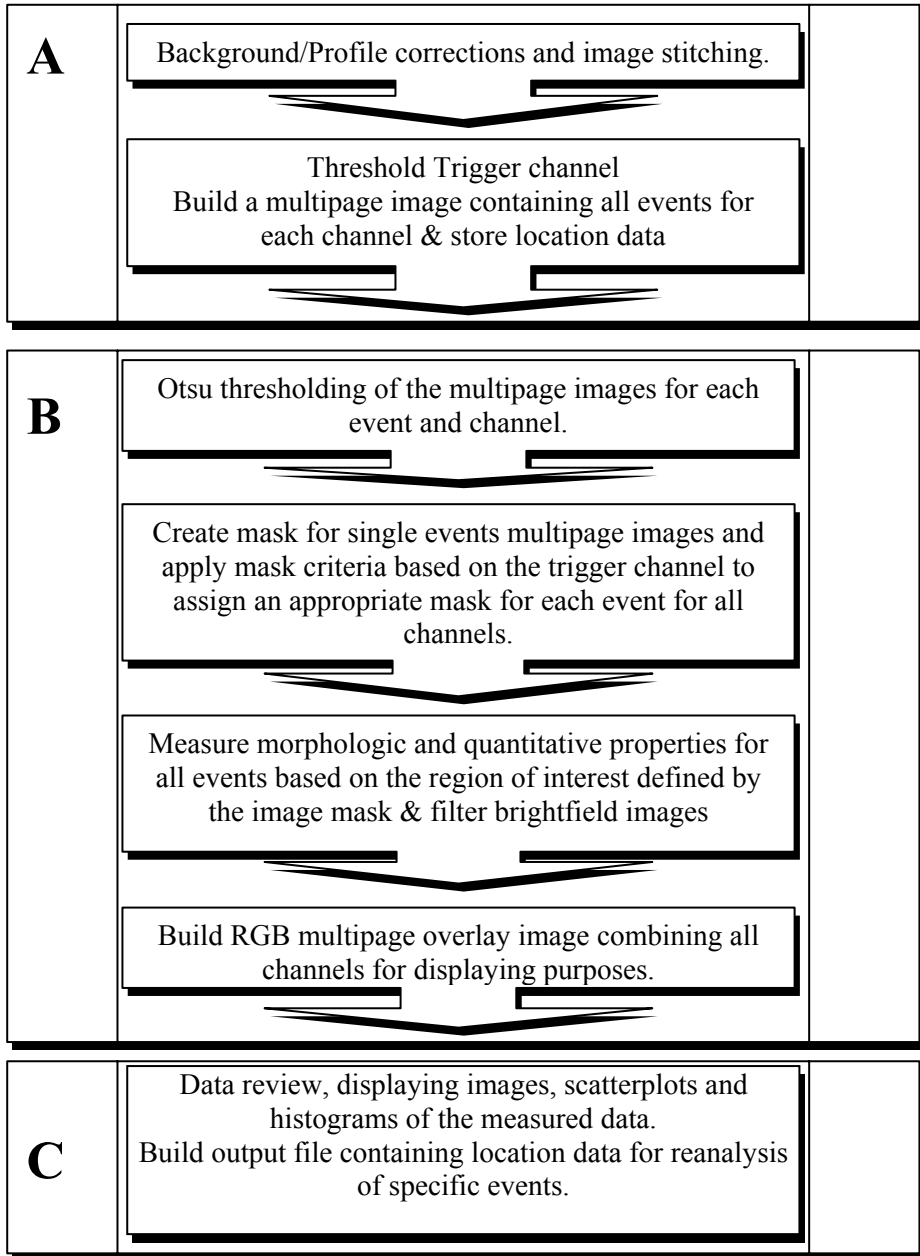


**Figure 2.2.10** Overview image analysis.

**A)** Reduce data and filter out possible events of interest. **B)** Further process reduced data and measure object parameters. **C)** Visualize measured data and obtain information for specific cell populations.

If a signal is present due to non-specific binding it should be nearby the cytokeratin, to prevent the selection of a nearby leukocyte. As a CTC is normally negative for CD45-APC, the signal shown should be close to the background which results in an abnormal low threshold level. In these cases the mask of the trigger channel is applied to select an appropriate mask. The mask for each channel is saved and used as a region of interest to measure quantitative and morphological parameters from the original images. For the brightfield images no mask is applied as they are only used for visual inspection.

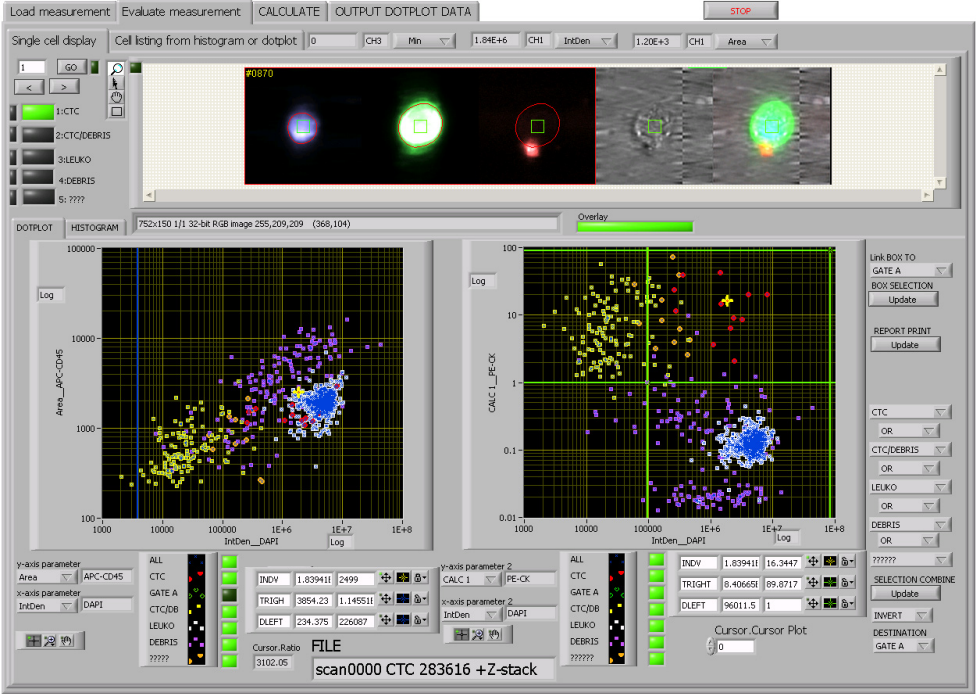


**Figure 2.2.11** Data analysis program.

Measured image parameters are plotted and grouped into defined populations. Within the program a list of events of interest can be selected for further reexamination.

Due to the relatively high ferrofluid content the brightfield images contain a striped pattern. Although this pattern is not directly visible in the fluorescence images, the bright field images are clearly degraded due to the presence of ferrofluid. To improve the visualization of the brightfield images, they are filtered. Whereas the ferrofluid forms straight horizontal lines due to the magnetic field, the image contains in particular mid-high frequencies in the vertical direction of the image. These typical frequencies are filtered out by calculating the Fourier transform of the image, masking the unwanted frequencies followed by an inverse Fourier

transform. Although most ferrofluid can be suppressed, it remains a trade off between ferrofluid suppression and loss of the corresponding spatial frequencies from the actual image of the cell. The bright field image therefore remains difficult to be analyzed for cellular features, but it can be used to identify debris which has in many cases an odd morphology and low transmittance. Removing ferrofluid content of these samples directly improves image quality.

### ***Image analysis displaying (C)***

To quickly review and handle the large amount of data a program was written in LabView to visualize the measured data with dotplots, images and corresponding masks as shown in figure 2.2.11. Based on the images, dotplots and selection criteria of the operator, events can be grouped into multiple populations.

The images originally acquired are in 12 bit grayscale, whereas a monitor typically can display only 256 gray levels and the human eye can only separate 100 gray levels.

To increase contrast, the images are automatically scaled, rather than using the full 12 bit scale, to increase the visibility for the operator. A major drawback is that it is difficult for an operator to deduce quantitative information from these images. A dim nucleus may appear just as bright as a much brighter nucleus. Furthermore a slight difference in monitor settings may already result in a different interpretation by the operator. The dotplots are therefore powerful tools to assist the operator in his/her selection operation. Quantitative information analyzed by the computer is always consistent and eliminates inter-reader variability.

The operator can select from these results a list with events of interest for reexamination. This list can be loaded in CellTracks TDI setup where each event can be revisited to obtain a Z-stack, before and/or after re-labeling the sample.

## **2.2.5 3D Imaging**

After analysis of the data obtained in a scan of the sample, a list is generated with all events. Each event that looks interesting to be observed directly by an operator, or that has to be examined in more detail, can be re-examined.

First the sample is realigned to match the position of the initial scan. Next the camera is set to operate in frame transfer mode and the sample is moved to the position of the event that has to be examined further. Then a step size is chosen and a Z-stack is obtained for all filter configurations (channels). A Z-stack is defined as a set of images of a specific event, each at a different focus position. (Figure 2.2.12) Typically steps of 1 micron are used between each step; this fulfills the Nyquist criterion<sup>76,77</sup> with the used microscope objective.

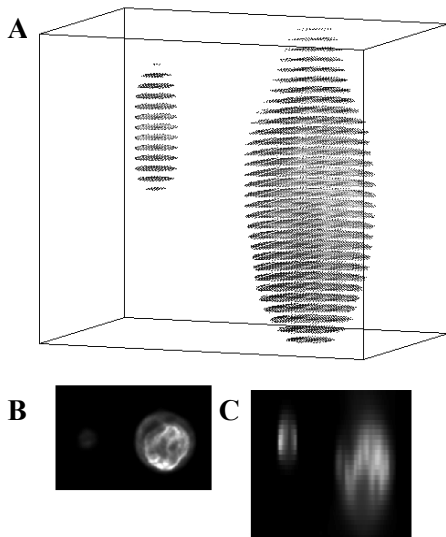


**Figure 2.2.12** Z-stack images are acquired for multiple layers, each at a predetermined distance from its predecessor. The images shown are from a leukocyte and from a relatively large SKBR-3 cell. **A)** Slices **B)** Top view X-Y **C)** Side view X-Z

### *Deconvolution*

To perform a 3D image restoration of the recorded Z-stacks a deconvolution program Huygens professional (Scientific Volume Imaging, Hilversum, The Netherlands) is used. This program uses a deconvolution algorithm<sup>93,94</sup> to remove out-of-focus blur, which effectively brings light back to the source.

The optical system transfers the information from object space to image space. Therefore a point source in the object space will be transferred as a 3D PSF (cone like shape) to the image plane. One may visualize an object as a large collection of many tiny point sources. The sum of all the PSF's of these point sources forms the image in the image plane. Mathematically the information in the image plane is formed by the convolution of the object with the PSF.

In an ideal situation the PSF is also a point source and all information of the object space is transferred into the image space. But this is not the case; during this process information is removed / filtered. When mapping object space into image space, typically high frequency content of the object is lost.

The remedy to this convolution problem is deconvolution, which inverses the convolution. The method used by the Huygens program is an iterative method using the Maximum Likelihood Estimation (MLE).

Particularly when analyzing FISH samples, this method is useful to increase the discrimination of these small objects and to discriminate between nearby lying objects.

## 2.3 Instrument – Characterization

### 2.3.1 Theory: Signal to noise ratio (SNR)

The Signal-to-noise ratio (SNR) describes the quality of a measurement. Specifically, it is the ratio of the measured signal to the overall measured noise at a detector. High SNR is particularly important in applications requiring precise and low intensity light measurements. Major aspects determining the SNR are the properties of the measured sample, the efficiency of the optical system, camera properties, excitation power, magnification, etc.<sup>95,76,77</sup>

Optimal detection with the highest SNR would result in a system with only photon shot noise ( $\sigma_S$ ). However each optical detection system has several noise sources.

Some major noise sources are background noise ( $\sigma_{BG}$ ) and noise arising from readout ( $\sigma_R$ ) of a CCD element. These and other noise sources will be described in the following section. The average noise for a pixel is described as signal spread in terms of standard deviation ( $\sigma$ ) relative to the mean signal ( $\mu$ ) for a pixel.

#### *Photon noise*

Photons incident on the CCD are converted to photoelectrons within the silicon layer. These photoelectrons comprise the signal but also carry a statistical variation in the photon arrival rate at a given point. This phenomenon is known as photon noise and follows Poisson statistics with a square root relationship between signal and noise.

$$\begin{aligned} \text{mean} &= \mu_{\text{SIGNAL}} = N_S \cdot \eta_{\text{eff}} \\ \text{noise} &= \sigma_{\text{SIGNAL}} = \sqrt{\mu_{\text{SIGNAL}}} \end{aligned} \quad (2.23)$$

With  $N_S$  the total amount of signal photons per pixel originating from the sample and  $\eta_{\text{eff}}$  the total efficiency factor (number of photons successfully converted into electrons divided by photons emitted by the initial source). Therefore  $N_S \cdot \eta_{\text{eff}}$  is the total amount of photons per pixel which are hitting the CCD and are converted successfully into an electron.

#### *Readout noise*

Electronic noise sources inherent to the CCD introduce an uncertainty at readout of the signal. These noise components are referred to as read out noise and represent the error introduced during the process of quantifying the electronic signal on the CCD. The major component of readout noise arises from the on-chip preamplifier, due to ineffectively resetting and transferring pixel charges.

$$\begin{aligned} \text{mean} &= \mu_{\text{BIAS}} \\ \text{noise} &= \sigma_R \end{aligned} \tag{2.24}$$

The readout noise is independent of the signal and integration time and is additive Gaussian noise and varies around the bias of the camera. The noise is identical for all the pixels and depends on the readout rate and CCD design. Typically the readout noise ( $\sigma_R$ ) of our camera is 8 electrons,  $\sim 1.7$  DN, per pixel. The mean signal  $\mu_{\text{BIAS}}$  is related to the camera offset and is used to prevent negative values. Our camera uses an offset of 920 electrons  $\sim 200$  DN per pixel. This can be subtracted and doesn't add additional noise.

### **Dark current noise**

Dark noise arises from the statistical variation of thermally generated electrons; these electrons stem from the CCD material itself and are caused by thermal vibrations, once trapped in the CCD well they are indistinguishable from “true” photoelectrons. The dark current noise depends on temperature and is approximately doubled for every 7 degrees increase in temperature. Dark noise ( $\sigma_{\text{DARK}}$ ), also follows a Poisson relationship, and is equal to the square root of the mean number of thermal electrons generated per pixel ( $\mu_{\text{DARK}}$ ) within a given exposure time.

$$\begin{aligned} \text{mean} &= \mu_{\text{DARK}} \\ \text{noise} &= \sigma_{\text{DARK}} = \sqrt{\mu_{\text{DARK}}} \end{aligned} \tag{2.25}$$

The contribution of dark current is very small for our camera, which is cooled down to  $-20$  degrees by a Peltier element. The total number of dark current electrons increases linearly in time; this results in approximately 0.8 electrons/second/pixel. Typically integration times of  $\sim 200$  ms are used and this noise factor is therefore irrelevant.

### **Background noise**

Background noise arises from several sources and originates from the optical system and the sample. Stray light originates from the optical (excitation) system and is caused by scattering of the sample and by reflections at lenses and filters of the optical system. Most of the stray light is Rayleigh scattered and effectively blocked by emission bandpass filters. However a small fraction of the scattered light is inelastically scattered. Raman scattering occurs from the optical components and from the aqueous sample solution. These contributions are not always blocked by the filters, due to a Stokes shift, and may overlap with the fluorescent emission spectra. Other background noise arises from auto fluorescence of the cells and debris in the sample. Furthermore fluorophores which are free in



the solution and are not specifically bound to the cellular objects may also contribute to the background signal. The total contribution of these noise sources is increasing linear with the excitation intensity and the total integration time. Background noise ( $\sigma_{BG}$ ) also follows a Poisson relationship and  $\sigma_{BG}$  is equal to the square root of the mean number of background photons/pixel ( $\mu_{BG}$ ) detected within a given exposure time.

$$\begin{aligned} \text{mean} &= \mu_{BG} \\ \text{noise} &= \sigma_{BG} = \sqrt{\mu_{BG}} \end{aligned} \quad (2.26)$$

### **Signal to noise ratio**

The signal to noise ratio used is defined by:

$$SNR = \frac{\mu_{SIGNAL}}{\sqrt{(\sigma_1)^2 + (\sigma_2)^2 + \dots}} \quad (2.27)$$

where  $\sigma_1, \sigma_2, \dots$  are the standard deviation of the different noise sources.

Taken together, the SNR for a single pixel on the CCD camera is given by the following relation:

$$\begin{aligned} SNR &= \frac{\mu_{SIGNAL}}{\sqrt{\sigma_{SIGNAL}^2 + \sigma_P^2}} = \frac{\mu_{SIGNAL}}{\sqrt{\mu_{SIGNAL} + \sigma_P^2}} \\ \sigma_P &= \sqrt{\mu_{BG} + \mu_{DARK} + \sigma_R^2} \end{aligned} \quad (2.28)$$

$$\mu_{TOTAL} = \mu_{SIGNAL} + \mu_{BG} + \mu_{DARK} + \mu_{BIAS}$$

Where,

$\sigma_P$  = Total of dark noise, readout noise and background noise per pixel.

$\mu_{TOTAL}$  = Total signal [electrons/pixel] which is converted into digital numbers DN with an electron conversion gain of the camera of 4.6 e-/DN

### **Integration time**

The total signal ( $\mu_{SIGNAL}$ ) is determined by the amount of photons which are successfully converted into photoelectrons within a given integration/exposure time. In the case of a TDI camera this integration time ( $T_{INT}$ ) is given by the number of TDI stages and the line rate (2.29). This line rate depends on the used scan speed of the stage, the magnification of the optical set-up and the pixel size of the CCD.

$$T_{INT} = \frac{N_{TDI} \cdot \delta_p}{M \cdot V} \quad (2.29)$$

Where,

$N_{TDI}$  = The number of TDI stages (1024 stages)

$\delta_p$  = The length of a pixel in the TDI direction 0.645 micron

$M$  = Magnification (Size of the image projected on CCD/size of object) which is 32.25x. This results in a sampling distance of 0.2 micron.

$V$  = Velocity of the object [micron/sec]

At longer integration times a higher signal will be obtained and the noise is dominated by photon shot noise. For short integration times the noise is dominated by the readout noise. In the CellTracks TDI setup signal photons are emitted by fluorescent dyes that are attached to the cells. The fluorescent emission will be strongly reduced in time when bleaching of the dyes increases. By consequence  $\mu_{SIGNAL}$  is not increasing linear with time. The result is that at an average (or proper) scan speed (or integration time) fluorescence is the dominant process and a high SNR is obtained. If the scan speed is too low the photon emission rate is strongly reduced before the end of the integration time. The background signal and the dark current will then be the dominating noise contributors as these processes are approximately linearly increasing in time, effectively resulting in a lower SNR.

### 2.3.2 Theory: Dynamic range/Detection limit

The total number  $N$  of pixels per cell is proportional with the size of the cell. In the CellTracks TDI setup a sampling resolution of 0.2  $\mu\text{m}$  is used and each pixel covers 0.04  $\mu\text{m}^2$  of the cell. Cells are round to oval in shape and vary in diameter from 3 to 40 micron. The total number of pixels needed to cover a whole cell therefore ranges from 175 to 31500. To obtain the total signal ( $S_{TOTAL}$ ) from the pixels covering the cell, the values of all these pixels have to be summed (2.30). In the following calculations we assume that the fluorescent signal ( $S_{SIGNAL}$ ) of a particle is constant for a particle which is detected by  $N$  pixels, irrespective of the value of  $N$ .

$$\begin{aligned} S_{TOTAL} &= S_{SIGNAL} + S_{BG} + S_{DARK} + S_{Bias} \\ S_{TOTAL} &= \sum^N \mu_{SIGNAL} + \sum^N \mu_{BG} + \sum^N \mu_{DARK} + \sum^N \mu_{BIAS} \end{aligned} \quad (2.30)$$

The total noise ( $\sigma_T$ ) of a fluorescent cell detected by  $N$  pixels is equal to

$$\sigma_T = \sqrt{N \cdot \sigma_p^2 + S_{\text{SIGNAL}}} \quad (2.31)$$

$\sigma_p$  is the total noise due to dark noise, readout noise and background noise for a single pixel. As shown in this equation the total noise is increased when using more pixels. This results in less total noise for a smaller object, as fewer pixels are used for the same object with the same photon emission  $S_{\text{SIGNAL}}$ . As a consequence the detection limit is raised by increasing N at a constant particle size, or for larger particles carrying the same amount of fluorophores.

### ***Detection limit***

The detection limit<sup>95,96</sup> can be calculated from equation 2.32 and is taken to be 3 times the total noise of the measured object.

$$S_{\text{LIMIT}} = 3 \cdot \sigma_T = 3 \cdot \sqrt{N} \cdot \sigma_p \quad (2.32)$$

The sensitivity is therefore decreased proportional with the square root of the number of pixels covered by the cell. The smaller the objects are, the higher the sensitivity is. However, to identify an object, it is necessary to apply a threshold algorithm to separate it from the background. Each separate pixel has to be above the pixel noise, the minimal detectable signal is therefore given by eq. 2.33

$$S_{\text{LIMIT}} = 3 \cdot \sigma_T = 3 \cdot N \cdot \sigma_p \quad (2.33)$$

Each pixel value is then  $\sim 3$  times the noise contribution in the total pixel value. When comparing 2.32 and 2.33, it is clear that a lower detection limit can be obtained when a separate trigger signal is used that pinpoints to the area/position of the object and acts as a mask for the detection area. This could be for example a brightfield image or a signal from another fluorescent probe. Averaging filters may also be used to find an initial mask, or cell location, of such events with limited signals.

### ***Dynamic range***

The dynamic range ( $D_R$ ) is defined in eq. 2.34 where  $S_{\text{MAX}}$  is the maximum signal of the camera. For our camera the maximum signal  $S_{\text{MAX}}$  is determined by the full well capacity of a single pixel, which is  $\sim 18000e$ - digitized in 12-bit, ranging from 200-4095 DN. The offset of 200 is used as a bias to prevent negative values.

$$D_R = \frac{\sum_1^N S_{\text{MAX}}}{\sqrt{\sum_1^N (\sigma_p)^2}} = \frac{N \cdot S_{\text{MAX}}}{\sqrt{N} \cdot \sigma_p} = \sqrt{N} \cdot \frac{S_{\text{MAX}}}{\sigma_p} \quad (2.34)$$

It shows that the dynamic range of a CCD detection system is increased proportional with the square root of the number of pixels covered by the cell and that the dynamic range depends on particle size.

The maximum signal is limited by the full well capacity. However the theoretical limit of the dynamic range is never obtained. In practice objects have a specific staining pattern, and the limit is only obtained when all pixels covering the cell are uniformly illuminated and are all saturated.

For example, a cell of 10 micron covers  $\sim 2000$  pixels. This results in a dynamic range of approximately 1:  $6.5 \times 10^4$  and corresponds with 4 logs of dynamic range. In general a system with a higher magnification has a larger dynamic range. This increase of the dynamic range can be used to lower the detection limit. In the CellTracks TDI system one can increase the intensity of the excitation light to increase the total signal output and use the full dynamic range.

It should be noted that in this description of the detection limit and dynamic range  $\sigma_p$  is considered to be constant, which is appropriate when comparing 1 system and measuring cells with a different size. When comparing 2 systems, with different magnifications,  $\sigma_p$  is not constant. The total background contribution  $S_{BG}$  for a single object is approximately the same for both systems and only pixel dependent noise ( $\sigma_{DARK}$  and  $\sigma_R$ ) increases with the square root of  $N$ . Furthermore increasing excitation light also has a disadvantage: the background noise will increase approximately linear with the excitation and  $S_{SIGNAL}$  is limited by the maximum amount of photons emitted by a fluorophore. Besides this, other factors also play a role when comparing two systems. The detection efficiency  $\eta_{eff}$  will be different, as the NA of the microscope objective is usually smaller for low magnifications.

The SNR of a cell can be calculated using eq. 2.35. (All variables are measured in electrons). This will yield an average of the SNR for an object since each pixel has a different signal and a different noise level. Therefore the SNR given for a single cell is an estimate for the total signal ( $S_{SIGNAL}$ ) from the  $N$  pixels that cover a cell. As shown the SNR drops when more pixels are used.

$$SNR = \frac{S_{SIGNAL}}{\sqrt{S_{SIGNAL} + N \cdot \sigma_p^2}} \quad (2.35)$$

$$S_{SIGNAL} = S_{TOTAL} - S_{BG} - S_{DARK} - S_{BIAS}$$

For each cell, the total signal output  $S_{TOTAL}$  is measured and the contributions of the (mean value of the) background, dark current and bias should therefore be subtracted to obtain  $S_{SIGNAL}$ .

### 2.3.3 Theory: Fluorescence emission

Figure 2.3.1a shows the Jablonski energy diagram for a typical fluorophore. In order to simulate the fluorescence emission process, a simplified model<sup>97-100</sup> (Figure 2.3.1b) will be used with only 2 electronic levels and no higher excited states. For our situation this is justified, as we typically use irradiance levels which are a factor of 500-2000 lower than needed to reach half saturation level of the fluorophores. Higher order transitions will therefore hardly ever occur in practice. The singlet state  $S_1$  is then almost empty and the long living triplet state,  $T_1$  has a very low occupancy as for the rate constants of the transitions holds  $K_{ISC} \ll K_F$  and  $K_{NR}$ . Photo bleaching is assumed to occur from the  $S_1$  state with a rate constant  $K_{BL}$ . It is assumed that bleached molecules no longer participate in the excitation-emission cycles.

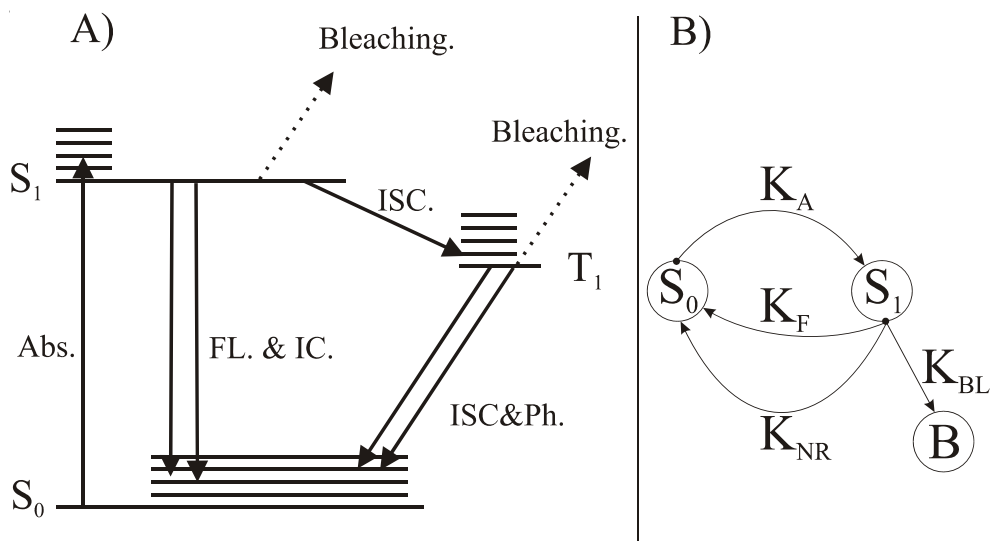


**Figure 2.3.1** A) Jablonski energy level diagram for a fluorophore.  $S_0$ ,  $S_1$ ,  $T_1$  are the energy levels of the ground state, first excited singlet state and the triplet state, respectively. The arrows represent the transition between the states. Abs.: absorption; FL.: Fluorescence; IC.: internal conversion, ISC.: intersystem crossing; Ph.: Phosphorescence. The dotted lines represent photo bleaching. B) Simplified model of the fluorescent process used for calculations.  $K_F$ ,  $K_{NR}$ ,  $K_{BL}$  and  $K_A$  are the rate constants for respectively depopulation of  $S_1$  by fluorescence emission, non radiative conversion, bleaching and depopulation of  $S_0$  by absorption. Bleached fluorophores do not longer participate in the excitation emission cycle.

The excitation rate constant  $K_A$  from state  $S_0$  to state  $S_1$  is proportional to the laser irradiance  $I$  [ $\text{W}/\text{cm}^2$ ] and to the absorption cross section  $\sigma_{S_0S_1}$  [ $\text{cm}^2$ ] at a wavelength  $\lambda$  (Eq. 2.36). The absorption cross-section of the fluorophores we use is wavelength dependent. We therefore first calculate an average absorption cross-section by multiplying the excitation band profile with the (normalized) absorption band.

$$K_A = \frac{I}{E_{\text{photon}}} \sigma_{S_0S_1} \quad [\text{sec}^{-1}] \quad (2.36)$$

Where,

$E_{\text{photon}} = \frac{\hbar c}{\lambda}$  is the energy of a single photon ( $\hbar$  = Planck constant =  $6.63 \times 10^{-34}$  Js,

$c$  = velocity of light =  $3 \times 10^8$  m/s).

$K_1$  is defined as the total rate constant for depopulation of  $S_1$ , the lifetime  $\tau_1$  of the  $S_1$  state is given by eq. 2.37

$$K_1 = K_F + K_{NR} + K_{BL}$$

$$\tau_1 = \frac{1}{K_1} \quad (2.37)$$

The fluorescence quantum yield is defined as the ratio between the number of fluorescent transitions and all transitions from level  $S_1$ .

$$\Phi_F = \frac{K_F}{K_1} = \frac{\tau_1}{\tau_F} \quad (2.38)$$

The bleaching quantum yield can be defined as the portion of bleached transitions compared to all transitions from level  $S_1$ .

$$\Phi_{BL} = \frac{K_{BL}}{K_1} \quad (2.39)$$

The maximum number of photons,  $n_f$ , that a single fluorophore can emit before it is bleached, is given by eq. 2.40

$$n_f = \frac{\Phi_F}{\Phi_{BL}} \quad (2.40)$$

### ***Kinetic behavior***

The kinetics of excitation and emission follows from coupled first-order differential equations. The probabilities of the  $S_0$  and  $S_1$  states are time dependent and follow from (eq 2.41). In the absence of light a fluorescent molecule is assumed to be in the ground state  $S_0$ .

$$\begin{aligned}\frac{dS_0(t)}{dt} &= -K_A \cdot S_0 + K_F \cdot S_1 + K_{NR} \cdot S_1 \\ \frac{dS_1(t)}{dt} &= +K_A \cdot S_0 - K_1 \cdot S_1 \\ \frac{dB(t)}{dt} &= +K_{BL} \cdot S_1 \\ S_0(0) &= 1 \quad S_1(0) = 0 \quad B(0) = 0 \\ S_0(t) + S_1(t) + B_1(t) &= 1\end{aligned}\tag{2.41}$$

The solution for the time dependent  $S_1(t)$  probability is given in eq. 2.42. The equation contains the steady state condition  $S_{1eq}$ . Between parentheses the time dependent parameters are given, with one term for the irreversibly photo-bleached molecule and a term concerning the initial start condition. The last time dependent term (initial start condition) can be neglected for total signal output calculations. The steady state conditions  $S_{1eq}$  under constant illumination are achieved after illuminating for a period in the order of the fluorescent lifetime  $\tau_F$ .

$$\begin{aligned}S_1(t) &= \frac{K_A}{K_A + K_1} \cdot \left( e^{\left(\frac{-K_A K_{BL}}{K_A + K_1}\right) \cdot t} - e^{-(K_A K_0) \cdot t} \right) \\ &\approx S_{1eq} \cdot e^{\left(\frac{-K_A K_{BL}}{K_A + K_1}\right) \cdot t} \\ S_{1eq} &= \frac{K_A}{K_A + K_1}\end{aligned}\tag{2.42}$$

The rate constant of photo bleaching is usually much smaller than other rate constants,  $K_{BL} \ll K_F$ .

### ***Fluorescence signal***

To properly describe the fluorescence signal emitted by a dye solution after excitation with a focused laser beam, one has to know the intensity distribution in the laser focus. To obtain a solution, the laser focus is approximated by a rectangular, time independent, excitation profile. The probability that a dye

molecule is in the excited state  $S_I$  under constant excitation is  $S_I(t)$ . All fluorescent transitions occur from the  $S_I$  state with a rate constant  $K_F$ . The total fluorescence emission rate  $N_{rate}(t)$  for  $C_F(0)$  fluorophores is therefore given by eq. 2.43

$$N_{rate}(t) = C_F(0) \cdot K_F \cdot S_I(t) = C_F(0) \cdot \Phi_F \cdot \frac{K_A}{\frac{K_A}{K_1} + 1} \cdot e^{\left(-\frac{K_A}{\frac{K_A}{K_1} + 1} \cdot \Phi_{BL}\right) \cdot t} \quad (2.43)$$

$$N_{rate}(t) \approx C_F(0) \cdot \Phi_F \cdot K_A \cdot e^{(-K_A \cdot \Phi_{BL}) \cdot t}$$

For low light conditions far below saturation  $K_A \ll K_1$  and

$$\frac{K_A}{\frac{K_A}{K_1} + 1} \approx K_A$$

The total number  $N_S(T)$  of photons emitted for  $C_F(0)$  fluorophores during a time period 0 till T is given by eq. 2.44.

$$\begin{aligned} N_S(T) &= \int_0^T N_{rate}(t) \cdot dt \\ &= C_F(0) \cdot \frac{\Phi_F}{\Phi_{BL}} \cdot \left(1 - e^{\left(-\frac{K_A}{\frac{K_A}{K_1} + 1} \cdot \Phi_{BL} \cdot T\right)}\right) \approx C_F(0) \cdot \frac{\Phi_F}{\Phi_{BL}} \cdot \left(1 - e^{(-K_A \cdot \Phi_{BL} \cdot T)}\right) \end{aligned} \quad (2.44)$$

This simplified model shows that the fluorescence emitted by a fluorophore decays exponentially with a decay time of  $\tau_{BL} = 1/(K_A \cdot \Phi_{BL})$ .

The maximum signal that ultimately can be achieved is reached when all fluorophores are bleached, independent of the excitation power. The total fluorescent signal observed in a time period, is ultimately determined by the bleaching rate and the lifetime of the fluorophore. The model shows that at low intensities the fluorescent emission is approximately linear with the excitation power ( $K_A \ll K_1$ ). For high excitation powers ( $K_A \cong K_1$ ), the fluorescent signal (rate) is limited by the lifetime of the fluorophore. This means that high excitation rates, reaching the saturation energy of the fluorophore during integration of the signal by the CCD, are less efficient. For flowcytometry<sup>28</sup> intensities are used ranging from 1 to 400 kW.cm<sup>-2</sup>, these are at least a factor of 1000 higher than is commonly



used in image cytometry. Fluorophores like PE and APC have saturation energies of 18 and 65 kW.cm<sup>-2</sup> respectively and can therefore be saturated in a flow cytometer. Fluorophores like the 655 quantum dots have a long lifetime of ~20-40 ns<sup>101</sup> and saturation energies of ~1000 W.cm<sup>-2</sup>. Quantum dots are therefore limited in the maximum emission rate despite the high absorption cross-section of these fluorophores. The bleaching rate of these molecules is very low and excitation and emission spectra are far apart. This makes them from a technical point of view ideal for image cytometry which uses relatively low excitation intensities and long illumination times.

### Typical values

R-Phycoerythrin and Allophycocyanin are two important fluorophores used in the CTC detection assay. The relatively large absorption cross-section with a short fluorescence lifetime results in a quick burst of photons with a relatively high throughput. This is an important aspect to obtain a high SNR whereas the signal increases much faster during the illumination than the noise does.

	$\lambda_{\text{abs}}$ (nm)	$\lambda_{\text{fl}}$ (nm)	$\sigma$ (peak) cm <sup>2</sup> /molecul e	$\tau_{\text{FL}}$ (ns)	$\tau_0$ (ns)	$\Phi_{\text{FL}}$	$\Phi_{\text{BL}}$	$n_f$ (photons/ molecule)
APC	650	660	$2.67 \times 10^{-15}$	2.7	1.8	0.68	$4.5 \times 10^{-6}$	$1.5 \times 10^5$
R PE	546	578	$7.48 \times 10^{-15}$	3.2	3.1	0.98	$1.1 \times 10^{-5}$	$8.9 \times 10^4$
DAPI	347	458	$9.02 \times 10^{-17}$	2.8		0.90	-	-

**Table 2.3.1** Fluorescent properties of R-Phycoerythrin and Allophycocyanin<sup>56,57</sup> and DAPI<sup>102</sup> bound to DNA.

### 2.3.4 Signal throughput

For the CTC detection assay 3 fluorophores are used, DAPI, PE, and APC. The detection efficiency of the CellTracks TDI varies for these dyes and depends on the detection efficiency of the setup as given in chapter 2.1.2, and the used emission filter for each fluorophore. In figure 2.3.2 the normalized emission spectra are shown (solid lines) and the dashed lines are the remaining spectra of the fluorophores when passed through the optical system. The total detection efficiency of each fluorophore is determined by the ratio of the area underneath the filtered spectra divided by the area of the initial emission spectra of the fluorophore. Effectively less than 1% of each photon emitted by a fluorophore is successfully converted to a photoelectron detected by the camera.

Channel	Excitation	Absorption efficiency at excitation.	Emission peak	Emission Filter	Total detection efficiency
	$\lambda(\text{nm})$	(%)	$\lambda(\text{nm})$		%
DAPI	375	80	458	450DF65	0.44
PE	532	79	578	580DF30	0.77
APC	639	77	660	660DF32	0.68

**Table 2.3.2** Detection and excitation efficiency of the CellTracks TDI system when using specific emission filters for DAPI, PE and APC.

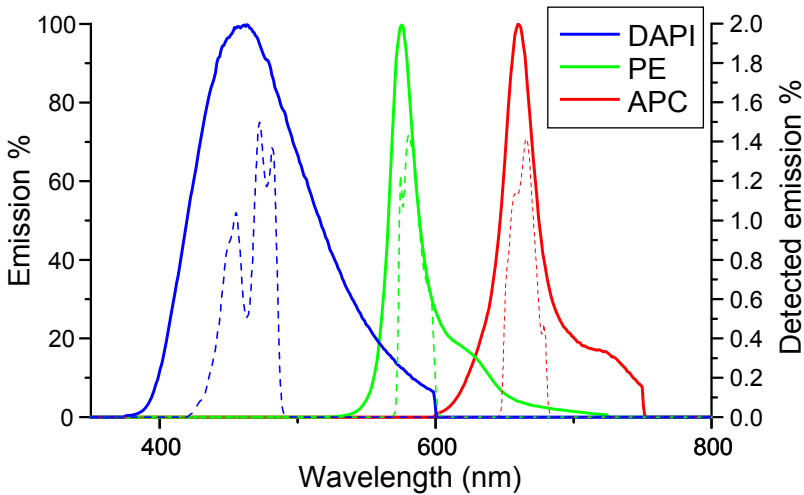


**Figure 2.3.2** Emission spectra for DAPI, PE and APC (solid lines) and the corresponding emission spectra of these dyes when filtered through the optical system (dashed line, with the corresponding Y-axis at the right side of the graph).

### 2.3.5 Measurements: Noise

#### *Noise factors for CTC samples*

The total noise introduced in a measurement depends strongly on the sample and on the specific fluorophore which is measured. Variations are caused due to variations of the background signal  $\mu_{BG}$ . The total noise of a single pixel is given by:

$$\sigma_P = \sqrt{\mu_{BG} + \mu_{DARK} + \sigma_R^2} \quad (2.46)$$

The pixel noise of a specific sample/image is calculated from two measured images<sup>77</sup>  $I_1$  and  $I_2$ . The two images have the same expectation but different realizations of the noise. The noise per pixel  $\sigma_p$  in (DN) is therefore given by:

$$\sigma_p = \frac{\sigma[I_1 - I_2]}{\sqrt{2}} \quad (2.47)$$

To get insight in the introduced noise for CTC samples we measured the noise contribution for the DAPI, PE and APC channels (table 2.3.2.). A 375, 532 and a 639 nm laser are used for excitation with the following band pass filters: 450DF40, 580DF30 and 660DF32 respectively. Furthermore the samples are scanned in TDI mode at a scan speed of 1 mm/s. These are the conditions normally used for the CTC samples in the CellTracks TDI. Besides a CTC sample, we also tested a clean PBS solution. The noise level per pixel  $\sigma_p$  is calculated according to eq. 2.47 at positions without a fluorescent object. As shown in table 2.3.3 typically the noise at dark is  $\sim 1.88$  DN, this equal to  $8.6 e^-$ , and corresponds with the readout noise according to camera specifications.

Channel	PBS	CTC-SAMPLE
	$\sigma_p$ (DN)	$\sigma_p$ (DN)
Average at dark	1.88	1.88
DAPI channel (10%)	3.60	8.21
PE channel	2.75	2.70
APC channel	2.57	2.80

**Table 2.3.3** Average noise levels for the CellTracks TDI when measuring a PBS and a CTC-sample using DAPI, PE and APC emission filter.

Channel	Excitation	Emission Peak	Emission Filter	Raman Peak for water	$\sigma$ (peak)
	$\lambda$ (nm)	$\lambda$ (nm)		$\lambda$ (nm)	$\text{cm}^2/\text{molecule}$
DAPI	375	458	450DF65	430	$3.03 \times 10^{-29}$
PE	532	578	580DF30	649	$5.48 \times 10^{-30}$
APC	639	660	660DF32	816	$2.13 \times 10^{-30}$

**Table 2.3.4.** Absorption cross section and emission of water due to Raman scattering of water at 365,532 and 639 nm excitation.<sup>103</sup>

When the laser excitation is turned on the background noise is increased. Typically the noise level increases to  $\sim 2.7$  DN for the APC and PE channels for both samples. This indicates that the CTC-sample contains a low level of free fluorophores in the solution and is properly washed. The increase of background noise can be assigned to stray light originating due to reflections and scattering of

the sample at lenses and filters of the optical system. Background noise due to Raman scattering can be neglected for the APC and PE channel. If Raman scattering occurs it is most likely due to the bulk amount of buffer solution. Typically the Raman cross-section<sup>103</sup> is very small and the peak of the Raman shift for water is  $\sim 3400 \text{ cm}^{-1}$ . As shown in table 2.3.4 Raman scattering is blocked when measuring the APC and PE fluorophores.

However for the 375 nm excitation, in case of the DAPI channel one might expect some additional background due to Raman. Besides stray light some additional background is also induced due to auto fluorescence and due to specific and non-specific labeling of small cellular debris. As shown in table 2.3.2 is the background noise for the DAPI channel much higher for the CTC-sample. This increase in noise to  $\sim 8 \text{ DN}$  is induced by the excessive amount of free ferrofluid particles. The ferrofluid is partly blocking the background. In a homogeneous condition the noise increases with the square root of the background signal. However the background signal is not homogeneous and noise depends on the modulation of the actual background induced by the ferrofluid.

### *Noise and images*

This is also clear from figure 2.3.3. It shows a fluorescent image of the cytokeratin (PE), the nuclear staining (DAPI) and a brightfield image of an apoptotic CTC and a leukocyte.

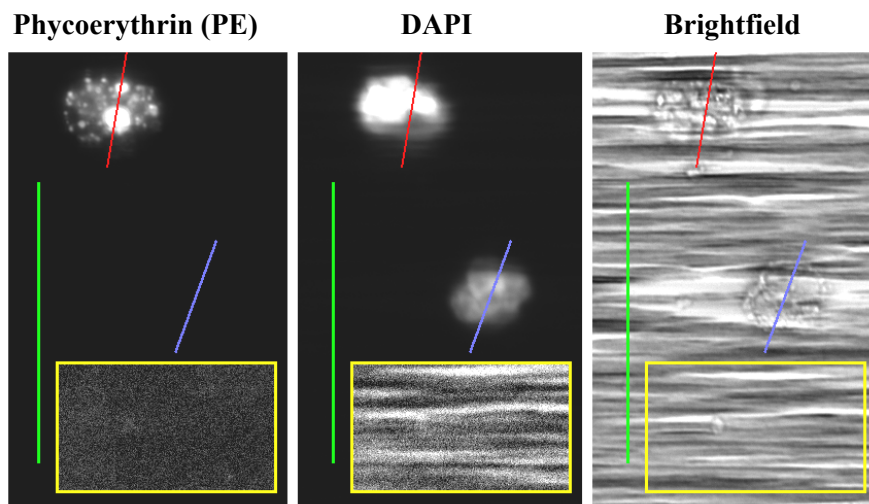


**Figure 2.3.3** Fluorescent images of an apoptotic CTC and a leukocyte. Cytokeratin (PE), nuclear staining (DAPI) and brightfield image are shown respectively. The indicated lines red, green and blue are associated with the line profiles shown in figure 2.3.4. The yellow box shown is contrast enhanced (Range 0-30) to show typical background variations.

The associated line profiles in this image are shown in figure 2.3.4. Furthermore a specific part of the image is contrast enhanced (range 0-30 DN) indicated with a yellow box. This directly reveals the influence of the ferrofluid on background noise. Typically the fluctuations of the DAPI background are similar with the striped ferrofluid distribution visible in the bright field image.

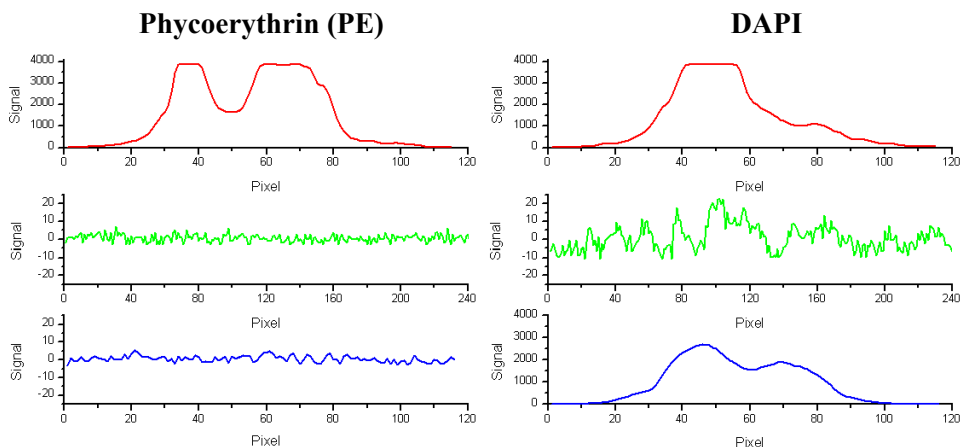


**Figure 2.3.4** Line profiles of the red green and blue line shown in figure 2.3.3 for PE and DAPI.

The images shown in figure 2.3.3 and the associated line profiles directly indicate some of the troubles that arise when analyzing the samples. As shown the dynamic range is limited by the maximum peak signal of the event. The peaks in the cytokeatin and the DAPI image are already saturated and limit accurate quantification of the fluorophores and reduces image contrast. This can only be prevented by signal reduction. (Decrease excitation and/or integration time)

It is also apparent from these images that the ferrofluid interferes with the fluorescent signal. Some parts of the fluorescent images are partly blocked. As a consequence this will introduce errors in the quantification and underestimate the total signal. Furthermore image detail is partly lost and is therefore less accurate for image details describing the specific staining pattern of the cell. The influence of the ferrofluid on the brightfield image is also apparent; the high contrast of the ferrofluid lines makes the brightfield image rather difficult to analyze. Brightfield signals could be used as good parameter to describe the cell morphology and could be used as a kind of mask/area to measure the signal of the fluorescent images. However with the current amount of free ferrofluid this is rather difficult. Therefore it would be very valuable to reduce ferrofluid content which will result in less noise and an increase of signal and accuracy.

## 2.3.6 Measurements: Bleaching and SNR

### *Bleaching*

Bleaching of the fluorophores is the limiting factor for the detection of fluorescent labels. After some period most the fluorophores are bleached and increasing irradiance or integration time does not result in signal increase and results in a decrease of SNR. The bleaching rates of the used fluorophores for the CellTracks TDI were measured using whole blood samples spiked with SKBR-3 cells. The SKBR-3 cells are labeled with PE-cytokeratin and the leukocytes are labeled with APC-CD45. The nuclei are stained with DAPI. To obtain decay curves for these fluorophores, selected cells were repeatedly scanned at a speed of 1 mm/s. The obtained decay curves are shown in figure 2.3.5 and follow a first order exponential decay according to eq. 2.43 where  $\tau_{BL} \approx I/(K_A \Phi_{BL})$ . Apparent from these curves is the relatively short decay time ( $\tau_{BL}$ ) for the PE fluorophore of  $\sim 3$  seconds. When excitation intensity is reduced with a ND4 filter the decay time is  $\sim 4x$  times larger and it indicates that photo bleaching is linear increasing with the excitation power.

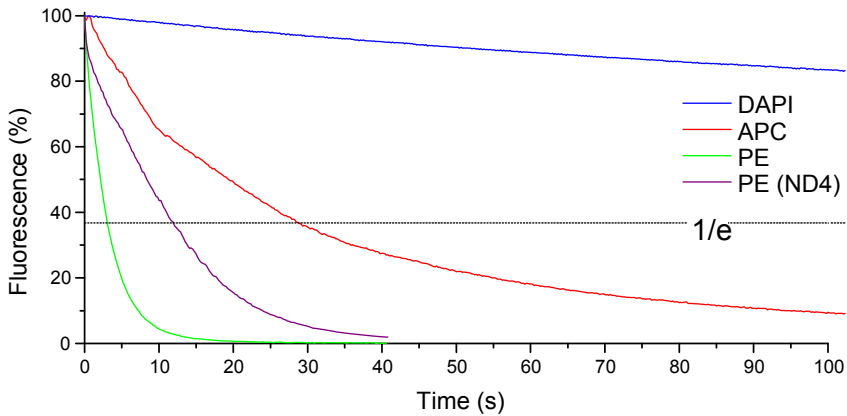


**Figure 2.3.5** Bleaching rates of DAPI, APC, PE and PE(ND4) in the CellTracks TDI setup. Decay curves are measured at a scan speed of 1mm/s. The intersection of the decay curves with the 1/e line corresponds with the decay time  $\tau_{BL}$ .

### Signal to noise ratio (SNR)

The total signal collection, decay and the SNR for PE are shown in figure 2.3.6. All curves are normalized to 100%.

The black curve in figure 2.3.6 shows the total amount of PE signal (%) during acquisition. The signal is increasing until all fluorophores are bleached (eq. 2.44). However the maximum signal to noise ratio is obtained before all fluorophores are bleached. The two curves shown for the SNR are calculated according to eq. 2.35. The red curve shown is the SNR measured for a large SKBR-3 cell ( $\sim 240\mu\text{m}^2$ ) with an average intensity of 700 DN/pixel; this is at the initial condition. (First frame ( $\sim 204.8$  ms)). It shows that the SNR is increasing until a total integration time of  $\sim 10$  seconds. For smaller and/or brighter objects the absolute SNR and optimal integration time will increase. For larger and/or dimmer objects the absolute SNR and optimal integration time will decrease. The blue line in figure 2.3.6 indicates this limiting case of the SNR. This situation occurs for dim signals and/or a high background when the absolute SNR drops below 1. The maximum SNR for dim signals is obtained when the integration time ( $T_{\text{int}}$ ) is approximately equal to the bleaching rate  $\tau_{\text{BL}}$ .

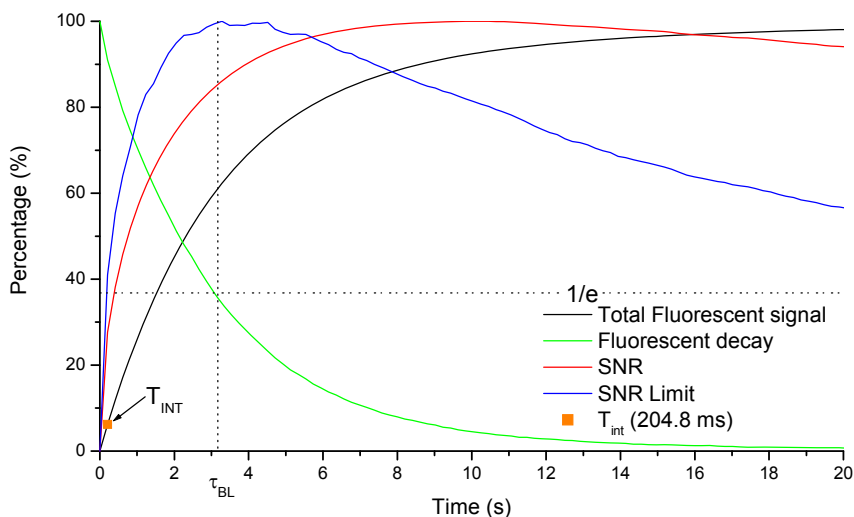


**Figure 2.3.6** Relative signal output for PE with a decay time of  $\tau_{\text{BL}}$ . The green line indicates the exponential decay curve and the black line shows the total signal. The orange dot indicates the integration time  $T_{\text{int}}$  at 1mm/s ( $\sim 204.8$  ms). The red and blue line indicates the SNR for a typical object (average signal), and noise limited object respectively.

The decay curves of figure 2.3.5 shows that for all fluorophores only a small portion is bleached. The used integration time  $T_{\text{int}}$  is much smaller than  $\tau_{\text{BL}}$  and to

obtain the maximum SNR it would require an increase of excitation power and/or integration time.

However increasing excitation power or integration time for the initial scan is not useful for PE and DAPI. This would result in excessive saturation of the camera for most objects and an increase of signal is only useful for dim objects. For the CTC samples analyzed with the CellTracks TDI only an increase of excitation power of the red laser is still useful; whereas the APC signal is relatively dim compared to PE and DAPI and does not fill the complete dynamic range for these samples. Another reason to spare the fluorophores on the objects is to retain the possibility to reexamine specific events. This gives the possibility to further investigate objects and to increase integration time to obtain the maximum SNR for dim events.

### 2.3.7 Measurements: Sensitivity, linearity and dynamic range

#### *Sensitivity and dynamic range*

The fluorescence sensitivity<sup>104</sup> of the CellTracks TDI for PE was measured using Quantibrite PE beads (Becton Dickinson, NY, USA). These are calibrated standardized Phycoerythrin (PE) conjugated 3.65 micron beads with a known amount of PE molecules per bead. Each vial contains 4 bead populations with 515, 5956, 26653 and 69045 PE molecules. The beads were deposited on a glass slide and diluted in PBS. Accordingly two samples were scanned at a scan speed of 1mm/s and 0.4 mm/s. At this speed each object was illuminated and integrated for ~204.8 ms and 512 ms respectively. The excitation for these beads was the 532nm laser excitation line and a 580DF30 emission filter was used. The obtained histograms are shown in figure 2.3.7. In these histograms the mean signal value/pixel is plotted in digital numbers (DN). This value was calculated from the signal ( $S_{\text{SIGNAL}} = S_{\text{TOTAL}} - S_{\text{BG}} - S_{\text{DARK}} - S_{\text{Bias}}$ ) of the object divided by the area of the bead (~1050 pixels). It appears that all four bead populations are resolved from the background. The coefficient of variation (CV) is approximately 12%-15% for the 2 highest peaks and is primarily determined by a variation of the amount of PE molecules/bead. Comparable measurements with a flow cytometer show variations of the same order~13%. The relatively low CV of 7.2% for the highest peak in figure 2.3.7b when scanning at 0.4 mm/s is not realistic. For these beads integration is too long and the signal output is saturated for some pixels and clipping to the maximum value of the camera. The mean value and variation of the signal is therefore underestimated.



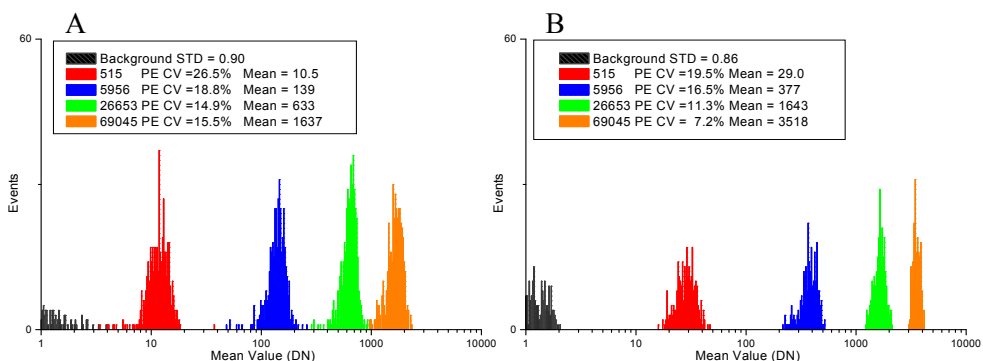


**Figure 2.3.7** Histograms with the mean signal value/pixel for 4 Quantibrite PE bead populations and the background signal for an average area of 1050 pixels per object. Histograms A and B are at a scan speed of 1.0 and 0.4 mm/s respectively.

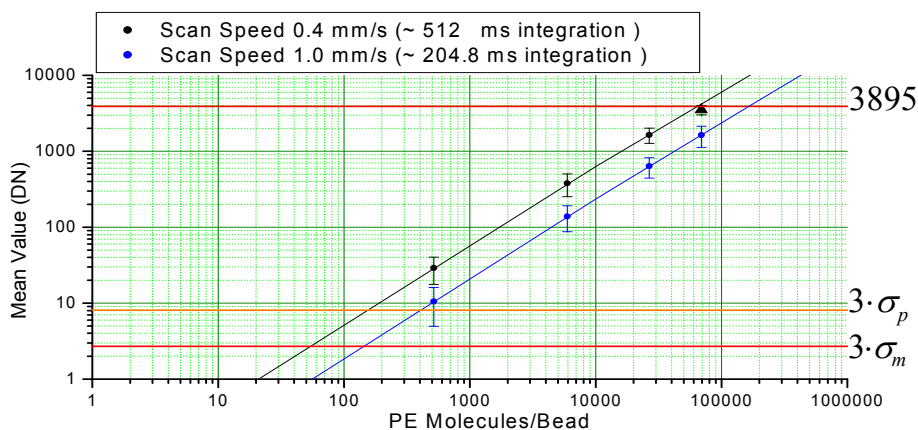


**Figure 2.3.8** Mean Fluorescence intensity of the Quantibrite calibration beads plotted against the PE molecule density per bead. The error bars indicate the  $\pm$  standard deviation of the mean signal value. The red line at 3895 indicates the maximum signal/pixel. The under limit of signal detection is indicated by the two lines at the bottom of the graph. In the graph  $\sigma_p$  is the total noise of a single pixel and  $\sigma_m$  is the measured noise level which is averaged over an area of 1050 pixels. The sensitivity is determined by the total amount of photons detected for a bead divided by the number of PE molecules/bead. At 1mm/s and 0.4 mm/s 115 photons and 295 photons are detected respectively for a single PE molecule. The red line at 3895 is indicating the maximum signal value of the camera (DN) minus the bias  $\sim$ 200 DN. The beads with the highest peak (triangle) at 0.4 mm/s are partly saturated and therefore omitted in calculating the interpolated (black) line.

The mean value of each bead population shown in the histograms of figure 2.3.7 has been plotted against the known PE molecule density of the beads. As shown in figure 2.3.8 signal increase is linear with the total amount of PE molecules/bead.

The under limits of detection are given by the position where 3 times  $\sigma_p$  coincides with the interpolated lines. The detection limit is therefore  $\sim 150$  and  $\sim 400$  PE molecules for a scan speed of 0.4 and 1.0 mm/s respectively. This determination is based on a simple threshold algorithm to segment and detect an object. As is already apparent from the error bars for the lowest peak at 1mm/s, some pixels of the object are below the noise level. However for this measurement we used a brightfield image to detect the position of the beads. This image was used as a mask to measure the total signal of an object. The detection limit is therefore  $\sim 60$  and  $\sim 150$  PE molecules for a scan speed of 0.4 and 1.0 mm/s respectively. The detection limit therefore depends on the used segmentation algorithm. To clarify this further an image of a dim Quantibrite bead is shown in figure 2.3.9. The area/mask of the image is determined with different segmentation methods.

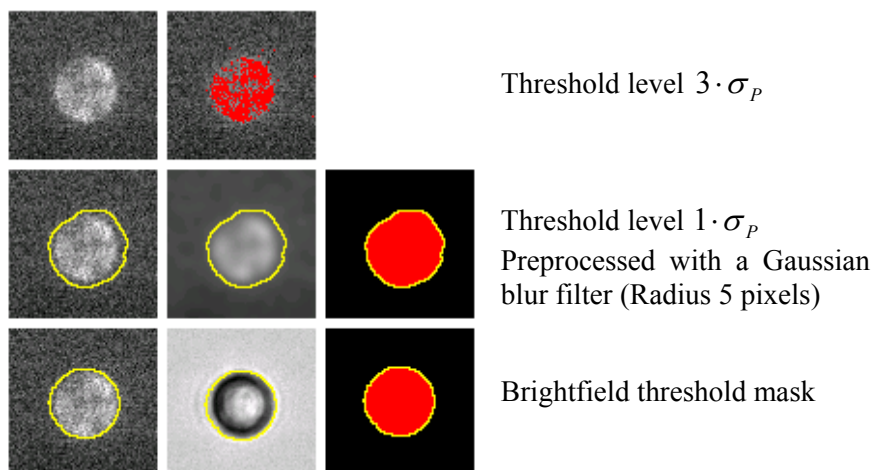


**Figure 2.3.9** Dim Quantibrite-PE bead with on average 515 PE molecules. A simple threshold segmentation algorithm is limiting the detection limit. Averaging neighboring pixels or the use of a brightfield mask can further lower this detection limit.

As shown when the threshold level is set to 3 time  $\sigma_p$  some pixels in the background are already above threshold level and some pixels within the bead are below threshold. This can be prevented by using a Gaussian blur filter. This filter averages the pixel intensity within a specified radius for each pixel. Although this smoothing reduces resolution it averages down the noise and enables us to segment the particles at a lower threshold limit to obtain a proper mask for the object.

When a brightfield image is used as a mask/trigger for the detection area the detection limit doesn't depend on the fluorescent signal. This enables detection of an event without a fluorescent signal and accumulation of the signal is done for a well defined area of the mask which is a direct measure of object size.

### ***Linearity and system variation***

The coefficient of variation (CV) is an important aspect for an image cytometer as it determines how well closely spaced populations can be separated. The measured CV for a population is determined by the variation of the object and variations introduced by the optical system. Typically inhomogeneous illumination is the main factor that introduces additional variations of the measurement. In the CellTracks TDI a homogeneous profile is created with a beam homogenizer as described in chapter 2.1 Furthermore a correction is applied based on the measured illumination profile to obtain a homogeneous output for the complete illumination area. Although this correction is possible and useful, the initial illumination profile should be as uniform as possible whereas signal correction also amplifies the noise of the system.

The linearity and the variation of the CellTracks TDI were measured with Rainbow linear particle, RLP-30-5 (Spherotech Inc., Libertyville, IL, USA). The sample contains a mixture of blank particles and rainbow particles in five different fluorescent intensities. The intensity drops down in divisions of 2 from the brightest particle. The size of these particles ranges from 3.0 to 3.4 micron and they have a small coefficient of variation ~2.0%. This small coefficient of variation (CV) makes them useful to determine variations introduced by the measurement system, whereas the CV depends less on the particle variation.

The coefficient of variation is defined as:

$$CV = \frac{STD}{Mean} \cdot 100\% = \frac{\sigma}{\mu} \cdot 100\% \quad (2.48)$$

The rainbow beads were prepared on a glass slide and diluted in PBS. Next the sample was scanned at a scan speed of 1mm/s. As excitation source we used the 532 nm green laser which has been partly blocked with a ND4 filter to prevent saturation of the brightest peak. At this speed and intensity each object is illuminated and integrated for ~204.8 ms and the maximum peak has a mean value of ~ 1200 DN which is at ~1/3 of the full camera range. The obtained histogram is shown in figure 2.3.10.

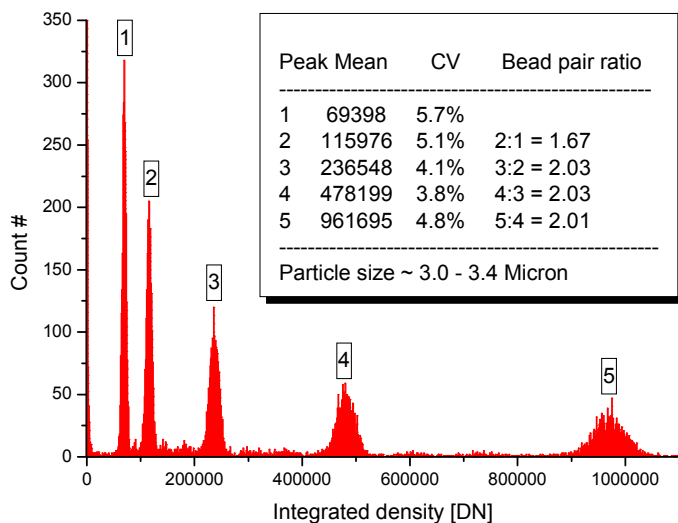


**Figure 2.3.10** Histogram of the integrated density for Rainbow RLP-30 beads, The resulting CVs are ~4.7% as shown. The ratio between the consecutive bead populations is 2.

The CVs obtained are on the average 4.7% with a minimum of 3.8% for peak 4 and a maximum for peak 1 of 5.7%. The system also has a linear response, whereas the ratio between the bead populations is approximately ~2.0 as specified, and a linear regression through the plot values results in a  $R^2 = 0.9998$ . This excellent linear behavior can be expected for a CCD detection system.

## 2.3.8 Optimal scan speed and acquisition times

### *Optimal scan speed*

The maximum scan speed of the CellTracks TDI is determined by the maximum stable readout rate at 5 KHz of the TDI camera. This is obtained at a scan speed of 1mm/s and corresponds with an integration time of 204.8 ms.

When images are acquired for a CTC sample, the complete surface of a sample chamber is scanned. The surface area of these sample chambers is 2.7 x 29.7 mm. To obtain the fastest scan of the complete chamber the maximum scan speed of 1mm/s is used for all fluorophores. However, this is only possible if the fluorescent emission is high enough and furthermore it is limited by the dynamic range of the camera. With this in mind optimal conditions for signal acquisition are obtained when approximately the mean value of the signal is at 2/3 of the full camera range to prevent saturation. This could be obtained by reducing the scan speed but it would also result in a reduction of the overall scan time of the sample. A better

approach would be an increase of signal by increasing the amount of excitation light. Therefore the CellTracks TDI system is equipped with multiple lasers instead of a mercury arc lamp. The amount of irradiance that can be obtained with a laser is much higher and is easily controlled. Furthermore as shown in chapter 2.3.6 are the decay times ( $\tau_{BL}$ ) of the fluorophores much longer than the integration time of 204.8 ms with the current excitation power. Therefore it is not limited by bleaching and increasing excitation power or acquisition time is still useful. This makes it possible to scan the fluorescent objects at  $\sim 2/3$  of the dynamic range of the camera without sacrificing scan speed. A further increase of scan speed for this system is straightforward and only requires a faster camera and a corresponding increase of laser excitation power.

### ***Acquisition time***

As already mentioned in the introduction the acquisition time for a low resolution system is shorter than for a high resolution system. This is also in general the main reason to use a low magnification system instead of a high resolution system. However a faster scan speed comes at the cost of lower resolution and reduces the specificity regarding morphological parameters.

As will be shown in the next paragraph an increase in resolution is desired when analyzing CTC samples. This higher degree of specificity can be obtained with our CellTracks TDI setup and not with the current “CellTracks Analyzer II” (Immunicon Inc, Huntingdon Valley, USA). To prevent excessive scanning times due to an increase in resolution, the CellTracks TDI has been optimized to minimize the total acquisition time. To illustrate these points, I will give a comparison of the actual acquisition times of these two systems and an estimate for a 32.25x system without a TDI CCD.

The field of view is decreased with the square of the magnification ( $M^2$ ). The number of images needed to cover a complete chamber increases therefore dramatically when a smaller sampling distance is used. This would yield an increase of acquisition time with a factor 10.4 for the CellTracks TDI. The total acquisition time for a system can be estimated by the acquisition time of a single frame multiplied by the total number of frames ( $N_{FRAME}$ ) covering the complete surface area. The total acquisition time of a single frame ( $T_{FRAME}$ ) is described by:

$$T_{frame} = \sum_{i=1}^K T_{OVERHEAD(i)} + T_{CHANNEL(i)} \quad (2.48)$$

$$T_{TOTAL} = T_{frame} \cdot N_{FRAMES}$$

Where  $T_{OVERHEAD(i)}$  is the overhead time which is introduced due to readout of the camera, switching of the bandpass filter, and relocation to the next frame.

$T_{\text{CHANNEL}(i)}$  is the integration time needed for each (fluorescence or brightfield) image. In total  $K=4$  channels are imaged (DAPI, PE, APC and FITC or brightfield). The integration times used are the actual values needed for the analysis of a CTC sample. The results of the comparison are shown in table 2.3.5. Typically a complete scan with the CellTracks Analyzer II takes about 9 minutes and with the CellTracks TDI this is 38 minutes. Although acquisition time is increased for the CellTracks TDI it is much faster than a traditional system, that operates at a sampling distance of 0.2 micron/pixel, without a TDI-CCD camera. Such a system would need at least 80 minutes. (Assuming that the required integration time is equal with the CellTracks Analyzer II). However for these systems integration time is not the limiting factor. Typically the CellTracks Analyzer II needs on average 0.48 seconds overhead time for each image. The overhead time in these systems contributes 63% of the total acquisition time, as shown (marked green) in table 2.3.5. Reducing this overhead time therefore makes a great step towards reducing the total acquisition time.

### ***Reducing overhead time***

Overhead time is the main reason why the CellTracks TDI uses a TDI camera. The use of a TDI minimizes overhead time due to stage repositioning. The overhead time is thereby reduced to 16% of the total acquisition time. Therefore, it results in a shorter scan time yet using the same integration time. The CellTracks TDI acquires image data continuously during movement and obtains 1 large image of 0.180 x 30 mm (135 Mpixel). This process is repeated 16 times to cover the complete chamber for 1 channel. The acquisition of such a long image takes 30 seconds. During the acquisition each object is effectively integrated and illuminated for 204.8ms. An additional overhead time of ~ 5 seconds/image is introduced when the stage is repositioned to the next line and is brought into a continuous motion again.

### ***Reducing acquisition time***

As mentioned, the acquisition speed of the CellTracks TDI is currently limited by the maximum scan speed of 1mm/s.

However it is now also limited by the size of the excitation profile. At present only 67% (900 pixels) of the camera width is used. Extending the illumination profile to the full width of the camera (1344 pixels) could reduce the amount of frames needed in the horizontal direction. This would reduce the total amount of 16 lines to 11 lines and bring acquisition times down to ~26 minutes. The main reason to use this smaller illumination profile is the possibility to reduce scanning times further with a PDMS groove structure (See figure 1.1.10 in the introduction).

	CellTracks Analyzer II		CellTracks (32.25X)		CellTracks TDI	
<b>A</b>	<b>Number of frames required to cover a sample chamber of 2.7x29.7mm<sup>2</sup></b>					
Sample area	Horiz.	Vert.	Horiz.	Vert.	Horiz.	Vert.
CCD Size(pixel)	1036	1384	1036	1384	900	150000
Sampling(um)	0.645	0.645	0.2	0.2	0.2	0.2
Effective size (mm)	0.67	0.89	0.21	0.28	0.18	30.00
Distance scanned in setup (mm)	3.34	31.24	2.90	29.89	2.88	30.00
Total Area (mm <sup>2</sup> )	104.4		86.7		86.4	
Frames	5	35	14	108	16	1
Total # Frames	175		1512		16	
<b>B</b>	<b>Total acquisition time per frame required for a measurement of 4 Channels</b>					
Integration DAPI	200 ms		200 Ms		30 s	
Integration FITC/BF	100 ms		100 Ms		30 s	
Integration PE	200 ms		200 Ms		30 s	
Integration APC	600 ms		600 Ms		30 s	
Total Integration 4 channels	1100 ms		1100 ms		120 s	
Overhead Time 4 channels	1868 ms		1868 ms		20 s	
Total acquisition 4 channels	2968 ms		2968 ms		140 s	
<b>C</b>	<b>Total acquisition time required to measure 4 channels and cover a complete sample chamber.</b>					
Total # images	175		1512		16	
Total integration	192.5 s		1663.2 s		1920 s	
Total overhead	327 s		2824 s		320 s	
Overhead %	62.9 %		62.9 %		16.3 %	
Integration %	37.1 %		37.1 %		85.7 %	
Total Acquisition	8.66 Min		79.78 Min		37.33 Min	

**Table 2.3.5** CTC sample acquisition parameters for the CellTracks Analyzer II, CellTracks (32.25 X) and the CellTracks TDI. A) Total number of frames to cover sample area. B) Typical Integration times and overhead time for each frame. C) Summary for the total acquisition time needed for a CTC sample.

This grooved structure is guiding the cells into a designated area of 6 separate lines which are only 80 micron in width. (The currently used illumination profile was specifically chosen for these grooves and is large enough to cover the complete width of these grooves.) This structure could reduce the acquisition time further down to 14 minutes. However this development is still in progress in our group and has not been implemented yet.

Furthermore, acquisition times could be brought down even further by using 2 or even more cameras simultaneously and imaging multiple channels in parallel. This would bring the acquisition times below the 9 minutes currently obtained with the CellTracks Analyzer II while maintaining resolution. However one should keep in mind that excitation and detection of multiple fluorophores simultaneously also results in increase of crosstalk of the fluorescent channels.

### **2.3.9 Specificity of CTC Identification**

#### ***Identification by specific probes***

The specificity of the identification of an object, most often a cell, can be created in several ways. In general the specificity is obtained by the use of highly specific probes. Flowcytometry relies on the quantification of one or more specific probes attached to a cellular object. The specificity of a flowcytometer is therefore limited by the degree of specificity of the different probes and scatter parameters of the object. The same holds for an image cytometer, because non-specifically bound fluorophores cannot be discriminated from the same fluorophore that is specifically bound. However for image cytometry additional specificity regarding a cellular object can be derived from morphological parameters. These may further identify an event, based on its specific staining pattern. In that way the specificity of an image cytometer is also determined by the optical resolution of the system.

#### ***Classification of CTCs by size and staining pattern.***

Several studies using image cytometry aim to obtain prognostic data based on the enumeration of CTCs in peripheral blood. It therefore should be noticed that image analysis is a crucial and critical part for image cytometry regarding CTCs. Most cytometric CTC detection systems rely on the final selection by an operator. In that sense the operator also determines the specificity. Current methods do not differentiate the full data set. Samples are quantified in absolute numbers of CTCs which is of course a valuable number but lacks qualitative information of the detected CTCs. It neglects the fact that CTCs form not just a homogeneous population. Typically a whole range of cellular objects related to CTCs can be detected. These range from small apoptotic bodies to fully intact CTCs. Such objects may demonstrate relevant parameters, like the size of the tumor or the clearance of the amount of CTCs which are shed into the bloodstream. Therefore the number of objects does not indicate straightforwardly the metastatic potential,



which would be ideal if one wants to use the number of objects as a measure for prognosis.

For these reasons it may be better to discriminate CTC objects into multiple classes and really exploit the extra specificity that is obtained with an image cytometer. As an example I will show some images (Figure 2.3.11-2.3.14) of CTCs from cancer patients obtained with the CellTracks TDI system. Each panel contains a single CTC, stained with a nuclear stain (DAPI), Cytokeratin-PE and in brightfield respectively. For each event the leukocyte marker is negative which is not shown.

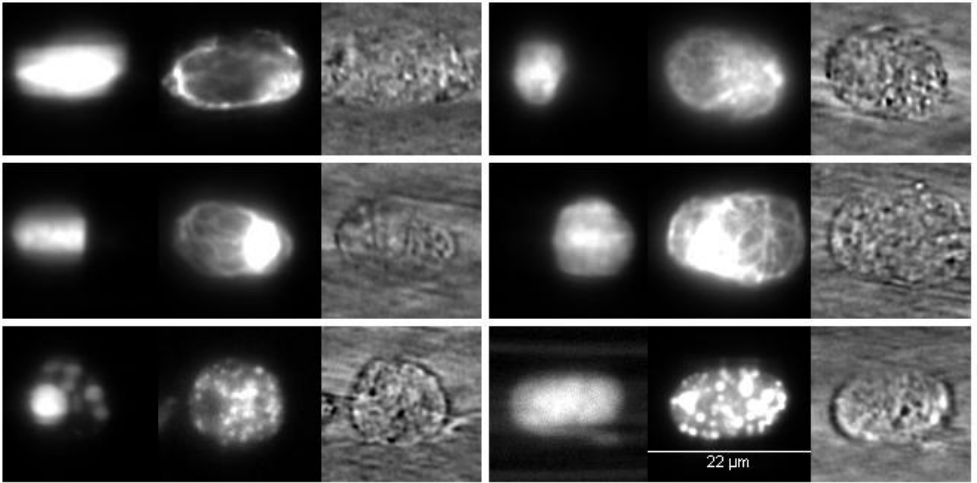


**Figure 2.3.11** Large size epithelial CTCs with various typical staining patterns and cytokeratin expressions. In each panel a single CTC with a nuclear stain (DAPI), Cytokeratin-PE and brightfield is shown respectively.

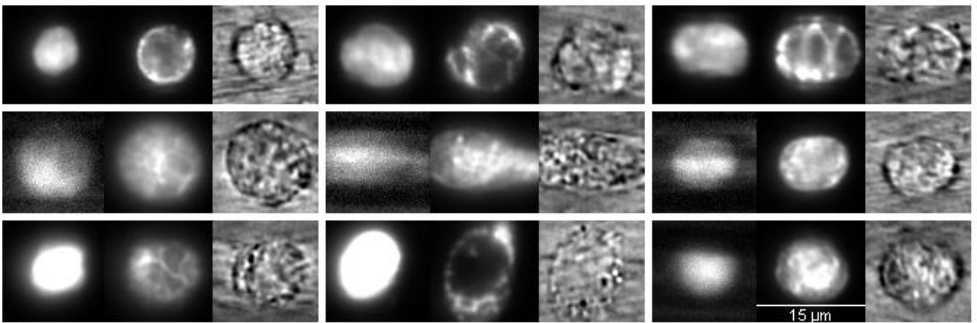


**Figure 2.3.12** Medium size epithelial CTCs In each panel a single CTC with a nuclear stain (DAPI), Cytokeratin-PE and brightfield is shown respectively.

These images demonstrate the large heterogeneity among CTCs. The variations not only depend on cancer type and patient but also vary within a single sample. The size of CTCs ranges from 4 to 40 micron, in contrast to leukocytes in the peripheral

blood which range from 6 to 11 micron. Most detected CTCs tend to be larger than the average leukocyte population.

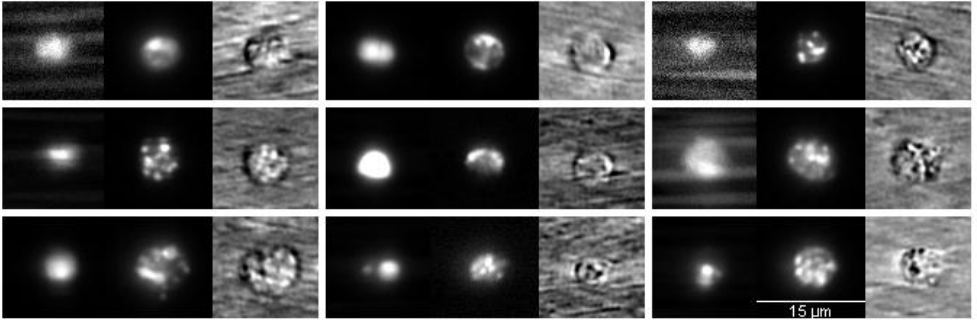


**Figure 2.3.13** Small sized epithelial CTCs. For each panel a single CTC with a nuclear stain (DAPI), Cytokeratin-PE and brightfield is shown respectively.

Besides size variations, CTCs show also large variations in cytoke­ratin expression and DNA content. Furthermore some cells show more or less specific cellular staining patterns as e.g. punctuated cytoke­ratin staining (Figure 2.3.14). These images are consistent with what one would expect for CTCs undergoing apoptosis.

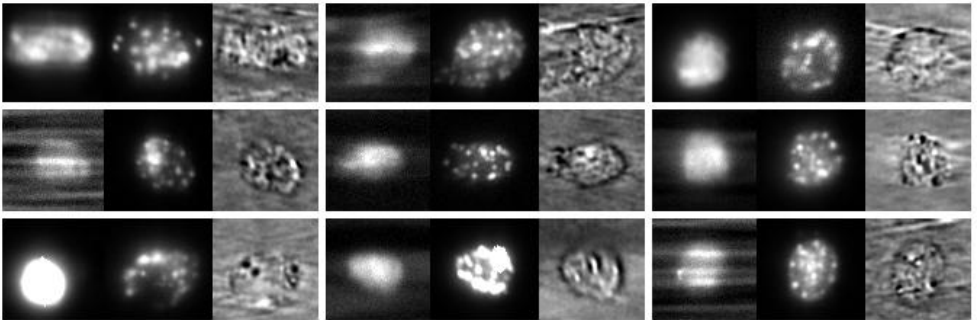


**Figure 2.3.14** CTCs with a punctuated cytoke­ratin staining. This is consistent with a CTC undergoing apoptosis.

To determine prognostic information from CTCs with metastatic potential it may be insufficient just to enumerate the CTCs based on a rudimentary selection protocol. Typical criteria currently used for identification are minimal size, oval to round morphology, positive cytoke­ratin staining, a visible nucleus and a negative staining for leukocytes. Based on these criteria all the images presented in this paragraph, may be classified as showing a CTC. However, this classification is probably not sufficient and may also be prone to errors. It may include a population of CTCs which are not likely to metastasize. As an example in figure 2.3.15 three events are reexamined with the CellTracks TDI.

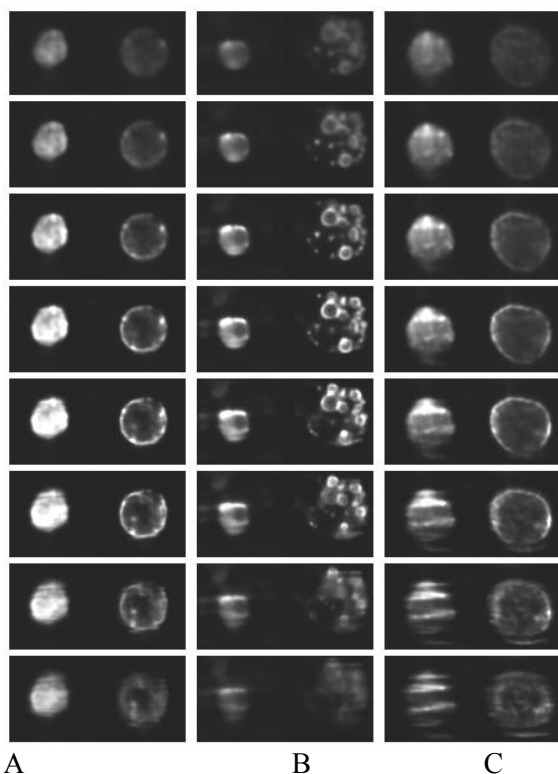


**Figure 2.3.15** Epithelial derived tumor cells reexamined by means of a 3D stack of multiple images. For each column a single CTC is analyzed whereas each row is acquired at a different depth with steps of 1 micron. Each panel shows a (DAPI) and a Cytokeratin-PE staining respectively.

In figure 2.3.15, the first column shows a single detected CTC out of a patient sample whereas the second and third columns show two CTCs from a second patient with a total of 13 assigned CTCs. However the majority of the counted CTCs in the latter sample 12 out of (13) had a punctuated cytoskeleton similar as shown in figure 2.3.15b, which points to apoptosis. This indicates that even though these CTCs are released massively in the bloodstream they may not have the potential to metastasize. In contrast, the patient sample in figure 2.3.15a does only have 1 CTC, however, that CTC seems to be in a rather good condition which may point that it forms a great risk.

It should be understood that no further conclusion may be drawn from these results due to the lack of clinical evidence. But it shows that specific interesting morphological features are clearly visible in the CellTracks TDI. These features are

normally not, or less clearly, visible when using a low resolution system like the CellTracks Analyzer II.

Finally when samples are reexamined for further identification by applying FISH probes, the higher resolution becomes an absolute necessity to discriminate consistently between these small probes.

# Part III Applications



## **3.1 Characterization of Circulating Tumor Cells by Image Cytometry**

### **3.1.1 Summary**

We developed the CellTracks TDI an image cytometer designed to improve the enumeration and characterization of Circulating Tumor Cells (CTCs). The system is equipped with a 40x NA 0.6 objective and lasers as light sources. Images are obtained in a continuous motion with a TDI camera minimizing the overhead time. To reduce inter-reader variability and limit manual review of the samples quantitative as well as morphological data of the acquired objects is obtained. The data is presented in scatter plots in combination with the associated images for each object and gates can be drawn to assign specific populations.

For this study the capabilities of the CellTracks TDI analysis platform was compared with the commercially available CellTracks Analyzer II. Blood samples of 26 metastatic carcinoma patients were screened for intact CTCs on both systems and showed a good correlation. In addition to intact CTCs the new instrument also identified and quantified CTC related debris and apoptotic CTCs. The number of apoptotic CTC and CTC related cell debris was larger than the number of intact CTC but showed a good correlation suggesting that a more accurate measurement of the presence of CTC may be obtained using this approach. Moreover enumeration of CTCs with CellTracks TDI can be obtained without review of an operator. The heterogeneity among events assigned as “true” CTCs is still large denoted by a large variation in cytokeratin expression, DNA content and staining patterns.

### **3.1.2 Introduction**

Circulating Tumor Cells (CTCs) can be present in the peripheral blood of cancer patients and their presence is associated with shortened survival.<sup>13-18</sup> The number of tumor cells, reported to be present in peripheral blood, varies greatly between studies, which largely can be attributed to the differences in sample preparation and analysis techniques. To minimize variability in rare cell analysis standardized and automated sample preparation is required. In the analysis of the samples the difficulty is to set criteria by which an event can be assigned as a tumor cell and that can be applied to different samples, instruments and operators. In this study CTCs were enriched from 7.5 ml blood samples and fluorescently labeled with the CellTracks Autoprep, an automated immunomagnetic sample preparation system.<sup>44-47</sup> The samples were first analyzed with the CellTracks Analyzer II a semi-automated fluorescence microscope<sup>38</sup> followed by analysis of the same samples on the CellTracks TDI. The numbers of CTCs detected by both systems are compared. In addition events related to CTCs were identified as apoptotic

CTCs and CTC-debris. These, events were quantified by CellTracks TDI analysis only.

### **3.1.3 Materials and methods**

#### ***Sample preparation***

Blood was drawn from 26 metastatic carcinoma patients in 10 ml CellSave Preservative evacuated blood collection tubes (Immunicon Corp., Huntingdon Valley, PA). Samples were kept at room temperature and processed within 72 hours. 7.5 ml aliquots of blood were centrifuged and placed in a CellTracks Autoprep. The system adds EpCAM antibody labeled ferrofluids that are specific for epithelial cells, to the blood sample and after incubation and magnetic separation, cells of epithelial origin are enriched. The sample is stained with the nucleic acid dye DAPI, Phycoerythrin labeled monoclonal antibodies directed against cytokeratin 8,18, 19 (PE-CK) and Allophycocyanin labeled monoclonal antibodies against CD45 (APC-CD45). Cytokeratins are cytoskeleton proteins present in cells of epithelial origin and CD45 is specific for leukocytes. After incubation the sample is placed into an analysis cartridge and placed in the MagNest™ Cell Presentation Device. This device is designed to present the magnetically labeled cells at the upper surface of the sample cartridge<sup>49</sup>.

#### ***CellTracks Analyzer II***

The CellTracks Analyzer II® is a four color semi-automated fluorescent microscope (Immunicon Corp., Huntingdon Valley, PA). The system uses a 10x NA 0.45 microscope objective and a digital camera to acquire images covering the entire surface of the sample chamber. After image analysis a gallery of objects stained for both cytokeratin (CK-PE) and nuclear content (DAPI) is shown to the operator. A trained operator makes the final selection based on morphological criteria. The selection criteria require the event to have a diameter of at least 4 micron, round to oval morphology, positive staining for cytokeratin, a clearly defined nucleus and negative staining for CD45-APC.

#### ***CellTracks TDI analyzer***

After the initial scan with the CellTracks analyzer II the sample is maintained in the MagNest and the sample is rescanned the same day with the CellTracks TDI system. For each sample images are acquired that cover the surface of the complete sample chamber for DAPI, PE-CK, APC-CD45 and additionally a bright field image. The CellTracks TDI uses a 40x NA 0.6 CFI Plan Fluor ELWD objective (Nikon, Tokyo, Japan) to obtain an increase of resolution and sampling density. To minimize total acquisition time due to this increase of sampling it uses a 12-bit TDI camera (Hamamatsu ORCA-ERT 12). Images are therefore acquired in continuous



motion to minimize total overhead time due to stage repositioning. Illumination is obtained with 375nm, 532nm, 639nm laser lines as excitation source for the fluorophores. Beam homogenizing optics (Suss-MicroOptics, Neuchatel, Switzerland) are used to create a square ( $180 \times 180 \mu\text{m}^2$ ) homogeneous illumination profile. The brightfield images are obtained with a blue LED underneath the sample.

After image acquisition of a sample, the initial 16.1 GB of 12-bit raw image data is processed with a script written in ImageJ.<sup>79,80</sup> The program applies a flat field correction and subtracts the background from all images. The signal level of the PE-CK images are used as a trigger channel and all objects with a level of 50 DN above background and larger than  $3 \mu\text{m}$  are considered a possible event. For these triggered positions expressing PE-CK, an area of  $30 \times 30 \mu\text{m}^2$  around the object is saved for DAPI, PE-CK, APC-CD45 and brightfield. This smaller data set of  $\sim 172$  Mb for 1000 events is processed further and the remaining image data (background) is discarded. The program determines a region of interest (ROI) for each PE-CK event by means of an Otsu threshold algorithm.<sup>92</sup> This region of interest is used as a measure for the object size and serves as a mask to determine quantitative information for an event. The corresponding region of interest for the nucleus stained with DAPI is also determined with an Otsu threshold. However, when determining the ROI for the nucleus it is restricted to the ROI of the PE-CK image. The center of the nucleus should be located within a radius of 10 micron of the center of the PE-CK ROI and has a maximum object size of 1.5 times the PE-CK ROI. If no object is found within these constrictions the same ROI is used as for the PE-CK image. The same restrictions hold for the APC-CD45 images. These restrictions are necessary to obtain a reliable ROI around each object. It prevents the selection of a ROI for DAPI and for CD45-APC of a neighboring object like a leukocyte. The size restriction with respect to the PE-CK ROI is necessary to prevent a selection of the complete background if no objects are found. Further image processing calculates quantitative and morphological information for all these events, therefore it uses the obtained ROIs for DAPI, PE-CK and APC-CD45 for each object.

The various quantitative fluorescence and morphological parameters obtained are presented in a dot plot and each event is linked to the actual image. This enables review of the sample by means of measured quantitative and morphologic parameters in combination with the obtained image for each event. Gates can be applied on the dotplot and the operator can further classify the detected populations.

### 3.1.4 Results

#### *Images of events after immunomagnetically enrichment for EpCAM expression*

Microscopic analysis of blood samples from metastatic carcinoma patients after immunomagnetic enrichment and fluorescent labeling yield a large variety of images. Typically the images from the events that passed the PE threshold can be divided into 3 populations as illustrated in figure 3.1.1 panels A, B and C. Panel A shows an event with a clear nucleus (DAPI), a cytoskeleton (Cytokeratin PE), no staining with the leukocyte marker (CD45-APC) and a bright field image showing a round to oval morphology. The images to the right display an overlay of DAPI / PE and DAPI / PE / bright field and are consistent with an epithelial cell and identified as CTC. Panel B shows an event with nuclear material, punctuated cytoskeleton staining, spotty staining with CD45-APC corresponding to the bright cytoskeleton punctuation and a bright field image showing a round to oval morphology. The typical cytoskeleton staining can be contributed to the collapse of the cytoskeleton which results in the retraction of the cytoskeleton filaments. The overlay images are consistent with a CTC undergoing apoptosis. Panel C shows an event that stains barely with DAPI, stains with cytoskeleton, not with CD45-APC and a small round particle in bright field image.

CD45-APC is added to the assay to avoid classification of leukocytes that stain non-specific with cytoskeleton as CTCs. Leukocytes that are carried over through the enrichment procedure but do not stain with cytoskeleton do not pass the cytoskeleton thresholds and are therefore not part of the final analysis. Figure 3.1.1 panel D shows the images associated with a leukocyte when the cytoskeleton threshold is not applied. The panel shows an event with a clear nucleus, no cytoskeleton PE, staining with the leukocyte marker and a bright field image showing a round morphology. The overlay images to the right are consistent with a lymphocyte. Figure 3.1.1 panel E shows the images associated with a leukocyte that passed the cytoskeleton PE threshold. The panel shows an event with a clear lobular nucleus, staining in the cytoskeleton PE channel, staining with the leukocyte marker and a bright field image showing an abundance of cytoplasmic granules and a round morphology. The overlay images to the right are consistent with an eosinophilic granulocyte. This positive staining in the cytoskeleton channel in this case may well be caused by the auto fluorescence of the cytoplasmic granules in the eosinophilic granulocyte that are known to be strongly autofluorescent<sup>87,88</sup> at a peak of 520 nm.

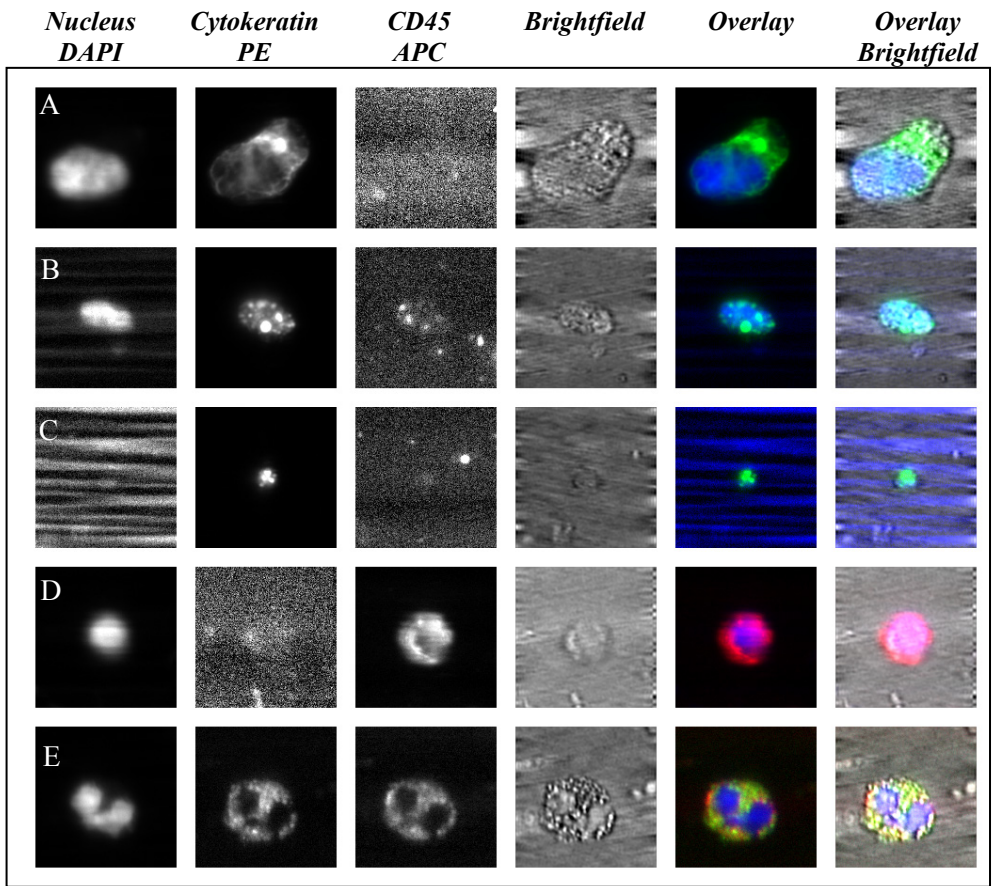


**Figure 3.1.1** CellTracks TDI images. (Image scale  $30 \times 30 \mu\text{m}^2$ ) Respectively for each row **A**) CTC; **B**) Apoptotic CTC; **C**) CTC debris (fragment); **D**) Leukocyte (lymphocyte); **E**) Leukocyte (autofluorescence or non-specific binding with cytokeratin-PE of an eosinophilic granulocyte)

### *CellTracks TDI data analysis*

The CellTracks TDI system identifies events that passed the Cytokeratin-PE threshold and measures several morphological parameters and quantitative fluorescence parameters for these events.

Figure 3.1.2 shows the measurement of a sample from a metastatic carcinoma patient. In these figures the total signal (integrated density of the fluorescent signal) of the corresponding fluorophores is plotted of each event. Panel A shows the total DAPI signal versus Cytokeratin-PE signal, Panel B shows the total DAPI signal versus the total CD45-APC signal, Panel C shows the total DAPI signal versus the ratio (total Cytokeratin-PE signal divided by the total CD45-APC

signal) and Panel D shows the total DAPI signal versus the size of the object in  $\mu\text{m}^2$ . Each dot represents an event that has passed the threshold and 5 clusters of events are identified and depicted with different colors. Three boxes in Panel C show the three regions with the CTC candidates. The events colored red have the highest DAPI signal and PE/APC ratio and represent intact CTC. Review of the images associated with the 6 CTCs confirmed that these indeed are classified as intact CTCs. The events colored green have intermediate DAPI signal, a high PE/APC ratio and are smaller in size (Panel D). Review of the images of the 15 green events showed that their features were consistent with late apoptotic CTC.

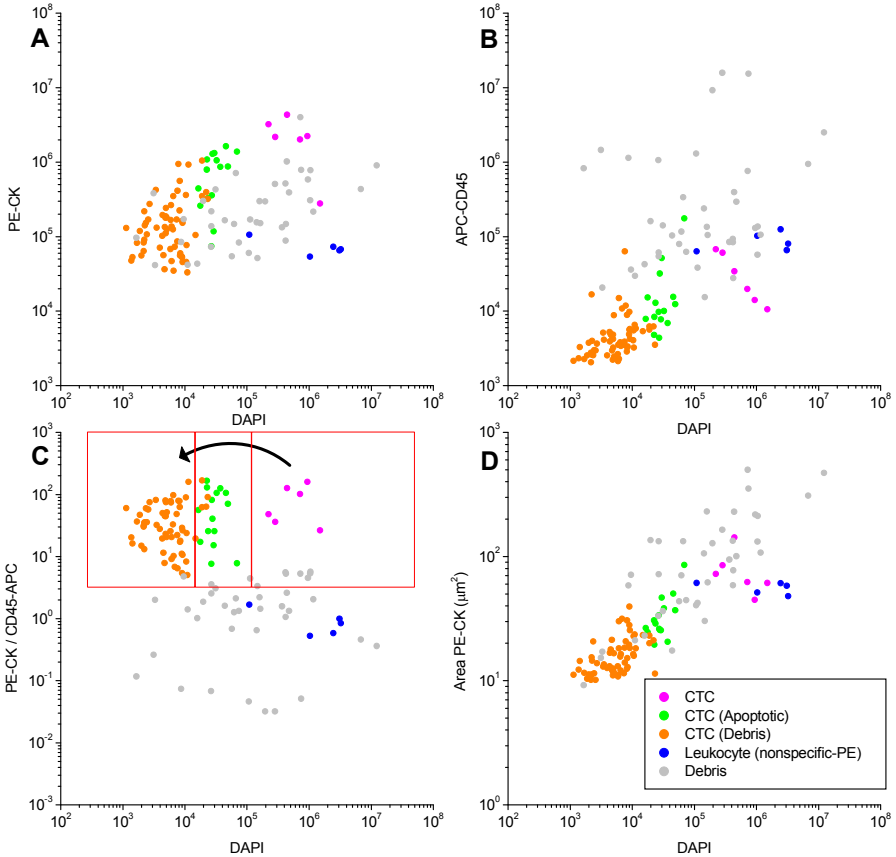


**Figure 3.1.2** Scatter plots of CellTracks TDI CTC analysis of blood from a metastatic carcinoma patient with CTCs detected by CellTracks.

Note that 2 events within the box are depicted grey and 4 events were depicted purple. In these instances morphological review did not confirm their identity as

late apoptotic CTC. The 61 events colored purple are not or weakly staining with DAPI, have a high PE/APC ratio and a small size ( $10 - 20 \mu\text{m}^2$ ). This is close to the size criterium of  $9 \mu\text{m}^2$  ( $\varnothing \sim 3\mu\text{m}$ ) used for events to pass the initial PE-threshold. Review of the images revealed small round particles that are considered a result of the degradation of tumor cells and referred to as tumor cell debris.

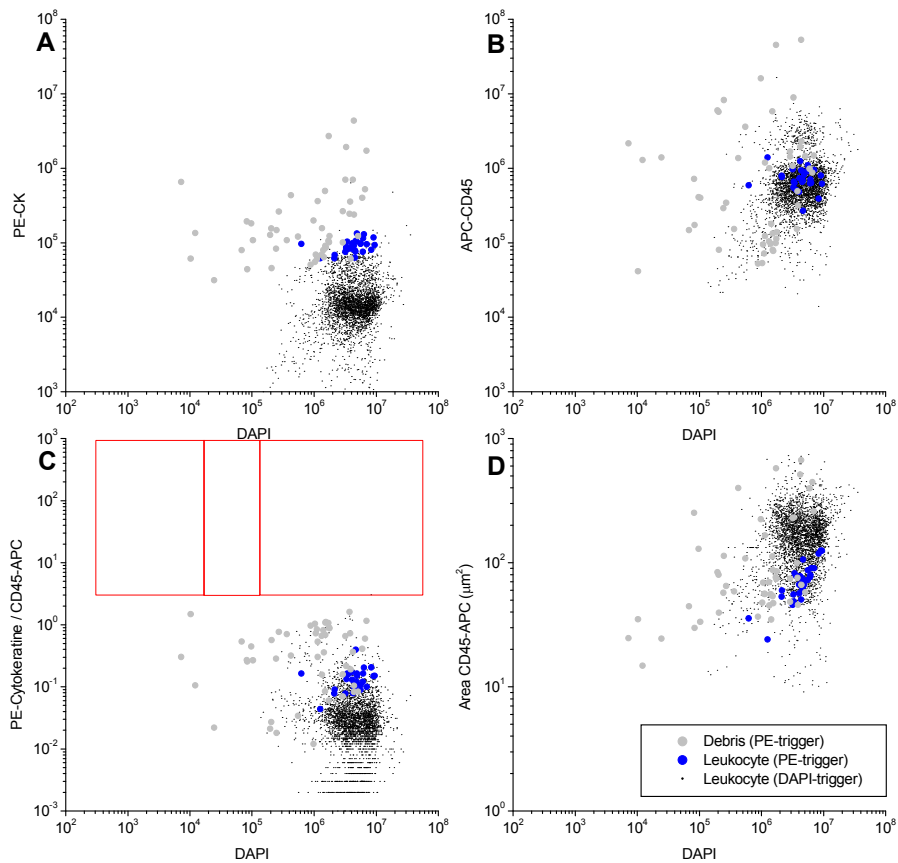


**Figure 3.1.3** Scatter plots of CellTracks TDI CTC analysis of blood from a metastatic carcinoma patient with no CTC detected.

All fragments smaller than  $3\mu\text{m}$  are not assigned as CTC debris, however they do appear in high quantities specifically for samples where CTCs are detected. Note that 4 events are located in the box with predominant green dots, after morphological review these events did not have sufficient features to qualify as apoptotic tumor cells. The events depicted blue have a high DAPI signal, a relatively low PE/APC ratio are identified as leukocytes staining non-specific for

PE-CK or displaying a high autofluorescence. The number of non-specifically stained leukocytes varied greatly between samples. Events that are not classified are depicted gray this debris stains positive in all channels have a strong correlation of the staining patterns and are mostly large and with diverse morphologic features that do not resemble a cell. The arrow indicated in Panel C shows the transition from intact CTC to CTC debris. This gradual transition with an increase of events and with no strict boundaries was observed in all samples that contained CTC.

Figure 3.1.3 shows the measurement from a sample of a metastatic carcinoma patient in which no CTC were detected. The displays are the same as shown in figure 3.1.2 except that events are also allowed that stain brightly with DAPI and not with cytokeratin. The black events in the dotplots represent the 3243 leukocytes (DAPI+,CK-PE-,CD45+) that are carried over through the sample preparation procedure. Note that no intact CTC were detected in the sample but also no events appeared in the boxes typical for apoptotic CTCs and CTC debris.

### ***Comparison of CTC analysis by CellTracks and CellTracks TDI***

Blood samples from 26 patients diagnosed with metastatic carcinoma were prepared for CTC analysis by the CellTracks Autoprep and analyzed by the CellTracks analyzer II. After analysis the same sample cartridge was analyzed by the CellTracks TDI.

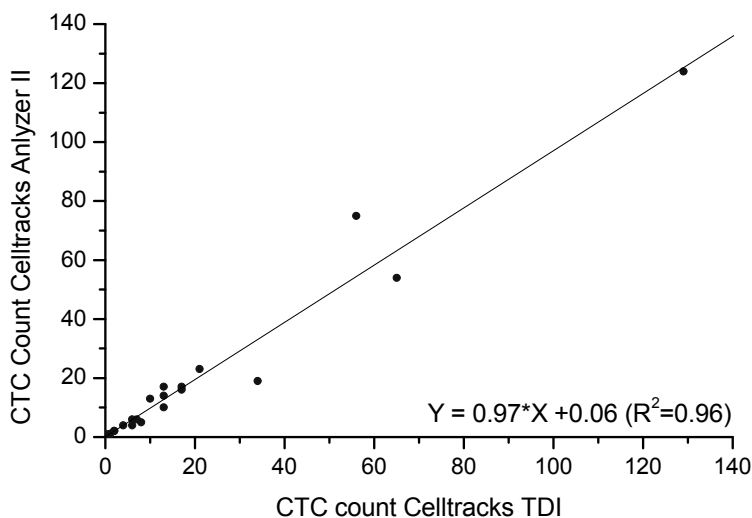


**Figure 3.1.4** CTC count CellTracks TDI versus CellTracks Analyzer II

The comparison of the CTC analysis of both instruments is shown in table 3.1.1. In the table the samples are sorted according to increasing CTC number reported after CellTracks Analyzer II data review. For the CellTracks TDI the apoptotic CTC, tumor cell debris, non-specific staining leukocytes and background events are also listed in the table. The comparison of the number of CTC detected by both instruments is illustrated in figure 3.1.4 and shows a good correlation ( $R^2 = 0.96$ ) with a slope close to 1 and an intercept close to zero.

#	CTAI	CTTDI	#CTC	#CTC	#CTC	#WBC	#Background
	#CTC	Intact	Apoptotic	Debris	Total		Debris
1	0	0	0	0	0	29	51
2	0	0	0	6	6	426	65
3	0	0	0	4	4	174	87
4	0	0	0	1	1	223	62
5	0	0	0	4	4	522	112
6	1	0	0	3	3	3	368
7	1	1	0	8	9	4	92
8	1	1	0	11	12	20	78
9	2	2	6	24	32	5	67
10	2	2	0	12	14	6	54
11	4	4	5	75	84	4	28
12	4	6	6	55	67	155	66
13	5	8	6	113	127	13	95
14	6	6	15	61	82	5	40
15	6	7	11	119	137	3	40
16	10	13	26	194	233	0	35
17	13	10	9	186	205	13	90
18	14	13	24	267	304	6	58
19	16	17	30	176	223	135	148
20	17	13	11	125	149	774	155
21	17	17	12	292	321	700	130
22	19	34	61	624	719	46	200
23	23	21	30	267	318	0	31
24	54	65	62	696	823	2	406
25	75	56	79	386	521	22	123
26	124	129	150	923	1202	2	71

**Table 3.1.1** CTC analysis of blood samples from 26 patients with metastatic carcinomas analyzed with the CellTracks analyzer II and CellTracks TDI system.

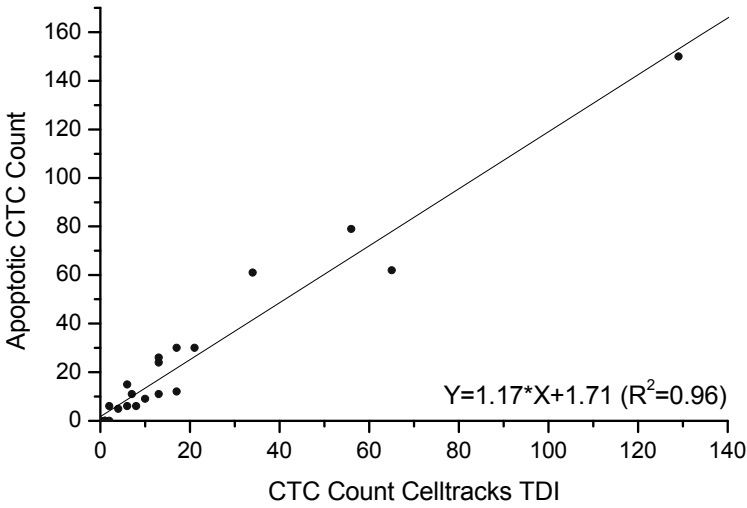


**Figure 3.1.5** Apoptotic CTC versus intact CTC count

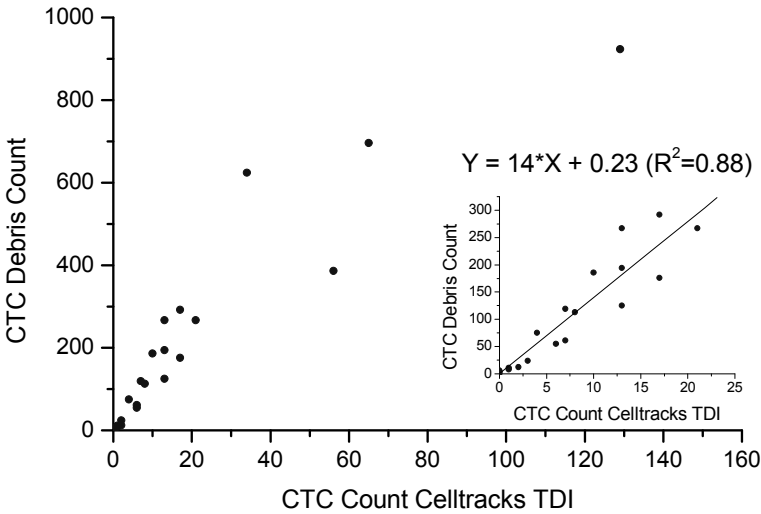


**Figure 3.1.6** CTC debris versus intact CTC count.

Figure 3.1.5 shows the relation between intact CTC and apoptotic CTC. The presence of apoptotic CTC is clearly correlated with the presence of intact CTC ( $R^2 = 0.96$ ) and the slope of 1.17 with an intercept of 1.71 suggest a slightly larger



number of apoptotic tumor cells. These analyses also suggest that the late apoptotic tumor cells are not classified as CTC in the CellTracks analyzer II data review. Figure 3.1.6 shows the comparison between intact CTC and CTC-debris and also shows a clear correlation ( $R^2=0.88$ ). The slope of 14X indicates a large proportion of CTC-debris in samples that contain intact CTC and the intercept of 0.23 indicates that no CTC-debris is present when intact CTC are absent. The insert in figure 3.1.6 shows the samples with less than 25 CTC.

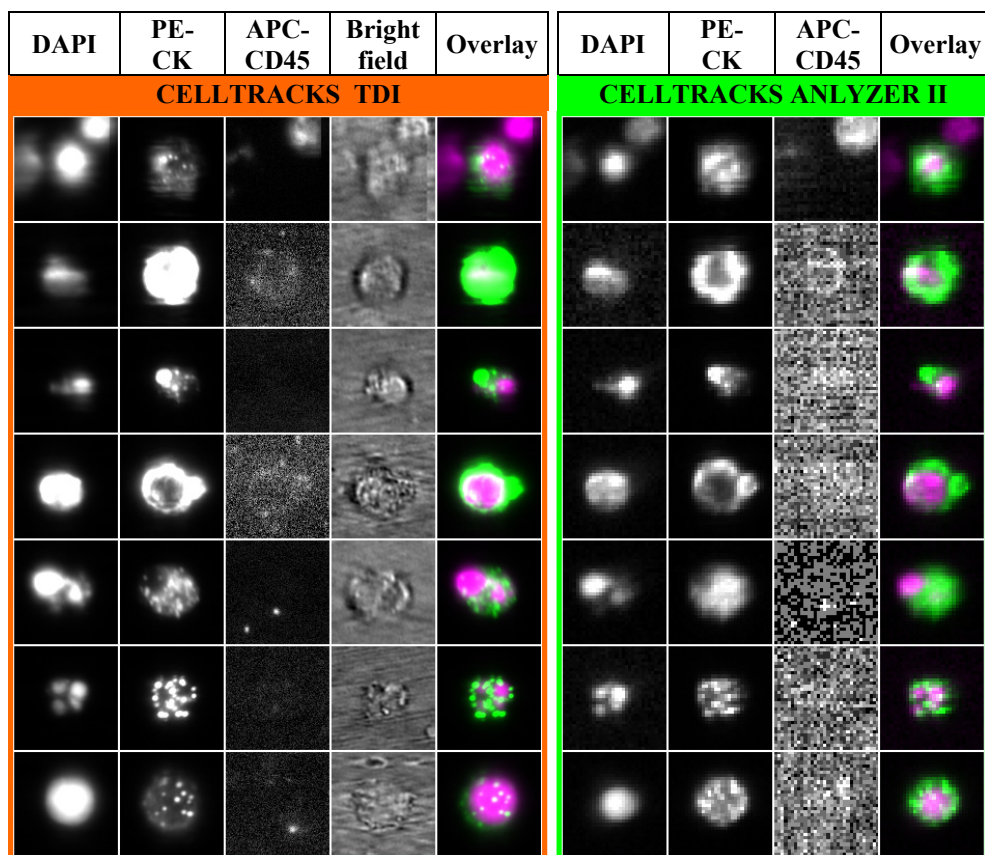


**Figure 3.1.7** Images obtained with the CellTracks TDI and the CellTracks analyzer II. (Image scale  $20 \times 20 \mu\text{m}^2$ )

As the same samples were analyzed by both systems the actual detected cells were traced back to make a direct comparison of the CTC images from both systems. In figure 3.1.7 seven images of CTCs detected by both systems are shown. The side by side comparison illustrates the higher resolution of the CellTracks TDI images and the additional information obtained by collection of the bright field image. The additional information assists the operator and/or the analysis software to

discriminate between the different populations. The example in the third row of figure 3.1.7 shows that the bright field image provides information that the object has indeed features consistent with that of a cell. Figure 3.1.8 shows an enlarged image of the nucleus and cytokeatin of the cells shown in row 5 and 6 of figure 3.1.7. The higher resolution of the CellTracks TDI images permits the identification of typical apoptotic features in the cells.

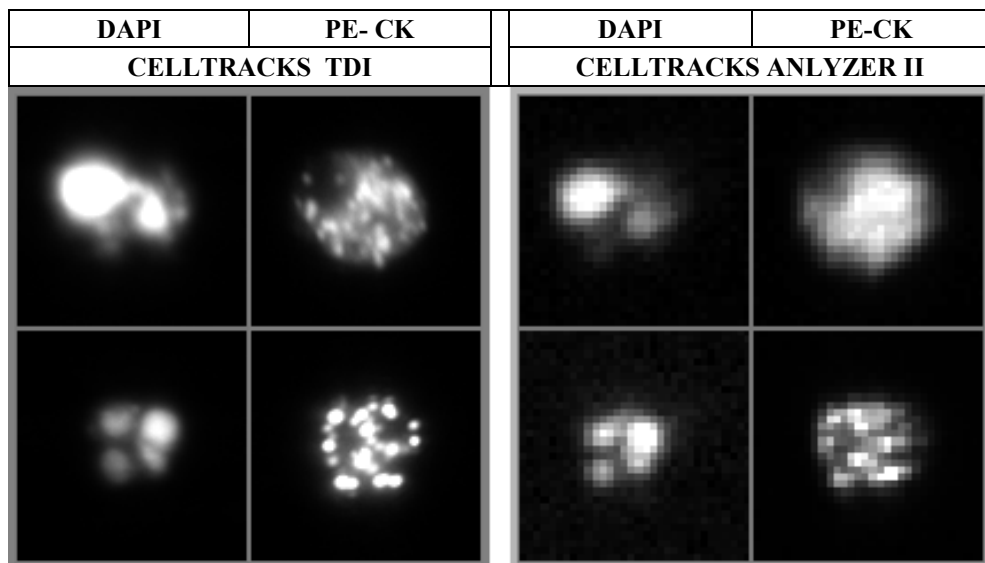


**Figure 3.1.8** Enlarged images obtained with the CellTracks TDI and the CellTracks analyzer II of DAPI and PE-cytokeatin of CTC from row 5 and 6 of figure 3.1.7. (Image scale  $20 \times 20 \mu\text{m}^2$ )

### 3.1.5 Discussion

The samples analyzed with the CellTracks analyzer II are used to count the number of intact CTC which are selected by an operator. With the CellTracks TDI we counted besides intact CTC also the apoptotic CTC, CTC-debris, leukocytes and debris. This count is based on quantitative information of PE, APC and DAPI staining shown in dotplots as well as manual review of the images.

The major differences between these setups are the microscope objective 10X NA 0.45 versus a 40X NA 0.6 objective. This results in a higher sampling resolution of the CellTracks TDI setup. Furthermore the CellTracks TDI setup uses 4 laser lines as excitation sources whereas the CellTracks analyzer II uses the spectral lines of a traditional mercury arc lamp. The TDI camera in the CellTracks TDI setup is used to minimize the acquisition time by reducing overhead time due to stage repositioning and camera readout. These differences results in a higher resolution

and increase of sensitivity and make it possible to better classify the CTC in different subpopulations based on quantitative and morphological parameters. The events assigned as a “true” intact CTC for the CellTracks TDI are based on selection criteria which are also used for the CellTracks Analyzer II. These events resemble intact cells with a round to oval morphology are larger than 4 micron, stain with cytokeratin, have a clear defined nucleus and do not stain with CD45-APC. A comparison of the intact CTC count between both systems show the same number of CTCs, figure 3.1.4. The slope and the intercept are close to 1 and 0 respectively. A direct comparison was obtained by manual inspection of each event classified as CTC by both systems and indeed confirmed that the same objects were selected as CTCs.

Although the same objects were selected as intact CTC, the increased resolution of the CellTracks TDI gives the possibility to better identify typical apoptotic features in the cells as shown in figure 3.1.8. This gives the possibility to further differentiate this population into intact CTCs with or without signs of cell death. It revealed that most of the events, assigned as intact CTCs show some degrees of caspase cleavage of the cytokeratin. On the other hand some CTCs were in a very good shape and do not show any sign of cell death. This might indicate a resistant CTC with a highly metastatic potential. One might hypothesize that a patient sample with just one or more of these well preserved CTCs could indicate a worse prognosis. On the other hand a patient sample containing more intact CTC with signs of cell death could indicate a better prognosis. The later cells are not likely to proliferate, and more or less indicate inefficient clearance for a massive shed of tumor cells into the bloodstream. Enumeration of these “well preserved” CTCs may therefore be a good indicator for prognosis instead of enumeration of all the intact CTCs based on a rudimentary selection protocol.

CTC assignment by the CellTracks analyzer II relies on the final selection by an operator on a set of pre selected events by the computer based on PE-cytokeratin and DNA content. The images presented to the operator are auto scaled to increase visibility. The human eye, however can only discern approximately 100 gray levels making deduction of quantitative information by the operator from these images difficult. In auto scaled images the relation between “true” signal and background is less apparent. A dim nucleus may appear just as bright as a brighter nucleus. Furthermore a slight difference in monitor settings may already result in a different interpretation by the operator. Besides the difficulties to manually review a sample, a large portion of cytokeratin positive events with or without a dim nucleus are rejected by the CellTracks Analyzer II. These objects may provide additional information on the total CTC count, but are omitted to prevent an excessive amount of objects to be reviewed manually. The dotplots as used in the CellTracks TDI are therefore a powerful tool to assist the operator in the CTC selection. Quantitative information analyzed by the computer is fast and consistent and reduces inter-reader variability. Furthermore it could limit the manual review to

only objects in the dotplot which are most likely to resemble a CTC and assign non intact CTCs and CTC related debris automatically.

The dotplots also pinpoints to another aspect of the CTC samples. As shown in figure 3.1.1 there is a shift of the events in the three boxes from right to left. It shows a transition from a fully intact CTC to small cellular fragments. During apoptosis the cytokeratin intensity is slightly reduced, likely caused by caspase cleavage of the cytokeratin and a condensing of the DNA. This gradual transition hampers the visual inspection by an operator. Since the difference between an intact CTC and an apoptotic CTC can be very subtle it will give rise to inter-reader variability.

The data in figure 3.1.6 shows that there is clear correlation between CTC debris and the number of intact CTC. This indicates that the small PE-cytokeratin fragments are real CTC debris and not just an aggregation of the PE fluorophore. One explanation for this debris of CTCs is that it is caused by mechanical stress during the immunomagnetical enrichment resulting in a destruction of intact CTC. Although this is not likely it will need to be excluded. This can be achieved by analysis of blood samples with an abundance of CTC debris which permit the processing and analysis of the sample without immunomagnetic enrichment. Presence of apoptotic bodies near the tumor site and in the blood stream are reported by others<sup>105-107,20</sup> and presence of caspase cleaved cytokeratin is reportedly increased in serum of patients with carcinomas<sup>108-111</sup> supporting the notion that the detected tumor debris with the CellTracksTDI is indeed directly related to the presence of tumor.

However, the question remains how these relatively small cytokeratine positive apoptotic bodies enter the blood stream. Are they released from the primary tumor or do they originate from CTC that disassembled in the blood stream. The correlation between intact CTC and CTC fragments suggest that they may have diagnostic potential. These objects are more frequent and can therefore be enumerated with a smaller statistical error.<sup>112</sup> Their clinical utility will however need to be assessed in clinical studies.

## **3.2 Identification of aneuploidy in Circulating Tumor Cells by a Laser Image Cytometer**

### **3.2.1 Summary**

We designed an image cytometer to enumerate Circulating Tumor Cells (CTCs) in a consistent and automated manner. This instrument, the “CellTracks TDI” uses a 40x NA 0.6 objective, lasers as light source and a TDI camera to acquire images in continuous motion. This avoids overhead time caused by the multiple repositioning steps of the XY stages common for a frame by frame scanning system. For this study the reexamination capabilities of the CellTracks TDI platform are evaluated. SKBR-3 cells spiked into 7.5 ml sample were immunomagnetically enriched, fluorescently labeled and analyzed by the image cytometer. The events detected by the analyzer were traced back and a 3D Z-stack is acquired to obtain more morphological detail. After the reexamination the sample is relabeled with FISH probes identifying locus Xq12 and 21q22.13 and the sample is examined again. To remove out of focus blur of the images in the Z-stack, deconvolution is applied on the stored images. This results in an increase of contrast and improves the accuracy for counting the small FISH probes. The data shows that multiple reexamination and relabeling steps are possible and can be applied in a consistent and automated manner.

### **3.2.2 Introduction**

The presence of circulating tumor cells (CTCs) in patients with metastatic carcinomas is associated with poor survival prospects<sup>13-18</sup>. Previously it has been demonstrated that chromosomal abnormalities in circulating tumor cells reflect those observed in the primary tumor.<sup>26</sup> In cases where few tumor cells are detected the question arises whether the detected events are indeed tumor cells. Detection of abnormal chromosome copy number in these cells can enable a confirmation that the detected cells are indeed cancerous. This can be achieved by enumeration of chromosomes with fluorescence in-situ hybridization (FISH). In this study the CellTracks TDI system was evaluated for its capability to enumerate chromosome copy numbers in cells identified as CTC and a model system was used in which cells from the breast cancer line SKBR-3 were spiked into a buffer solution and processed with an automated CTC isolation and staining system.

### 3.2.3 Materials and methods

#### *Cell Spiking*

Cells from the breast cancer cell line SKBR-3 (ATCC, Middlesex, UK) were cultured in RPMI 1640 Glutamax-I medium (Invitrogen, Carlsbad, CA). Cells were harvested and counted. 50 $\mu$ l volume containing ~ 35 SKBR-3 cells was spiked into 7.5 ml of a buffer solution.

#### *Tumor cell isolation and staining*

The CellTracks Autoprep<sup>44-47</sup> an automated sample preparation system (Immunicon Corp., Huntingdon Valley, PA), was used to process the 7.5 ml sample spiked with SKBR-3 cells. Ferrofluids coated with antibodies directed against the epithelial cell adhesion molecule (EpCAM) specific for cells of epithelial origin are incubated with the sample and used to immunomagnetically enrich for epithelial cells. The enriched samples are stained by the system with the nuclear acid dye DAPI, Phycoerythrin conjugated monoclonal antibodies recognizing cytokeratine 8,18 and 19 specific for the cytoskeleton of epithelial cells (PE-CK) and Allophycocyanin conjugated to the leukocyte specific monoclonal antibodies CD45 (APC-CD45). The CD45 was not used in the present analysis.

After incubation the sample is placed into the analysis cartridge and placed in the MagNest<sup>TM</sup> Cell Presentation Device. The device is designed to present the magnetically labeled cells at the upper surface of the sample cartridge. The cells maintain their position during the measurement.

#### *Tumor Cell Analysis by CellTracks TDI*

The MagNest containing the sample is placed in the CellTracks TDI system. The system is equipped with a 12-bit TDI camera (Hamamatsu ORCA-ERT 12), a 40x NA 0.6 objective, and 3 lasers with 375nm, 532nm, 639nm laser lines available for excitation. A blue LED positioned below the MagNest is used as a light source to obtain a bright field image. Due to the high cytokeratine expression of the SKBR-3 cell line is the excitation power of the 532nm laser reduced with a factor ~16. This reduces sensitivity and prevents saturation of the PE-CK signal. For each analysis DAPI, PE-CK and bright field images are acquired to cover the complete surface of the sample chamber. After image acquisition the images are processed. The PE-CK images are used as a trigger channel and all the objects expressing PE-CK are selected. The threshold allows events in the analysis when a 9  $\mu$ m<sup>2</sup> area containing 225 pixels exceeds 50 DN. This value represents approximately 7000 PE molecules. Smaller and dimmer objects are all treated as background and excluded. This minimizes the remaining dataset to just a few events which are processed further. For these events masks are established from each channel with an Otsu

threshold algorithm.<sup>92</sup> They are all compared and size and position criteria are used to determine the ultimate mask that covers the proper area of the object. With these masks quantitative and morphological information is obtained for each object. The correlation of the quantitative and morphological information for each object is shown in a dot plot. The actual images providing the morphologic information can be viewed simultaneously by selection of an event in the dot plots. An operator classifies the population of interest based on the quantitative and morphological information and can choose to obtain more detailed information of events of interest. The system maintains the positional information of each event and can travel back to the event of interest to acquire a Z-stack of images to obtain image detail in three dimensions. In the used setting, the system obtained a Z-stack of 41 slices (20 slices above and 20 stacks below the initial focus position) for the PE-CK, DAPI and bright field channel accordingly before moving to the next event. The obtained Z-stacks are sampled with a step size of 1 micron for each step, this is small enough to fulfill the Nyquist sampling criteria for a 0.6 NA microscope objective.<sup>76,77</sup>

### ***Sample preparation for FISH analysis***

After examination of the sample the MagNest containing the cartridge is removed from the scanning system. The cartridge plug is detached and the cells were fixed to the analysis surface by a gradual replacement of the buffer by Methanol/Acidic acid (3:1) followed by a 2 minute incubation. After fixation, the Methanol/Acidic acid is removed followed by immediate air drying for 2 minutes using air flow (100 liter/hour). The cells now adhere firmly to the glass surface and the sample cartridge can be removed from the MagNest. The cells are labeled with FISH probes identifying locus 21q22.13 and Xq12. Repeat sequence free PCR products of the BAC clones, CTD-2511E13, RP11-95G19 and RP11-720N21, were used for locus 21q22.13, and labeled with FISHBright 647 Far Red (Kreatech, Amsterdam). Repeat free PCR products of BAC clones RP11-383C12 RP11-479J1 and RP11-963N10, were used for locus Xq12, and were labeled with FISHBright 550 Orange/Red (Kreatech, Amsterdam, Netherlands). The labeled clones were pooled and diluted to 8 ng/ $\mu$ l total concentration in a hybmix consisting of 50% deionized formamide, 1xSSC and 10% dextran sulfate. 50  $\mu$ l of the hybmix was inserted in the cartridge and spread over the surface. The cartridge is placed on a hotplate and is heated to 80°C for 2 minutes, followed by cooling to 42°C. The cartridges are closed and left to hybridize on the hotplate overnight at 42°C. After hybridization the hybmix is replaced by 20%formamide, 0.1xSSC, 1  $\mu$ M DAPI and cartridges are incubated for 10 minutes on a 45 °C hotplate. After incubation the wash buffer is replaced by PBS and the sample is analyzed.

### ***Enumeration of FISH probes by CellTracks TDI***

The relabeled sample is inserted in a MagNest from which the magnets are removed and placed in the analysis system. The previously recorded locations are reloaded and after an initial alignment of the system, each event of interest is revisited. Z-stacks containing 41 slices with a step size of 1 micron are obtained for DAPI, FISHBright 550, FISHBright 647 and bright field.

### ***Analysis of reexamined events.***

The Z-stacks of the 2 reexamination cycles (before and after FISH) of a sample are all realigned. This realignment is used to obtain perfect overlapping images for both reexamination cycles as the cells can slightly move (1 – 10 micron) during FISH preparations. The shift in these images is obtained by correlating the DAPI signal for both reexaminations. Accordingly the images are cropped to 300x300 pixels to reduce the size of the images and minimize the processing time for deconvolution. The Huygens professional image analysis program is used for deconvolution<sup>93,94</sup> of the images (Scientific Volume Imaging, Hilversum, Netherlands). This reduces the out of focus light from the images in the Z-stacks. The 3 dimensional Z-stack images permit the identification of the fluorescence spots identifying the specific chromosomes in the cells.

## **3.2.4 Results**

### ***Identification of SKBR cells***

The immunomagnetically enriched and fluorescently labeled samples were scanned with the CellTracks TDI. The total surface area of an analysis cartridge is approximately 81 mm<sup>2</sup>. A first scan covering the complete surface is performed with a lateral sampling resolution of 0.2 μm for DAPI, CK-PE and bright field respectively. To prevent saturation due to the PE fluorochrome in the SKBR-3 cells that express cytokeratins at high density, the excitation power was reduced by placement of an ND16 filter in front of the 532nm laser. The DAPI excitation was reduced by placement of a ND4 filter in front of the 375nm laser. Panel A of Figure 3.2.1 shows an image of the PE expression across the complete surface of the analysis chamber. Panel B shows a magnification of one area and reveals the presence of two objects that stain with PE. A further magnification of the selected object reveals the identity. The DAPI, CK-PE, bright field, filtered bright field, DAPI and CK-PE overlay images show that one object is an intact SKBR-3 cell Panel C. The other object shown in panel D reveals a SKBR-3 cell fragment. The horizontal black lines visible in the bright field image represent the ~180nm ferrofluids that align under the influence of the magnetic field.



To minimize the influence of the ferrofluids the images are filtered by means of a fast fourier transform (FFT) filter. This is used to reduce the typical frequencies associated with the horizontally striped ferrofluid pattern, thereby improving the visualization of bright field images of the objects of interest.

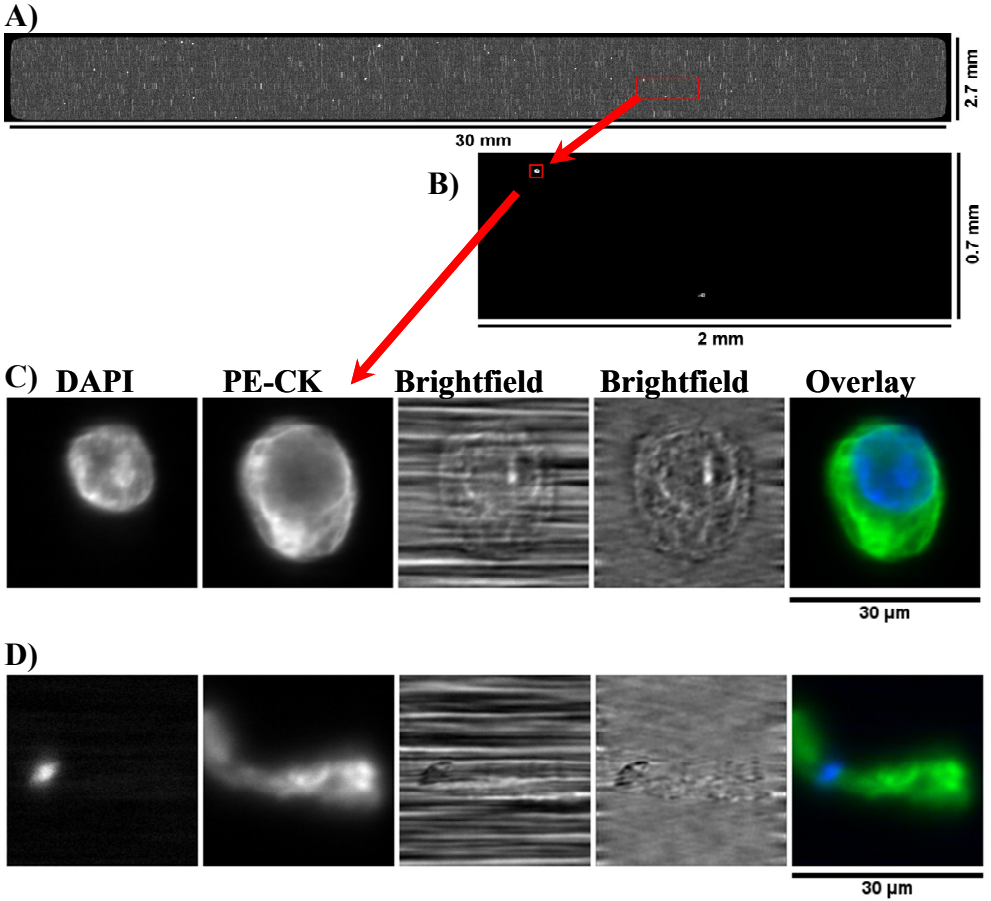


**Figure 3.2.1.** Images acquired in TDI mode of the sample cartridge.

A) Image of PE expression over the entire scan area B) Zoom of selected area indicated in Panel A. Panel C images of DAPI, CK-PE, bright field, filtered bright field, DAPI and CK-PE overlay from an intact SKBR-3 cell, object 1 in Panel B and in Panel D the images of a SKBR-3 cell fragment .

After data acquisition the images are processed and quantitative information is obtained from locations that exceeded the PE-CK threshold and were considered events. Figure 3.2.2 illustrates the integrated fluorescence intensity of DAPI and CK-PE from the sample shown in Figure 3.2.1 Panel A.

The 18 events colored red have the highest fluorescence intensity with both DAPI and CK-PE and the 14 events colored green show a gradual decline in the fluorescence of both parameters. The border between red and green was established by review of the images of each of the events. All red events were intact SKBR-3 cells whereas none of the green events had morphologic features consistent with an intact cell.

It should be noted that some events contained a cluster of SKBR-3 cells. This is caused by the adherent properties of these cells that were clustered when they were spiked in the blood. Furthermore most fragments and debris were relatively large and may have been damaged due to mechanical stress when harvesting SKBR-3 cells with a cell scraper from the culture dish.

The images associated with the two highlighted events in the dot plot are shown in figure 3.2.1 Panels C and D.

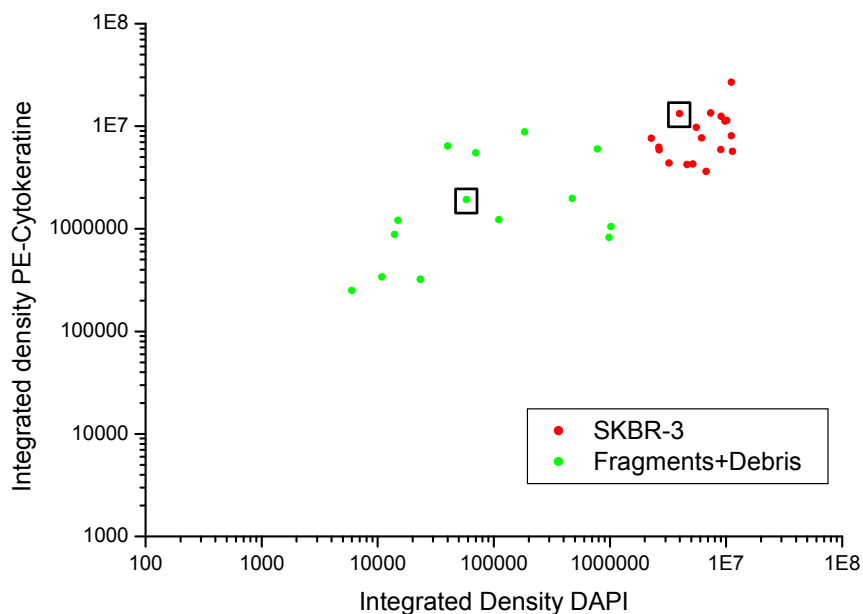


**Figure 3.2.2.** Dotplot Integrated fluorescence density of CK-PE and DAPI. The boxed events in the dot plot correspond to the images shown in figure 3.2.1c and figure 3.2.1d

### *Revisiting events of interest*

After image analysis the exact position of all events is known. The quantitative and morphological data of these events is shown in dot plots together with the corresponding images. Based on this data only a few events are relevant and are selected for reexamination. An example of a more detailed analysis of an event of

interest is shown in figure 3.2.3 The sample is repositioned in the system and moves to the position in which the event of interest was detected. During reexamination a Z-stack is obtained for each channel. To adjust the Z-position a piezo microscope objective positioner MIPOS 500 (piezosystem jena GmbH, Jena, Germany) is used. This stack contains 20 slices above and below the initial focus position with steps of 1 micron. The left side of figure 3.2.3 shows 9-slices of DAPI, CK-PE and bright field through the relocated event. Revisiting of 75 events in a set of 3 experiments showed that all events are still in the same position. The magnetic field in the MagNest is thus sufficient to maintain the position of the cells at the top glass surface.

### ***Revisiting events for evaluation of FISH results***

Cells of interest were revisited again after the extensive sample preparations associated with the hybridization of the fluorescent probes. Seventy-five events were revisited and only a slight movement of 1 to 10 micron relative to the glass surface of the chamber was observed. The fluid from the sample chamber from which the analysis is shown in Figure 3.2.2 was removed and the cells at the glass surface were fixed to permit the FISH procedure. In this example the sample chamber was hybridized with FISH probes specific for Chromosome Xq12 labeled with FISHBright 550 and Chromosome 21q22.13 labeled with FISHBright 647 and the nuclear staining with DAPI was repeated. After completion of the hybridization the sample is inserted back in the CellTracks TDI. The previously obtained position data is reloaded and the system realigns and obtains the information necessary for adequate focus of the events. The system revisits all events and creates a Z-stack of 41 slices for each DAPI, FISH 1 (FISHBright 550), FISH2 (FISHBright 647) and bright field.

DAPI	CK	BF	DAPI 2	FISH 1	FISH 2	BF 2	
Before FISH preparations			After FISH preparations				
							-5
							-4
							-3
							-2
							-1
							0
							+1
							+2
							+3
							+4

**Figure 3.2.3.** The selected event shown in figure 3.2.2 and 3.2.1c was reexamined. After image analysis, the system returns to this event and measures a Z-stack of 41 slices with a step size of 1

micron. The first 3 columns are acquired prior to FISH, showing DAPI, CK-PE and bright field. The last four columns display the same event and reexamined after FISH preparations. The images shown are respectively DAPI, FISH1: Chromosome Xq12 labeled with FISHBright 550, FISH2: Chromosome 21q22.13 labeled with FISHBright 647, bright field. (Image scale 30x30  $\mu\text{m}^2$ )

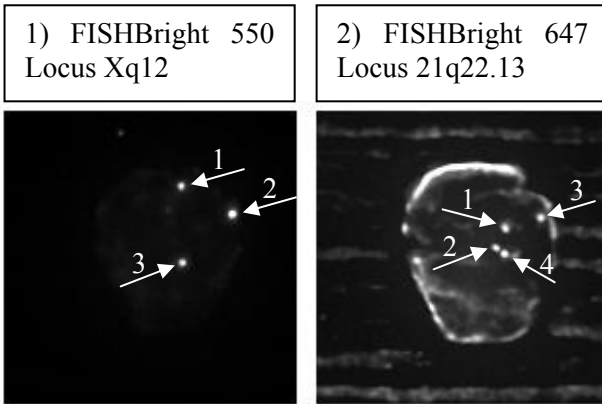


**Figure 3.2.4** Maximum intensity Z-projection of the z-stack shown in figure 3.2.3 for FISH probe 1 and 2 respectively. (Image scale 30x30  $\mu\text{m}^2$ )

To correct for the possible 1 to 10 micron movements of the cells, the DAPI signal of the first data acquisition is correlated with the second DAPI data acquisition and the samples are aligned accordingly. The DAPI, FISH 1 (Chromosome Xq12), FISH2 (Chromosome 21q22.13) and bright field images of this analysis are shown at the right panels of figure 3.2.3. Examination of the 9 DAPI slices permits visualization of the nucleus in the X, Y and Z plane. The small probes are clearly visible and appearing at different positions and depths of the nucleus. The fluorescent images shown are all optimized by effectively removing out of focus light by deconvolution of the images. The software effectively brings the light back to the source. This improves image quality and contrast which makes the small FISH probes easier to be discriminated for automated and manual counting of the probes. The locations of locus q12 on chromosome X can be found in slice -3 through +2. Fluorescent signals can be observed in three different locations indicating an abnormal copy number of chromosome X. At slice -1 all three dots can be seen. The locations of q22.13 on chromosome 21 can be found in slice -4 through +3. This is more easily observed with a maximum intensity Z-projection of the FISH probes as shown in figure 3.2.4. The copy number of chromosome X is clearly 3 and 4 for chromosome 21. It is also apparent that there is still a relatively large background staining at the cell surface for FISHBright 647

### *Assessment of aneuploidy*

Three samples spiked with SKBR-3 cells were prepared. From each sample 25 events were selected and investigated for the number of copies of chromosome X and 21. The 75 events contained 106 nuclei caused by cluster formation of the SKBR-3 cells. From these 106 nuclei, chromosome copy numbers were enumerated in 99 cases, no FISH signals were detected in 4 nuclei and the nuclei of 3 cells were no longer present. As these cells were present before the hybridization procedure they are most likely washed away during the FISH preparation, leaving a “hole” in the ferrofluids which is visible in the bright field images. Figure 3.2.5 shows a histogram with the count of each probe for all the events. The aneuploidy of the SKBR-3 cells is apparent with an average of 3 copies of chromosome X and 4 copies of chromosome 21.

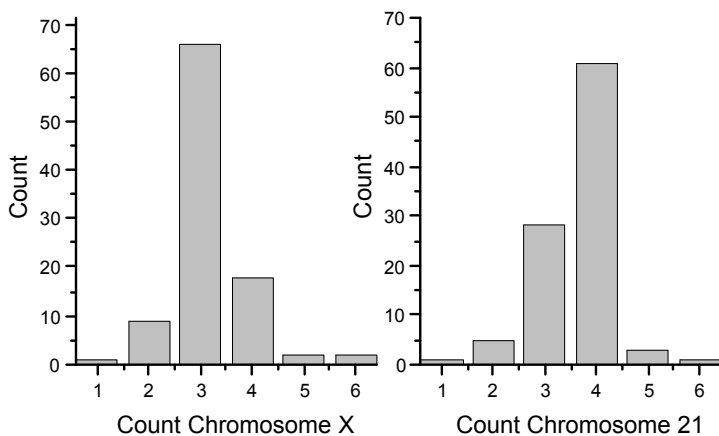


**Figure 3.2.5.** Histograms of the number of FISH signals from chromosome X and 21 in 106 nuclei from SKBR-3 cells.

### **3.2.5 Discussion**

The presence of CTCs in blood is associated with shortened survival of patients with metastatic carcinoma. Accurate identification of tumor cells in blood is therefore of great importance for the management of the disease in these patients. Recently significant improvements have been made in the preparation of blood samples for tumor cell detection as well as in the detection of tumor cells in these samples. Still the heterogeneous appearance of these cells makes assignment of individual events as tumor cells extremely difficult especially when only few

events are detected. The identification of tumor cells in patients with no known cancer is even of greater importance and phenotypic and morphological appearance is not sufficient to assign a single event as a tumor cell. Assessment of aneuploidy, gene amplification, translocation and micro deletions on CTC by FISH can expand the specificity of CTC detection and permits the identification of treatment targets. We have designed and built an automated laser image cytometer "CellTracks TDI" that is capable to detect and reexamine rare events in a consistent and automated manner. Important features of this instrument as compared to other imaging techniques are the data acquisition and the excitation of the fluorophores. The data acquisition of this instrument is operating with a TDI camera. This enables continuous sample scanning, while the line readout of the camera is synchronized with the sample motion. This results in minimal overhead time and prevents unnecessary bleaching of the sample which is not the case for a traditional frame by frame based scanning system.

The excitation of the fluorophores with the CellTracks TDI system is applied with a homogenized laser illumination profile. This gives the possibility to obtain a higher irradiance as compared to a mercury arc lamp which is limited due to a finite size of its arc. For this reason laser excitation has the capability to increase the irradiance rather than increasing integration time to accumulate enough signal to fill the dynamic range of the camera. Besides this advantage, a mercury arc lamp also produces relatively much heat and requires frequent replacement and realignment by an operator. These properties of a mercury arc lamp make it less desirable for an instrument in a clinical setting. However, a clear advantage of a mercury arc lamp is still the flexibility of the excitation range. Several emission peaks are readily available for excitation and this is limited for the CellTracks TDI by the amount of laser lines available in the setup.

The sample chamber which is a closed system can be accessed easily by removing the plug of the sample chamber and the buffer can be replaced without considerable disturbance of the cells. Whereas a unique property of these sample chambers is that the cells remain firmly at the top glass surface of the sample chamber assisted by the magnetic force of the MagNest. This makes multiple relabeling strategies possible with minimal interference of the cellular positions on the top surface of the cartridge. We used the CellTracks TDI system to explore the potential of these capabilities. Specific events are initially detected by a sample scan in TDI mode followed by reexamination prior to and after FISH preparation. The system positions the object at the center of the field of view and a stack of images at multiple focus positions (Z-stack) is obtained. This result showed that reexamination of the events is indeed possible after extensive sample preparations in a consistent manner. During this reexamination the camera is operated in frame transfer mode instead of TDI. This possibility to switch between acquisition modes enables the creation of the Z-stacks. TDI would in this case introduce more

overhead time since an object is positioned within a single field of view of the camera.

The counting of FISH probes in this study was done manually. This should be optimized further and requires a fully automated counting algorithm to minimize the workload of the operator<sup>113</sup>. Besides this it is also desired to assess more probes for FISH and tumor related antigens. This requires a larger set of fluorophores which can be visualized by the system. Regarding the small FISH probes there is a possibility to use ratio labeling<sup>114-115</sup> to maximize the number of probes that can be assessed. Another good alternative to assess more fluorescent probes could be an assay using multiple Qdots in combination with DAPI as a nuclear stain<sup>116-117</sup>. Since the Qdots have relatively small emission spectra, long photo stability and are all excitable in the UV region. These properties have several advantages and may give the possibility to spectrally separate up to 6 or 7 probes and could furthermore simplify the CellTracks TDI to a single UV laser excitation line. On the instrument side this could be implemented quite easily. However, it would first require optimization of the labeling protocols for Qdots CTC labeling. The probes should specifically label each target, with minimal background. Preferably it should be compatible with the current sample preparation.



## **3.3 Qdots as an alternative labeling strategy for Circulating Tumor Cell characterization**

### **3.3.1 Summary**

We designed an image cytometer to enumerate Circulating Tumor Cells (CTCs) in a consistent and automated manner. Typical for the CTC analysis assay the fluorophores DAPI, PE and APC are used and are excited with different lasers. For this study the capabilities of the CellTracks TDI platform are evaluated for Qdots as an alternative labeling strategy for CTCs. Initial experiments were obtained with the use of magnetic beads labeled with 5 different Qdots and showed that they can be resolved clearly. The cross-talk for the different Qdots is below 10%, except for Qdot 585 which was above 20% at 565DF20. Additional labeling experiments with Qdots are obtained with a mixture of the breast cancer cell lines SKBR-3 and MCF-7. Fluorescent labeling of the cells was obtained with Qdot 605, Qdot 655 conjugated with HER2/neu and MUC-1 respectively. The data shows that Qdots are a viable strategy for CTC labeling. However further optimization of the labeling protocols is still needed.

### **3.3.2 Introduction**

In patients with metastatic carcinomas the presence of circulating tumor cells (CTCs) is associated with poor survival prospects.<sup>13-18</sup> Beside enumeration, CTC detection can be exploited to further characterize a CTC and measure the presence or absence of specific treatment targets.<sup>23-25</sup> This can provide the oncologist with the information on the most effective therapy for the individual patient. To obtain expression levels for a large set of treatment targets, it is required for the current instrumentation to assess several fluorescent probes with minimal crosstalk. Therefore Qdots may be an attractive solution. They have narrow emission spectra, long photo stability and are all excitable in the UV region. These properties give the possibility to spectrally separate DAPI and 6 or 7 Qdots. This could simplify and optimize the instrumentation with just a single UV laser excitation line. In this study some initial experiments are shown to evaluate Qdots for use in the CellTracks TDI.

### 3.3.3 Materials and methods

#### *Bead labeling*

To obtain a bead mixture with 5 differently labeled beads, 5 different Qdots were labeled separately. 10 $\mu$ l of magnetic biotinylated beads (Spherotech, Lake Forest, IL) are diluted in 500  $\mu$ l PBS and centrifuged at 6,000 rpm for 3 min. Aspirated and resuspended in 550  $\mu$ l PBS. For labelling, five stock vials of Qdot nanocrystals streptavidin conjugates 565, 585, 605, 655 and 705 (Invitrogen) were used. From each Qdot vial 2 $\mu$ l was added to 100 $\mu$ l of the resuspended beads. These mixtures were incubated for 20 minutes and centrifuged at 6,000 rpm for 3 min and washed with PBS and resuspended in 100  $\mu$ l PBS. 10  $\mu$ l of each Qdot-labeled bead suspension were mixed and diluted in 280  $\mu$ l PBS. The Qdot-labeled bead mixture was transferred into the analysis cartridge and placed in the MagNest.

#### *Cell Spiking*

Cells from two breast cancer cell lines SKBR-3 and MCF-7 (ATCC, Middlesex, UK) were both cultured in RPMI 1640 Glutamax-I medium (Invitrogen, Carlsbad, CA). Cells were harvested and spiked into a 100 $\mu$ l buffer solution containing ~ 5,000 SKBR-3 and MCF-7 cells. The mixture was centrifuged at 1,200 rpm for 5 min and washed with PBS and resuspended in 100  $\mu$ l PBS.

#### *Qdot labeling of MCF-7 and SKBR-3 cells*

The spiked SKBR-3 and MCF-7 samples are incubated for 20 min with 10  $\mu$ l of Epithelial Cell Adhesion Molecule (EpCAM) labeled ferrofluids to immunomagnetically label the cells. EpCAM is specific for cells of epithelial origin. The cells are permeabilized by addition of 20 $\mu$ l Immuniperm for 10 min. The sample is stained with the nuclear acid dye DAPI (10 $\mu$ l) and two specific tumor targets (3 $\mu$ l) HER2/neu-Qdot 605 and (3 $\mu$ l) MUC-1-Qdot 655 conjugates. These conjugates were prepared with a Qdot Antibody Conjugation Kit (Invitrogen). This mixture was incubated for 45 min, centrifuged at 1,200 rpm for 5 min and washed with PBS and resuspended in 330  $\mu$ l PBS. After incubation and washing the sample is transferred into the analysis cartridge and placed in the MagNest(Immunicon). The device presents the magnetically labeled cells at the upper surface of the sample cartridge.

#### *Imaging by CellTracks TDI*

The samples are analyzed with the CellTracks TDI system. This is a fully automated scanning system. It uses a 40x NA 0.6 microscope objective (Nikon, Tokyo, Japan) and is equipped with 3 lasers (375nm, 532nm, 639nm). These are coupled in with a 400-535-635TBDR triple dichroic mirror Omega

Optical Inc. Brattleboro, VT). A blue LED positioned below the MagNest is used as a light source to obtain a bright field image. With this system the images are acquired with a 12-bit TDI camera (Hamamatsu, Hamamatsu city, Japan). Before the fluorescent light is detected by the camera the light passes through a motorized filter wheel (Thorlabs, Newton, NJ) to select the proper emission band pass filter for each probe. For the Qdots 5 different filters are used 565DF20, 585DF20, 605DF20, 655DF20 and 710AF40 (Omega Optical Inc). For DAPI and brightfield images are obtained with a 450DF65 emission filter. With these settings for excitation of DAPI and the Qdots only the 16 mW 375-nm laser diode (Power Technologies, Little Rock, AR) is used.

### 3.3.4 Results

#### *Qdot Crosstalk*

The Qdot bead mixture labelled with 5 different Qdots is scanned 6 times with a scan speed of 1 mm/s corresponding with an average integration time of 204.8 ms. Figure 3.3.1 shows 6 panels of a single frame with the corresponding images for Brightfield, Qdot 565, Qdot 585, Qdot 605, Qdot 655 and Qdot 705.

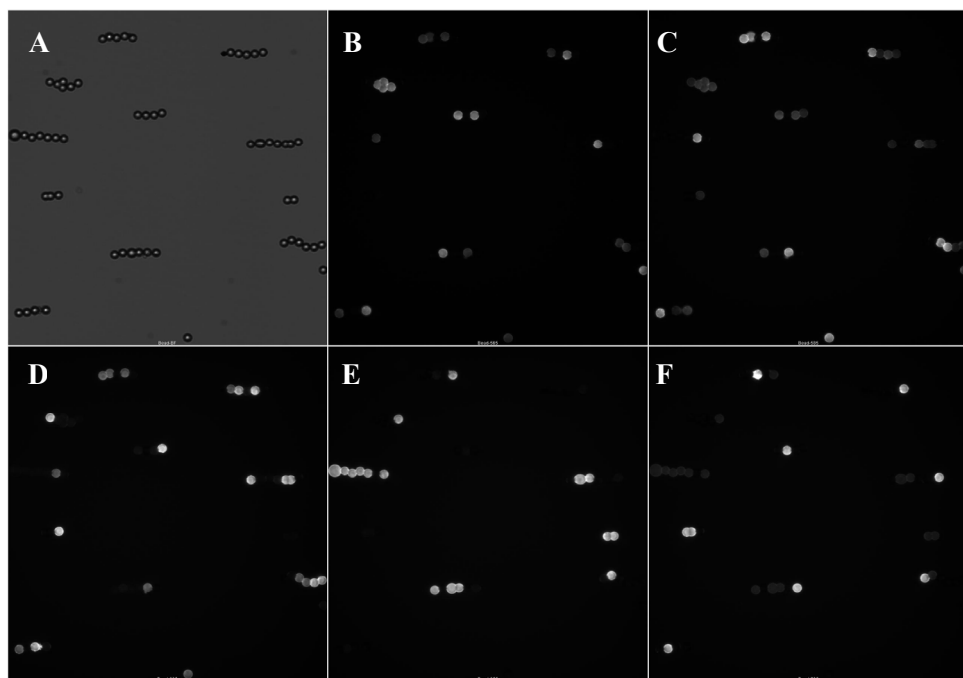


**Figure 3.3.1** 6 Separate images of Qdot labeled magnetic biotinylated beads obtained with the CellTracks TDI. Respectively for brightfield and 5 different Qdots (565, 585, 605, 655, 705)

The images in the figure 3.3.1 indicate there is some spectral overlap between the Qdots emission spectra. Although emission spectra are narrow, they are positioned relatively close to each other. The amount of overlap is shown in figure 3.3.2a and is determined by the contribution of the emission visible in the 5 images for the different bead populations. Since the bead population have been labeled and washed separately, each bead contained only 1 type of Qdot. From the figure it is clear that Qdot 585 has the most significant spectral overlap. This crosstalk can be compensated by spectral un-mixing<sup>118-120</sup> as is illustrated in figure 3.3.2b. The figure shows the 5 spectrally unmixed populations of beads. Spectral un-mixing with Qdots has the advantage that the Qdots are photo stable and the excitation is at a single wavelength, therefore the illumination profile is constant for all Qdots.

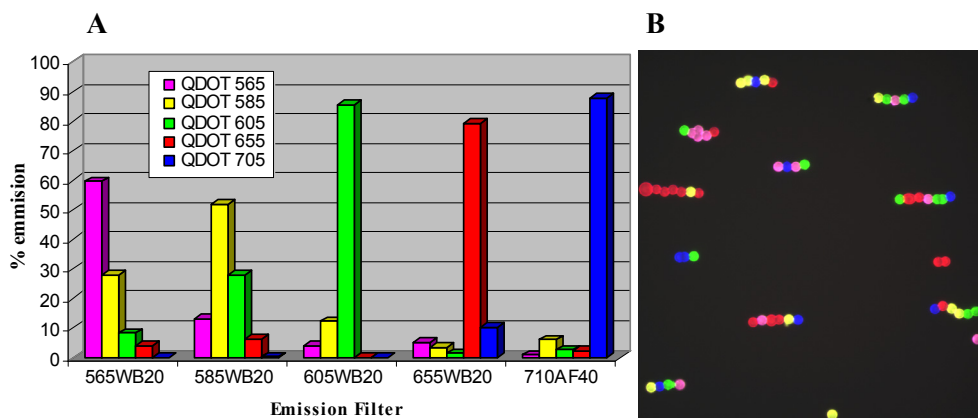


**Figure 3.3.2** Crosstalk of the fluorescent emission for Qdot (565,585,605,655 and 705) using 375nm UV excitation. Each Qdot is separated with a different band pass emission filters 565DF20, 585DF20, 605DF20, 655DF20 and 710AF40. (Omega Optical Inc). The right panel shows a color overlay of the 5 differently labeled beads after spectral un-mixing.

It is known that Qdots are very photo stable and have a large absorption cross section<sup>101</sup> that strongly increases in the UV region. (table 3.3.1). Therefore the intensity of the Qdot labeled beads, proved to be very high and required reduction of the laser power up to 25% of the 16mw 375 nm laser to prevent saturation of the camera. However an absolute quantification in terms of photons/Qdot has not been obtained since the quantity of Qdots on the beads was not known.

	Molar extinction coefficient M-1cm-1		
	@350 nm	@375 nm	@405 nm
Qdot 565	1,900,000	1,500,000	1,100,000
Qdot 585	3,500,000	2,850,000	2,200,000
Qdot 605	4,400,000	3,600,000	2,800,000
Qdot 655	9,100,000	7,400,000	5,700,000
Qdot 705	12,900,000	10,600,000	8,300,000

**Table 3.3.1** Molar absorption coefficient qdots (Invitrogen, CdSe/ZnS core-shell) Quantum yields are 30-50% and have a lifetime of ~ 20-40 ns.<sup>101</sup>

### *Qdot labeling of cells*

In the previous paragraph we showed that multiple Qdots can be detected and distinguished clearly with a direct imaging method using narrow bandpass filters. The properties such as (Brightness, photo stability, narrow emission bands and single UV excitation) show that they are ideal for an image cytometer. It gives the possibility to simplify the instrumentation further and measure with a high sensitivity. Despite all these good aspects on the instrument side, it is also very important that the Qdots can be used to specifically label a cellular target with a minimal amount of background. Furthermore when labeling cells with Qdots, it is also desired to keep the number of washing steps to a minimum. This is important for labeling circulating tumor cells to prevent additional cell loss. To this end we carried out several measurements and conjugated Qdot 605 and Qdot 655 with the antibodies HER2/neu and MUC-1 respectively. Direct conjugation of the antibodies with the Qdots is preferred to prevent additional washing steps when labeling multiple cellular targets.

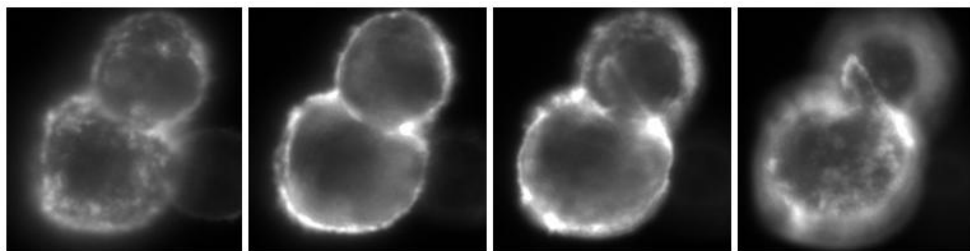


**Figure 3.3.3** Two SKBR-3 cells labeled with Qdot 605 - HER2/neu and imaged with the CellTracks TDI. Distance between z-stacks is 4 micron (integration time 30ms each) (Image scale 40x40 $\mu\text{m}^2$ )

From the first labeling experiments of SKBR-3 cells of Qdot 605 conjugated with HER2/neu a strong fluorescent emission of the Qdots was visible. At full laser power integration times of only 30-50ms were required, were a further increase of integration already resulted in the saturation of the camera. Although it should be

noted, that SKBR-3 cells do have a very strong HER2/neu expression with approximately 1.1 million binding sites.<sup>121</sup> Furthermore the fluorescence signal showed a minimal amount of bleaching and could be illuminated for several minutes without a decrease in signal. For a more detailed characterization, the CTC will be exposed longer to the illumination light. Therefore Qdots are preferred above fluorophores that bleach.

Additional experiments have been carried out with a mixture of SKBR-3 and MCF-7 cells labeled with Qdot 605 - HER2/neu and Qdot 655 - MUC-1. Figure 3.3.4 shows that the SKBR-3 cells (left panel) are staining with HER2/neu but not with MUC-1, whereas the MCF-7 cells (right panel) are staining with MUC-1 but not with HER2/neu. This expression is expected for these cell lines.<sup>122</sup> This indicates that Qdot labeling is indeed specific. Furthermore it is also visible that the strong DAPI signal also excited at 375 nm is still visible at 605 nm due to long tail in its emission spectra. Staining in the Qdot 605 HER2/neu channel (Right panel figure 3.3.4) is due to DAPI not HER2/neu. Note the same shape of the object in the DAPI and Qdot 605 channel.

The initial experiments showed good results, however it also showed some aggregation of the Qdots. Furthermore the Qdot conjugates deteriorated within a few days due to this aggregation.

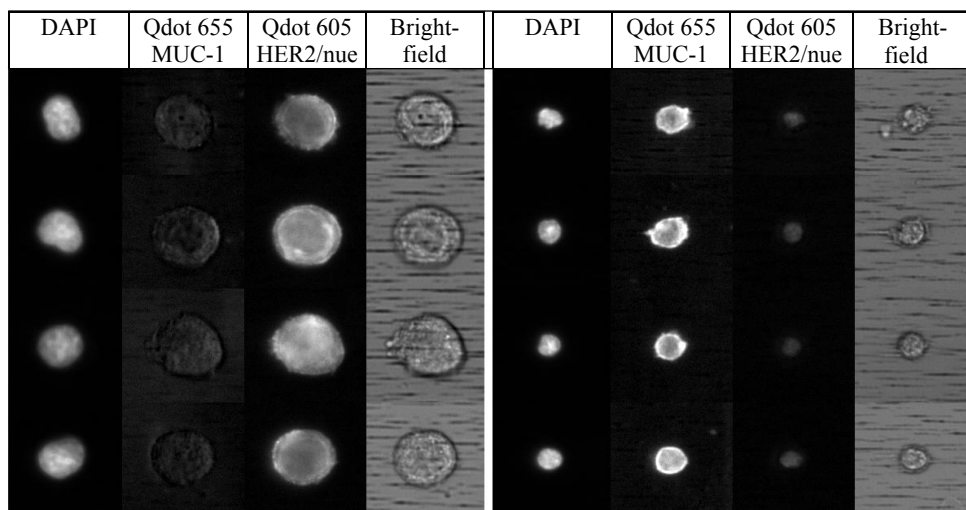


**Figure 3.3.4** Fluorescent images obtained with the CellTracks TDI. The left panel shows 4 relatively large HER2/neu positive and MUC-1 negative SKBR-3 cells. The right side panel shows 4 HER2/neu negative and MUC-1 positive MCF-7 cells. (Image scale 30x30 $\mu\text{m}^2$ )

Therefore the Qdots labeling became less efficient and showed severe aggregated clumps in the sample as shown in figure 3.3.5.

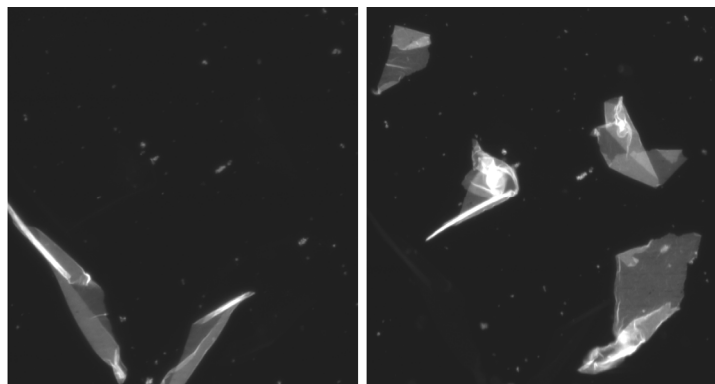


**Figure 3.3.5** Qdot aggregation for HER2/neu and MUC-1 conjugates.

### 3.3.5 Discussion

The enumeration of CTCs can be used to monitor disease progression of metastatic carcinoma patients. Beside enumeration of CTCs, it is desired to further characterize these tumor cells. This could be used to quantify the expression of several receptors related to specific therapies. To determine the expression of a broad range of tumor related receptors, it is necessary for the current instrumentation to distinguish and quantify a large set of specifically tagged fluorescent labels.

Therefore we tested the CellTracks TDI for its applicability of Qdots to quantify a broad range of receptors. Qdots provide the possibility to distinguish 6 or even more probes with minimal spectral overlap due to the relatively narrow and closely spaced emission spectra. Moreover, Qdots have the advantage that they are photo stable, have a large absorption cross section and large stokes shift. This enables long exposure times, sensitive detection and could further simplify the instrumentation to a single UV excitation source.

Initial experiments were obtained with Qdot labeled beads (figure 3.3.1 and 3.3.2) and showed that five different Qdots with a spectral distance of  $\sim 35\text{nm}$  can be spectrally resolved with the CellTracks TDI. Furthermore extension with more than 5 Qdots can be applied relatively simply and is not directly limited by the instrumentation.

Although strong fluorescent signals and spectral separation can be obtained the method is only viable if the labeling is specific. CTC detection and characterization requires specific labeling of each target with a minimum of background. Furthermore cell loss should be prevented and therefore a labeling procedure

should be developed with a minimal amount of washing steps, and preferably compatible with the current methodology. We tested the specificity of Qdot labeling using two breast cancer cell lines with different expression for HER2/neu and MUC-1. These measurements show that specific labeling of surface markers is possible and result in a strong fluorescent signal. However to fully exploit the Qdots and make use of multiple labels it requires further testing of multiple surface markers and also exploring the feasibility of labeling of intracellular objects.

Despite the good results, the initial experiments also showed that aggregation of the Qdots took place in the labeled samples and Qdot conjugates (figure 3.3.5). This resulted in deterioration of the sample, and labeling with Qdot conjugates became less effective after a few days. The use of Qdots therefore still requires further optimization of the labeling procedure to prevent aggregation and obtain reliable and consistent labeling of the samples. Nevertheless, the first Qdot experiments look promising, and could be a viable method to detect, and specifically label a large set of targets with high sensitivity and specificity.

Beside Qdot labeling the cell nuclei were labeled with DAPI. This dye has a relatively long emission tail and peak absorbance at 360 nm. This resulted in some crosstalk with Qdot 605 as shown figure 3.3.4 and will even interfere more with Qdots below 605. This cross-talk is induced since both DAPI and all Qdots are excited simultaneously in the UV region. This could be prevented using a 405 nm laser for Qdot excitation to avoid excessive DAPI cross-talk. Fortunately the cross-talk between the Qdots is limited due to the narrow emission spectra as shown in figure 3.3.2 and gives the possibility to spectrally separate a large set of Qdots. With the currently commercially available Qdots (525, 565, 585, 605, 705, 800) it could bring the setup up to 7 fluorophores including DAPI. Further extension of the number of probes would be possible with additional Qdots. Since Qdots can be tuned for a specific emission wavelength, which can go up from ~450 to 1900 nm. However the number of probes is ultimately limited by the amount of spectral overlap which can be accepted. Furthermore it also depends on the quantum efficiency of the detector, for the CellTracks TDI detection efficiency already drops below 0 at 1000nm. When minimal cross-talk below 10 % is desired it would require a spacing of ~40/50 nm between the Qdots. Therefore this would result in approximately 9-10 Qdots that can be used simultaneously in the CellTracks TDI. Furthermore when a large set of closely spaced Qdots is used it is required to correct the image data with a spectral un-mixing algorithm to obtain reliable quantitative information. In contrast no spectral un-mixing is needed with the current fluorophores DAPI, PE and APC as the emission spectra are well separated and each excited at a different wavelength. However addition of more traditional fluorophores will considerably increase the cross-talk. Another possibility is to maintain the current CTC assay using DAPI, PE and APC and add the Qdots as additional probes.



# Conclusions and outlook

## 4.1 Conclusions

### *CellTracks TDI*

We designed an image cytometer to enumerate Circulating Tumor Cells (CTCs) in a consistent and automated manner. This new instrument, the “CellTracks TDI” presented in this thesis is specifically designed to improve enumeration and characterization of Circulating Tumor Cells (CTCs) by increasing resolution, sensitivity and minimizing acquisition time. We showed that image acquisition with a TDI camera in continuous motion is a beneficial method to acquire image data for a large surface to minimize acquisition time.

The use of laser excitation as an ultra bright light source in combination with beam homogenizing optics also show to be a viable alternative to the Mercury Arc lamp used in the CellTracks II analyzer. Instead of adapting integration times of the camera to the illumination intensity bright laser excitation makes it possible to set the illumination intensity to the desired integration time. The fast switching and power adjustment properties, brightness, wavelength specificity, emission stability, minimal heat output and long life span make quantitative analysis more reliable and a preferred excitation source for an image cytometer in a clinical setting.

### *Automated scanning and image analysis*

An important aspect of an image cytometer is automation. Software has been written for automated scanning of a sample and several algorithms and procedures were developed to consistently obtain focus positions and sample borders. Besides data acquisition, an image analysis program was written. The large set of image data is processed automatically to extract and visualize useful information to an operator. Scatter plots together with images provides the operator simultaneously with quantitative and morphological parameters. A major advantage of this approach is the reduction of inter-reader variability and it permits the classification of CTCs and tumor cell derived microparticles without overloading visual inspection by an operator. CTC detection in the CellTracks analyzer II, relies completely on the final selection by an operator on a set of pre selected events. Difficulties arise for an operator to deduce quantitative information from the images that are auto scaled. Further improvements of the current analysis method could be obtained by means of multi parameter analysis of the measurement data. This could enhance the automated classification without manual inspection by an operator.

### ***CTC characterization***

The capabilities of the CellTracks TDI were compared with the commercial available CellTracks Analyzer II. Blood samples of 26 metastatic cancer patients were tested on both systems. The results showed a large heterogeneity in the morphology of CTC within and between patients. A side by side comparison showed a good correlation between intact CTC classified by both systems. The higher resolution and bright field images of the CellTracks TDI images provided additional information that permitted a better identification that for example allowed visualization of typical apoptotic features in the cells. With the quantitative analysis three populations of CTC were identified and a clear relation between the presence of CTC and CTC related debris was established. CTC debris was a factor 14 higher and patients without intact CTC showed a minimal amount of CTC related debris. This suggests that it might be very useful to enumerate these tumor cell derive micro particles. This could be a very useful tool to reduce false positive selection of a CTC sample. Furthermore it could be a better indicator in an earlier stage of the disease to set a lower threshold. However the same problem remains, CTC detection is inherently limited due to its low frequency and detection is ultimately limited by the amount of blood that can be drawn from a patient.

### ***Reexamination***

We showed that the CellTracks TDI is capable of revisiting specific events. This permits further examination of a specific event of interest and gives the possibility to further characterize a CTC. To evaluate this capability we labeled chromosomes with FISH probes that allowed detection of abnormal chromosome copy number in a CTC and confirm that the cell is indeed cancerous. Since the cells remained at their initial position even after extensive sample preparations by hybridization of the sample with FISH probes. However, the copy number of FISH probes for these cells was manually counted and the process should be automated as the manual counting is a labor intensive procedure.

## **4.2 Outlook**

### ***Illumination***

In the current setting we used multiple laser lines as excitation source. Beside laser excitation LED technology will be a good and inexpensive alternative as an excitation source in the near future. Although the light power is still limited technological advances will result in LEDs with a higher radiance. These advances will lead to the next generation of excitation sources for fluorescent microscopy and replace the mercury arc lamp as the preferred excitation source.

## ***Ferrofluid***

For immunomagnetic enrichment of the sample, ferrofluid is used and a large portion of the ferrofluid is not bound to the cells and remains in the sample. This has a severe drawback. The ferrofluid is partly blocking cells and interferes with the fluorescent signals. This makes quantitative analysis less reliable and image detail is partly lost as shown in chapter 2.3. The brightfield images are also severely degraded due to the ferrofluid content. These brightfield images could be very useful as an additional morphological parameter, unfortunately most of the detail is completely lost. Therefore it would be a great improvement of the current CTC assay when excessive ferrofluid content would be reduced. This will result in less noise, an increase of signal and accuracy and improve CTC enumeration and characterization. However care should be taken in ferrofluid removal since additional cell loss is not acceptable.

## ***Alignment structures***

As already mentioned in the introduction we already are working in our group on structures to guide the cells into a designated area. This structure should align the cells but not obstruct the light path. This led to the design of several types of V-groove PDMS structures. These structures mechanically align the cells and effectively reduce the total surface area. This has several advantages; it concentrates the cells and reduces the required scan time and prevents additional stitching of the images. Furthermore it limits the cellular objects to a small part of the homogeneous excitation profile. Due to the reduced area only a small stroke of the camera is used for detection. The remaining part of the camera could be used to simultaneously image a second stroke on the camera of an additional fluorescent channel. Although alignment is beneficial it also amplifies the problem of the ferrofluid interfering with the CTC detection. The ferrofluid is concentrated further and results in an increased blockage of the fluorescent signal. This points out again that it would be very useful to reduce excessive ferrofluid content.

## ***Parallel Multi Color Setup***

The current setup uses a single TDI camera and each channel is measured one after another. For the CellTracks TDI only a small part of the detection range is blocked due to small excitation bands of the used laser excitation. This could be exploited by splitting the fluorescent signal with dichroic mirrors and scanning the sample with multiple cameras simultaneously. Currently the acquisition software is modified to acquire image data of 3 cameras simultaneously and requires further implementation in the optical setup. This would further reduce total acquisition time. Yet excitation and detection of multiple fluorophores simultaneously also results in an increase of cross-talk. Beside this, multiple cameras considerably increases instrument cost.

### ***Dynamic focusing***

Focus is currently adjusted in feed forward and focus positions are determined prior to a sample scan. Preferably focus is obtained dynamically and adjusted continuously. This prevents additional time for pre focusing and is more accurate for local variations of the focus position. It would be very useful for the (PDMS) groove structure as these structures are less rigid and straight as a glass surface used for the current sample chambers.

### ***Multi probe fluorescent assay***

In the current setting we used 3 fluorophores. However detection of additional fluorophores is desired. These could be used to identify specific therapy targets on a CTC. With the three laser lines in the setup several traditional dyes and tandem dyes can be excited and expand the number of probes. However, most of these dyes have a broad emission spectrum and a relatively small stokes shift, addition of multiple dyes in the assay will inevitably lead to an increase of cross-talk.

Alternative to the traditional dyes we showed some of the first results with Qdots with the CellTracks TDI. Qdots have relatively narrow emission spectra, low bleaching rates and large stokes shifts. This gives the possibility to simplify the setup to a single UV excitation line and separate each QDOT with separate band pass filters. In the first experiments we showed the fluorescent labeling of beads with 5 different Qdots these could be separated and detected clearly with the instrument. To obtain results with cells we conjugated HER-2 and MUC-1 with Qdot 605 and Qdot 655 respectively. Although the cells were labeled specifically and showed a strong fluorescent signal there was still a large portion of debris due to aggregation of the Qdots. Use of the Qdots for the current CTC assay can be an attractive alternative it however requires further optimization of the labeling protocol.

### ***Cell removal***

With the current instrument we are able to identify, reexamine a specific event by means of a fluorescent image and capable of relabeling the CTC with FISH probes. Beside reexamination and relabeling inside the chamber it would be interesting to remove the cell of interest out of the analysis chamber. This could give the capability to further characterize a CTC by examining their potential to grow, analyze the DNA and RNA content with different analytical techniques such as a PCR array based approach.

# References

1. Engell HC. Cancer cells in the circulating blood; a clinical study on the occurrence of cancer cells in the peripheral blood and in venous blood draining the tumour area at operation. *Acta Chir Scand Suppl* 1955; 201:1-70.
2. Terstappen LWMM, Rao C, Gross S, Weiss A. Peripheral blood tumor cell load reflects the clinical activity of the disease in patients with carcinoma of the breast. *International Journal of Oncology* 2000;17: 573-578
3. Recamier JCA. L'histoire de le Meme Maladie. Gabor; vol, p 110, 1829.
4. Ashworth TR. A case of cancer in which cells similar to those in the tumours were seen in the blood after death. *Australian Med J* 1869;14:146-147.
5. Mocellin S, Ulrich Keilholz U, Carlo Riccardo Rossi CR, Nitti D. Circulating tumor cells: the 'leukemicphase' of solid cancers *TRENDS in Molecular Medicine* 2006;12:3
6. Pantel K, Cote RJ,Fodstad O.Detection and Clinical Importance of Micrometastatic Disease.*Journal of the National Cancer Institute* 1999;91:13.
7. Müller V, Daniel F Hayes DF, Pantel K.Recent translational research: circulating tumor cells in breast cancer patients. *Breast Cancer Research* 2006;8:110.
8. Pantel K, Brakenhoff RH. Dissecting the metastatic cascade.*Nat Rev Cancer* 2004; 4:448-456.
9. Smerage JB, Hayes DF.The measurement and therapeutic implications of circulating tumour cells in breast cancer. *British Journal of Cancer* 2006; 94:8-12.
10. Ring A, Smith IE, Dowsett M.Lancet. Circulating tumour cells in breast cancer.*Oncol* 2004;5: 79-88
11. Paterlini P, Benali NL.Circulating tumor cells (CTC) detection: Clinical impact and future directions. *Cancer Letters* 2007;253:180-204
12. Fidler IJ. The pathogenesis of cancer metastasis: the 'seed and soil' hypothesis revisited. *Nat. Rev. Cancer* 2003; 3: 453-458.
13. Cristofanilli M, Budd GT, Ellis MJ, Stopeck A, Matera J, Miller MC, Rueben JM Doyle G, Allard WJ, Terstappen LWMM, Hayes DF. Circulating Tumor Cells, Disease Progression and Survival in Metastatic Breast Cancer. *NEJM* 2004; 351: 781-791.
14. Hayes DF, Cristofanilli M, Budd GT, Ellis MJ, Stopeck A, Miller MC, Matera J, Allard WJ , Doyle GV, Terstappen LWMM. Circulating tumor cells predict progression free and overall survival at each follow-up time point during therapy of metastatic breast cancer patients. *Clin Can Res* 2006; 12:4218-4224.
15. Moreno JG, O'Hara MS, Gross S, Doyle G, Fritsche H, Gomella LG, Terstappen LWMM. Changes in circulating carcinoma cells in patients with metastatic prostate cancer correlate with disease status, *Urology* 2001; 58:386-392.
16. Moreno JG, Miller MC, Gross S, Allard WJ, Gomella LG, Terstappen LWMM. Circulating tumor cells predict survival in patients with metastatic prostate cancer. *Urology* 2005; 65: 713-718.
17. Budd G, Cristofanilli M, Ellis M, Stopeck A, Borden E, Miller MC, Matera J, Repollet M, Doyle G, Terstappen LWMM, Hayes D. Circulating Tumor Cells versus Imaging - Predicting Overall Survival in Metastatic Breast Cancer. *Clin Can Res* 2006;12: 6404-6409.
18. Cristofanilli M, Hayes DF, Budd GT, Ellis MJ, Stopeck AT, Doyle GV, Matera J, Allard WJ, Miller MC, Rueben JM, Fritsche HA, Hortobagyi GN, Terstappen LWMM. Circulating Tumor Cells: A Novel Prognostic Factor for Newly Diagnosed Metastatic Breast Cancer. *JCO* 2005; 23:1420-1430.
19. Larson CJ, Moreno JG, Pienta KJ, Gross S, Repollet M, O'Hara SM, Russell T, Terstappen LWMM. Apoptosis of Circulating Tumor Cells in Prostate Cancer Patients. *Cytometry* 2004; 62A: 46-53.
20. Mehes G, Armin Witt A,† Ernst Kubista E, AmbrosAF. Circulating Breast Cancer Cells Are Frequently Apoptotic. *AJP* 2001; 15:1.

21. Mocellini S, Fiore del P, guarnieri L, Scalerta R, Foletto M, Chiarion V, PILATI P, Nitti D, Lise M, Rossi CR. Molecular Detection of circulating tumor cells is an independent prognostic factor in patients with high-risk cutaneous melanoma. *Int. J. Cancer* 2004; 111:741-745.
22. Marrinucci D, Bethel K, Bruce RH, Curry DN, Hsieh B, Humphrey M, Krivacic RT, Kroener J, Kroener L, Ladanyi A, Lazarus NH, Nieva J, Kuhn P. Case study of the morphologic variation of circulating tumor cells. *Human Pathology* 2007; 38:514-519
23. Hayes DF, Walker TM, Singh B, Vitetta E S, Uhr JW, Gross S, Rao C, Doyle GV and Terstappen LWMM. Monitoring Expression of HER-2 on Circulating Epithelial Cells in Patients with advanced Breast Cancer. *Int J of Oncology* 2002; 21: 1111-1118.
24. Meng S, Tripathy D, Frenkel EP, Shete S, Ashfaq R, Saboorian H, Haley B, Frenkel E, Euhus D, Leitch M, Osborne C, Clifford E, Perkins S, Beitsch P, Kahn A, Morrison L, Herylyn D, Terstappen LWMM, Lane N, Wang J, Uhr JW. uPar and Her-2 gene status in individual breast cancer cells from blood and tissues. *PNAS* 2006; 103: 17361-17365.
25. Meng S, Tripathy D, Shete S, Ashfaq R, Haley B, Perkins S, Beitsch P, Khan A, Euhus D, Osborne C, Frenkel E, Hoover S, Leitch M, Clifford E, Morrison L, Herlyn D, Terstappen LWMM, Fleming T, Fehm T, Tucker T, Lane N, Wang J, Uhr J. HER-2 Gene Amplification can be acquired as breast cancer progresses. *PNAS* 2004; 101: 9393-9398.
26. Fehm T, Sagalowsky A, Clifford E, Beitsch P, Saboorian H, Euhus D, Meng S, Morrison L, Tucker T, Lane N, Ghadimi BM, Heselmeyer-Haddad K, Ried T, Rao C, Uhr J. Cytogenetic evidence that circulating epithelial cells in patients with carcinoma are malignant, *Clinical Cancer Research* 2002; 8:2073-2084.
27. Tibbe AGJ, Swennenhuis JF, Terstappen LWMM. Detection of cytogenetic aberrations in circulating tumor cells. *Proc Annu Meet Am Assoc Cancer Res* 2006; 47: A3624.
28. Shapiro HM. *Practical Flow Cytometry*. Third edition 1995, Wiley-Liss, New York. ISBN 0471303763.
29. Agronsskaia. Identification of DNA fragments by two parameter flow cytometry. PhD Thesis 1999 University of Twente, ISBN 9036513014.
30. Gross HJ, Verwer B, Houck D, Hoffman RA, Recktenwald D. Model study detecting breast cancer cells in peripheral blood mononuclear cells at frequencies as low as 10<sup>-7</sup> *Proc. Natl. Acad. Sci. USA* 1995; 92:537-541.
31. Racila E, Euhus D, Weiss AJ, Rao C, McConnell J, Terstappen LWMM, Uhr JW. Detection and characterization of carcinoma cells in the blood. *PNAS* 1998; 95: 4589-4594.
32. Ortyu WE, Basiji DA. Imaging and analyzing parameters of small moving objects. USA patent 6249341. 2001.
33. Hesse J, Sonnleitner M, Sonnleitner A, Freudenthaler G, Jacak J, Jlinger OH, Schindler H, Schu1 GJ. Single-Molecule Reader for High-Throughput Bioanalysis. *Anal. Chem.* 2004; 76:5960-5964.
34. Bocsi J, Varga VS, Molnar B, Sipos F, Tulassay Z, Tarnok A. Scanning Fluorescent Microscopy Analysis Is Applicable for Absolute and Relative Cell Frequency Determinations. *Cytometry* 2004; 61A:1-8.
35. Mesker WE, Vrolijk H, Sloos WCR, Tollenaar RAEM, Tanke HJ. Detection of tumor cells in bone marrow, peripheral blood and lymph nodes by automated imaging devices. *Cellular Oncology* 2006; 28:141-150.
36. Borgen EE, Naume B, Nesland JM, Nowels KW, Pavlak N, Ravkin I, Goldbard S. Use of Automated Microscopy for the Detection of Disseminated Tumor Cells in Bone Marrow Samples. *Cytometry (Communications in Clinical Cytometry)* 2001; 46:215-221.
37. Becker SS, Becker-Pergola G, Fehm T, Emig R, Wallwiener D, Solomayer EF. Image Analysis Systems for the Detection of Disseminated Breast Cancer Cells on Bone-Marrow Cytospins. *Journal of Clinical Laboratory Analysis* 2005; 19:115-119.
38. Allard WJ, Matera J, Miller MC, Repollet M, Connelly MC, Rao C, Tibbe A, Uhr JW, Terstappen LWMM. Tumor cells circulate in the peripheral blood of all major carcinomas but not in healthy subjects or patients with non-malignant diseases. *Clin Can Res* 2004; 10: 6897-6904.
39. Rosenberg R, Gertler R, Friederichs J, Fuehrer K, Dahm M, Phelps R, Thorban S, Nekarda H, Siewert JR. Comparison of two density gradient centrifugation systems for the enrichment of disseminated tumor cells in blood. *Cytometry* 2002; 49:150-158.

40. Vona G, Sabile A, Louha M, Sitruk V, Romana S, Schutze K, Capron F, Franco D, Pazzagli M, Vekemans M, Lacour B, Brechot C, Paterlini P. Isolation by Size of Epithelial Tumor Cells *AJP* January 2000; 156:1.
41. Hsieh HB, Marrinucci D, Bethel K, Curry DN, Humphrey M, Krivacic RT, Kroener J, Kroener L, Ladanyi A, Lazarus N, Kuhn P, Bruce RH, Nieva J. High speed detection of circulating tumor cells, *Biosensors and Bioelectronics* 2006; 21:1893–1899.
42. Kraeft SK, Ladanyi A, Galiger K, Herlitz A, Sher AC, Bergsrud DE, Even G, Brunelle S, Harris L, Salgia R, Dahl T, Kesterson J, Chen LB. Reliable and Sensitive Identification of Occult Tumor Cells Using the Improved Rare Event Imaging System. *Clinical Cancer Research* 2004; 10:3020–3028.
43. Krivacic RT, Ladanyi A, Curry DN, Hsieh HB, Kuhn P, Bergsrud DE, Kepros JF, Barbera T, Ho MY, Chen LB, Lerner RA, Bruce RH. A rare-cell detector for cancer. *Proc. Natl. Acad. Sci. U.S.A.* 2004; 101:10501–10504.
44. Kagan M, Howard D, Bendele T, Mayes J, Silvia J, Repollet M, Doyle J, Allard J, Tu N, Bui T, Russell T, Rao C, Hermann M, Rutner H, Terstappen LWMM. A Sample Preparation and Analysis System for Identification of Circulating Tumor Cells. *J Clinical Ligand Assay* 2002; 25: 104-110.
45. Kagan M, Howard D, Bendele T, Rao C, Terstappen LWMM. Circulating Tumor Cells as Cancer Markers, A Sample Preparation and Analysis System, In *Tumor Markers: Physiology, Pathobiology, technology and Clinical Applications*, eds Diamandis E P, Fritsche HA, Lilja H, Chan DW, Schwartz M. AACCPress, Washington 2002; pp 495-498.
46. Rao CG, Chianese D, Doyle GV, Miller MC, Russell T, Sanders RA, Terstappen LWMM. Expression of epithelial cell adhesion molecule in carcinoma cells present in blood and primary and metastatic tumors. *Int. J. Oncology* 2005; 27: 49-58.
47. Liberi PA, Rao CG, Terstappen LWMM. Optimization of ferrofluids and protocols for the enrichment of breast tumor cells in blood. *J Magnetism and Magnetic Materials* 2001; 225: 301-307.
48. Molecular Probes. Excitation and emission spectra, <http://www.probes.com>.
49. Tibbe AGJ, de Grooth B, Greve J, Liberti PA, Dolan GJ, Terstappen LWMM. Optical tracking and detection of immunomagnetically selected and aligned cells. *Nature Biotechnology* 1999; 17:1210-1213.
50. Tibbe AGJ. Cell Tracks: The next step in cell analysis. PhD Thesis 2001 University of Twente, ISBN 9036515416.
51. Schreuder F. Time Delay Integration (TDI) Imaging with Cell Tracks. Master Thesis 2003, University of Twente.
52. Schreuder F, Greve J, Terstappen LWMM, TibbeAGJ. Devices and methodes to image objects by time delay integration. USA patent 2004 PCT/US2004/025981.
53. Grooth de BG, Geerken TH, Greve J. The Cytodisk: A cytometer based upon a new principle of cell alignment. *Cytometry* 1985; 6: 226-233.
54. Scholtens T. Technical aspects of aligning and analyzing rare cells in blood. Master Thesis 2004, University of Twente.
55. Engh van den G, Farmer C. Photo-Bleaching and Photon Saturation in Flow Cytometry. *Cytometry* 1992; 13:669-677.
56. He J, Hu Y, Jiang L. Photodynamic action of phycobiliproteins: in situ generation of reactive oxygen species. *Biochimica et Biophysica Acta* 1997; 1320:165–174.
57. White JC, Stryer L. Photostability Studies of Phycobiliprotein Fluorescent Labels. *Analytical biochemistry* 1987; 161:442-452.
58. Hirai T, Fuse K, Kurisu K, Ebata K. Development of Diffractive Beam Homogenizer. *SEI Technical review* 2005; 60:6.
59. Kopp C, Ravel L, Meyrueis P. Efficient beamshaper homogenizer design combining diffractive optical elements, microlens array and random phase plate. *J.OP A:Pure Appl. Opt* 1999; 1:398-403.
60. Riser AP, Cassarly WJ. Analysis of single lens arrays using convolution., *Optical Engineering* 2001; 40:5.
61. Schreiber PP, Kudaev S, Dannberg P. Homogeneous LED-illumination using microlens arrays, [www.microoptics.org](http://www.microoptics.org)

62. Volkel R, Eisner M, Weible KJ. Miniaturized imaging systems. *Microelectronic Engineering* 2003; 67: 461–472.
63. Schreuder F, Greve J, Terstappen LWMM. A Laser Illumination System in Fluorescent Microscopy. USA patent 2006 PAN 60/800,258. 2006.
64. Cairns B, Wolf E. Changes in the spectrum of light scattered by a moving diffuser plate. *J. Opt. Soc. Am.* 1991; 8:12.
65. Suss-MicroOptics SA, neuchatel, Switzerland Technical information sheets. [www.suss-microoptics.com](http://www.suss-microoptics.com)
66. Netten H, Vliet van LJ, Boddeke FR, Jong de P, Young IT. A Fast Scanner for Fluorescence Microscopy using a 2-D CCD and Time Delayed Integration. *BioImaging* 1994; 2:184-192.
67. Yasuda N, Namiki K, Honma Y, Umeshima Y, Marumo Y, Ishiidi H, Benton ER. Development of a high speed imaging microscope and new software for nuclear track detector analysis. *Radiation Measurements* 2005; 40:311-315.
68. Schlig ES. A 3072 X 32-stage TDI imaging device. *IBM J. Res. Dev.* 1991; Vol. 35 no.112
69. Wong HS, Yao YL, Schlig ES. TDI charge coupled devices: design and applications. *IBM J. Res. Dev.* 1992; 36:83:106.
70. Stevens EG, A Unified Model of Carrier Diffusion and Sampling Aperture Effects on MTF in Solid-state Image Sensors. *IEEE transactions on electron devices* 1992; vol. 39. (Nov)
71. Fischer TA, Holm J. Electronic still picture Camera Spatial Frequency Response Measurement. *Proc. PICS Conf. IS&T* 1994; 2:626-630
72. ISO 12233 International Standard, Photography - Electronic Still Picture Cameras - Resolution measurements.
73. Burns PD, Slanted-Edge MTF for Digital Camera and Scanner Analysis, *Proc. PICS Conf., IS&T;2000;135-138*
74. Burns PD, Williams D. Using Slanted Edge Analysis for Color Registration measurements. *Proc. PICS Conf. IS&T* 1999; 51-53.
75. Burns PD, Williams D. Refined Slanted-Edge Measurements for Practical Camera and Scanner Testing. *Proc. PICS Conf. IS&T* 2002; 191-195.
76. Young IT, Gerbrands JJ, Vliet van LJ. Fundamentals of image processing, Delft University of Technology, Delft, 1995, 1-110.
77. Mullikin JC, van Vliet LJ, Netten H, Boddeke FR, van der Feltz GW, Young IT, Methods for CCD camera characterization, Image Acquisition and Scientific Imaging Systems, *Proc. SPIE* 1994, vol. 2173, 73-84.
78. Horowitz P. *The art of electronics*, 2nd edition, 1989, Cambridge University press, ISBN 0 521 37095 7.
79. Rasband WS, ImageJ, U. S. National Institutes of Health, Bethesda, Maryland, USA, <http://rsb.info.nih.gov/ij/>, 1997-2007.
80. Abramoff MD, Magelhaes PJ, Ram SJ. Image Processing with ImageJ. *Biophotonics International* 2004; Vol. 11.7:36-42.
81. Streibl N. Depth transfer by an imaging system. *Opt Acta* 1984; 31:1233–1241.
82. Young IT, Zagers R, van Vliet LJ, Mullikin J, Boddeke F, Netten H. Depth of focus in microscopy. *Proceedings SCIA'93*. Tronto, Norway 1993; 493–498.
83. Boddeke FR, Van Vliet LJ, Netten H, Young IT, Autofocusing in microscopy based on the OTF and sampling. *Bioimaging* 1994; 2:193–203.
84. Bueno-Ibarra MA. Fast autofocus algorithm for automated Microscopes. *Optical Engineering* 2005; 44(6), 063601.
85. Geusebroek J, Cornelissen F, Smeulders AWM, Geerts H. Robust Autofocusing in Microscopy, *Cytometry* 2000; 39:1–9.
86. Mason DC, Green DK. Automatic Focusing of a Computer-Controlled Microscope, *IEEE transactions on biomedical engineering* 1975; 22:4.



87. Mayeno AN, Hamann KJ, Gleich GJ. Granule-associated flavin adenine dinucleotide (FAD) is responsible for eosinophil autofluorescence. *Journal of Leukocyte Biology* 1992; 51:2.
88. Weil GJ, Chused TM. Eosinophil Autofluorescence and its Use in Isolation and Analysis of Human Eosinophils Using Flow Microfluorometry. *Blood* 1981; Vol. 57: 6.
89. Bocker W, Gantenberg HW, Muller WM, Streffer C. Automated cell cycle analysis with fluorescence microscopy and image analysis. *Phys. Med. Biol.* 1996; 41:523–537.
90. Model MA, Burkhardt JK. A Standard for Calibration and Shading Correction of a Fluorescence Microscope. *Cytometry* 2001; 44:309–316.
91. Varga VS, Boesi J, Sipos J, Csendes G, Tulassay Z, Molnar B. Scanning Fluorescent Microscopy is an Alternative for Quantitative Fluorescent Cell Analysis. *Cytometry* 2004; 60A:53–62.
92. Liao PS, Chen TS, Chung PC. A Fast Algorithm for Multilevel Thresholding. *Journal of information science and engineering* 2001; 17:713-727.
93. Landmann L. Deconvolution improves colocalization analysis of multiple fluorochromes in 3D confocal data sets more than filtering techniques. *Journal. Microscopy.* 2002;208:134-147
94. Deconvolution Recipes, Scientific Volume Imaging, Hilversum, [www.svi.nl](http://www.svi.nl)
95. Doel van den LR, van Vliet LJ, Young IT. Design Considerations for a Conventional Microscope based Microarray-Reader to Improve Sensitivity, Proc. ASCI 2001, 7th Annual Conf. of the Advanced School for Computing and Imaging (Heijten, NL, May 30-June 1), ASCI, Delft, 2001, 70-77.
96. Ortyl WE, Hall BE, George TC, Frost K, Basiji DA, Perry DJ, Zimmerman CA, Coder D, Morrissey PJ. Sensitivity Measurement and Compensation in Spectral Imaging. *Cytometry* 2006; 69A:852–862.
97. Doornbos RMP. Experimental and model investigations of bleaching and saturation of fluorescence in flow cytometry, *cytometry* 1997; 29:204-214.
98. Mathies RA, Stryer L. Single-molecule fluorescence detection: A feasibility study using phycoerythrin. In: *Applications of Fluorescence in the Biomedical Sciences*, Lansing Taylor D (ed.). Alan R Liss, NewYork, 1986, pp 129–140.
99. Mathies RA, Peck K. Optimization of High-Sensitivity Fluorescence Detection. *Anal.Chem.* 1990;62:1786-1791.
100. Wildengren J, Rigler R. Mechanisms of photobleaching investigated by fluorescence correlation spectroscopy. *Bioimaging* 1996;4:149-157.
101. Treadway JA. Focus on Detection with Qdot Conjugates, [www.Invitrogen.com](http://www.Invitrogen.com).
102. Carlsson C, Larsson A, Björkman M, Jonsson M, Albinsson B. Experimental and Simulated Fluorescence Depolarization Due to Energy Transfer Tools to Study DNA–Dye Interactions. *Biopolymers* 1998; 41:481 – 494.
103. Faris GW, Copeland RA. Wavelength dependence of the Raman cross section for liquid water. *Applied optics* 1997; 36:12.
104. Chase ES, Hoffman RA. Resolution of Dimly Fluorescent Particles: A Practical Measure of Fluorescence Sensitivity, *Cytometry* 1998;33:267–279.
105. Leers MPG, Björklund V, Björklund B, Jörnvall H, Nap M. An immunohistochemical study of the clearance of apoptotic cellular fragments. *Cell. Mol. Life Sci.* 2002;59.
106. Leers MPG. Cytokeratine en zijn afbraakproducten als potentiële aangrijpingspunten om apoptose te monitoren in patiëntenserum. *Ned Tijdschr Klin Chem* 2003;28: 20-25.
107. Ku N, Liao J, Omary MB. Apoptosis Generates Stable Fragments of Human Type I Keratins. *Journal of Bio. Chem.* 1997, 272:33197–33203.
108. Hägg M, Biven K, Ueno T, Rydlander L, Björklund P, G.Wiman KG, Shoshan M, Linder S. A novel high-throughput assay for screening of pro-apoptotic drugs. *Investigational New Drugs* 2002; 20: 253–259.

109. Schutte B, Henfling M, Kolgen W, Bouman M, Meex S, Leers MPG, Nap M, Bjorklund V, Bjorklund P, Bjorklund B, Lane EB, Omary MB, Jornvall H, Ramaekers FCS. Keratin 8/18 breakdown and reorganization during apoptosis. *Experimental Cell Research* 2004; 297:11-26.
110. Kramer G, Erdal H, Mertens HJMM, Nap M, Mauermann J, Steiner G, Marberger m, Biven K, Shoshan MC, Linder S. Differentiation between Cell Death Modes Using Measurements of Different Soluble Forms of Extracellular Cytokeratin 18. *Cancer Res* 2004;64:1751-1756.
111. Jahr S, Hentze H, Englisch S, Hardt D, Fackelmayer FO, Hesch R, Knippers R. DNA Fragments in the Blood Plasma of Cancer Patients: Quantitations and Evidence for Their Origin from Apoptotic and Necrotic Cells. *Cancer Research* 2001;61: 1659-1665.
112. Tibbe AGJ, Miller C, Terstappen LWMM. Statistical Considerations for Enumeration of Circulating Tumor Cells. *Cytometry* 2007; 71A:154-162.
113. Netten H, Young IT, Vliet van LJ, Tanke HJ, Vrolijk H, Sloos WCR. FISH and Chips: Automation of Fluorescent Dot Counting in Interphase Cell Nuclei *Cytometry* 1997; 28:1-10.
114. Nederlof PM, Flier van der S, Vrolijk J, Tanke HJ, Raap AK. Fluorescence Ratio Measurements of Double-Labeled Probes for Multiple In Situ Hybridization by Digital Imaging Microscopy. *Cytometry* 1992;13:839-845.
115. Wiegant J, Bezroukove V, Rosenberg C, Tanke HJ, Raap AK, Zhang H, Bittner M, Trent JM, Meltzer P. Differentially Painting Human Chromosome Arms with Combined Binary Ratio-labeling Fluorescence In Situ Hybridization. *Genome Res.* 2000;10:861-865.
116. Jaiswal JK, Simon SM. Potentials and pitfalls of fluorescent quantum dots for biological imaging. *TRENDS in Cell Biology* 2004;14:9.
117. Wu X, Liu H, Liu j, Haley KN, Treadway JA, Larson JP, Ge N, Peale F, Bruchez MP. Immunofluorescent labeling of cancer marker Her2 and other cellular targets with semiconductor quantum dots. *Nat. Biotechnol* 2003; 21:41-46.
118. Neher R, Neher E. Optimizing imaging parameters for the separation of multiple labels in a fluorescence image. *Journal of Microscopy* 2004; 213:46-62.
119. Zimmermann T, Rietdorf J, Rainer Pepperkok R. Spectral imaging and its applications in live cell microscopy. *FEBS Letters* 2003 ; 546:87-92.
120. Gammon ST, Leevy WM, Gross S, Gokel GW, Piwnica-Worms D. Spectral unmixing of multicolored bioluminescence emitted from heterogeneous biological sources. *Anal Chem.* 2006; 78:1520-7.
121. Nagy P, Friedlander E, Tanner M, Kapanen AI, Carraway KL, Isola J, Jovin TM. Decreased Accessibility and Lack of Activation of ErbB2 in JIMT-1, a Herceptin-Resistant, MUC4-Expressing Breast cancer Cell Line. *Cancer Res* 2005; 65:2.
122. Akewanlop C, Watanabe M, Singh B, Walker M, Kufe DW, Hayes DF. Phagocytosis of Breast Cancer Cells Mediated by Anti-MUC-1 Monoclonal Antibody, DF3, and Its Bispecific Antibody. *Cancer Research* 2001;61:4061-4065.

# Summary

Cancer is frequently identified at a late stage of the disease and it is difficult for oncologists to stipulate the best strategy with regard to treatment. The current detection methods are frequently based on radiographic imaging which indicate the increase and changes of a tumor over a long time span. This does not give the possibility to evaluate quickly whether the treatment is effective and does not give information regarding treatment targets expressed on the tumor. This specificity is necessary for the treatment with specific targeted therapies. Therefore a biopsy should still be obtained from the primary tumor. However repeated evaluation is desired, tumor cells are genetically unstable, and this can quickly lead to mutations and result in resistance to treatment. A new technique which can give all kinds of specific information on the tumor on a regular basis would be a valuable tool. A potential technique is circulating tumor cell (CTC) detection. This technique enumerates and characterizes tumor cells in a blood sample. These tumor cells (CTCs) that entered the blood stream, may result in metastasis, which frequently leads to death. The problem regarding CTC detection is their inherent low occurrence. This requires enrichment of the blood sample and a very precise and accurate detection method to trace a single tumor cell, in a couple milliliter of blood.

In this thesis the development of a new instrument called the “CellTracks TDI” is described. This instrument is specifically developed to improve the enumeration and characterization of magnetically enriched CTC samples. We used a magnetic enrichment method protocol developed by Immunicon.

Chapter 1 gives a general introduction. The characteristics concerning CTC detection and the possibilities of the current analysis techniques are discussed. Although current equipment is capable of analyzing CTC samples, it still has some disadvantages and can be improved further. Specifically it is desired to have a system that scans a sample very fast and measures several markers with a higher resolution and sensitivity.

This has lead to an instrument which scans a CTC sample using a TDI camera and a 40X 0.6NA objective. A complete description of the optics and used hardware has been given in chapter 2.1. The TDI operation of the camera makes it possible to acquire the fluorescence images in a continuous motion and therefore it minimizes acquisition time. For excitation several laser lines have been used, where laser light has been homogenized to produce a flattop profile with the use of micro lens arrays.

Chapter 2.2 describes the analysis of the data and the automated control of the system. This is necessary to obtain a complete sample scan automatically and consistently. Furthermore it reduces the large quantities of data to obtain useful information.

In chapter 2.3 the characterization of the system is described. The different properties of the system and the CTC samples such as noise, dynamic range, bleaching, sensitivity, scan times and specificity have been evaluated to characterize the system.

Blood samples of 26 metastatic carcinoma patients have been examined for CTCs by both the CellTracks TDI and the commercial CellTracks Analyzer II. This has been described in chapter 3.1 and the results showed a good correlation between both systems. The results furthermore show that the higher resolution of the CellTracks TDI makes apoptotic characteristics of the CTCs better visible. Moreover our new system also measures small fragments originating from tumor cells. The relatively large quantities and the correlation with the intact CTCs indicate that enumeration of these particles may have diagnostic potential. This may lead to an instrument which is able to detect the presence of tumor cells in an earlier stage of the disease. Currently detection is limited to the amount of blood that can be drawn from a patient.

A possibility to analyze tumor cells in more detail is described in chapter 3.2. After initial detection, events of interest were selected and revisited. Prior to the second reexamination step the cells are labeled with FISH probes to evaluate chromosomal alterations.

In chapter 3.3 we presented the first experiments of cells labeled with Qdots. Specific tumor markers Her2/nue and MUC-1 were conjugated with Qdots and were detected with the CellTracks TDI. Use of the Qdots for the current CTC assay can be an attractive alternative to extend the number of probes that can be assessed. It however requires further optimization of the labeling protocol.

A final conclusion and remarks concerning the CellTracks TDI are given in chapter 4. Followed by an outlook for possible improvements and new experiments to further extend and optimize CTC detection.

# Samenvatting

Kanker wordt vaak in een te laat stadium gesignaleerd en het is voor oncologen moeilijk te bepalen wat de beste strategie is voor behandeling. De huidige detectie methoden zijn vaak gebaseerd op beeldvormende technieken, die geven gedurende langere periodes de groei en veranderingen van een tumor aan. Dit geeft niet de mogelijkheid om in een kort tijdsbestek te bepalen of de behandeling effectief is. Tevens geeft het geen informatie over de eventuele expressie van tumor gerelateerde receptoren, wat de mogelijkheid biedt voor specifiek gerichte behandeling methodes. Een biopsie van de tumor is hiervoor noodzakelijk, dit is echter een moment opname. Tumorcellen zijn genetisch niet stabiel en dit kan leiden tot resistentie en mutaties gedurende de behandeling. Een nieuwe techniek die met grote regelmaat allerlei specifieke informatie over de tumor kan geven, zou dan ook een waardevolle toevoeging zijn. Een potentiële techniek hiervoor is Circulerende Tumor Cel (CTC) detectie. Deze techniek meet de aantallen en eigenschappen van eventuele tumor cellen in een bloed sample. Deze tumor cellen (CTCs) die in de bloedbaan zijn gekomen, kunnen mogelijk uitzaaiing tot gevolg hebben, wat vaak leidt tot het overlijden van de patiënt. Het probleem voor detectie is echter dat deze cellen in zeer lage concentraties voorkomen. Dit vereist verrijking van het bloed sample en een zeer nauwkeurige detectie methode om een enkele tumorcel, in een paar milliliter bloed te kunnen traceren.

In dit proefschrift wordt de ontwikkeling van een nieuw instrument de “CellTracks TDI” beschreven. Dit instrument is speciaal ontwikkeld om de magnetisch verrijkte CTC samples beter te kunnen analyseren. Hierbij is gebruik gemaakt van een magnetisch verrijking methode zoals deze is ontwikkeld door Immunicon.

Hoofdstuk 1 geeft een algemene introductie. De kenmerken betreffende CTC detectie en de mogelijkheden van de huidige bloedanalyse apparatuur worden besproken. Hoewel de huidige apparatuur instaat is om CTC samples te analyseren heeft deze toch enkele nadelen. Het is namelijk gewenst, om zeer snel, voor meerdere markers, met een hoge resolutie en gevoeligheid te meten, om zo tot een betere karakterisering van een CTC te komen.

Dit heeft geleid tot het maken van een instrument dat een CTC sample scant met behulp van een 40X 0.6NA objectief en een TDI camera. De optica en gebruikte hardware zijn beschreven in hoofdstuk 2.1. Hierbij wordt het fluorescentiesignaal vergaard, met een constante beweging, om zo doende de scan tijd te minimaliseren. Meerdere laserlijnen zijn gebruikt voor de excitatie, hierbij is het laserlicht gehomogeniseerd in een vierkant vlak met behulp van micro lens arrays.

Een belangrijk aspect zoals beschreven in hoofdstuk 2.2 is de analyse van de data, en de geautomatiseerde aansturing van het instrument. Dit is noodzakelijk om een compleet sample automatisch en consistent te scannen. Tevens is beschreven hoe de grote hoeveelheden verkregen data, uiteindelijk gecondenseerd zijn tot bruikbare informatie.

In hoofdstuk 2.3 worden de verschillende eigenschappen van het systeem en de CTC samples beschreven. Eigenschappen zoals ruis, dynamisch bereik, bleking, gevoeligheid, nauwkeurigheid, scantijden en specificiteit zijn bepaald om het systeem te karakteriseren.

Bloed samples van 26 patiënten met een gemetaseerd carcinoom zijn onderzocht voor CTCs. Als vergelijk zijn de metingen uitgevoerd op twee systemen. Ons nieuwe systeem de CellTracks TDI en de commerciële CellTracks Analyzer II. Dit is beschreven in hoofdstuk 3.1 en toonde een goede correlatie aan, tussen beide systemen. De hogere resolutie van de CellTracks TDI maakt echter ook apoptotische kenmerken van de CTCs beter zichtbaar. Daarnaast meet ons nieuwe systeem ook allerlei kleine fragmenten afkomstig van de tumor cellen. De relatief grote hoeveelheden en de correlatie met de intacte CTCs, geven aan dat de bepaling van deze deeltjes misschien wel een waardevolle toevoeging kunnen zijn. Dit zou kunnen leiden tot een systeem dat reeds in een vroeger stadium, de aanwezigheid van tumorcellen kan detecteren. De detectie limiet is namelijk beperkt tot de hoeveelheid bloed die redelijkerwijs afgenomen kan worden.

Een mogelijkheid om tumor cellen in meer detail te analyseren wordt beschreven in hoofdstuk 3.2. Na de eerste detectie, zijn de geselecteerde cellen hierbij twee keer opnieuw geanalyseerd. Waarbij in de tweede stap de cellen opnieuw gelabeld worden maar nu met een FISH label, om chromosoom afwijkingen te bepalen.

In hoofdstuk 3.3 zijn de eerste resultaten gepresenteerd om cellen te labelen met Qdots en deze vervolgens te detecteren met de CellTracks TDI. Hierbij zijn de specifieke tumor markers Her2/nue en MUC-1 geconjugeerd met Qdots. Dit vereist echter nog verdere optimalisatie, maar kan zeker een goed alternatief zijn om meerdere markers te detecteren.

Een definitieve conclusie en opmerkingen betreffende de CellTracks TDI wordt gegeven in hoofdstuk 4. Aansluitend worden de vooruitzichten voor mogelijke verbeteringen en nieuwe experimenten besproken om CTC detectie verder uit te breiden en te optimaliseren.

# Nawoord

Eindelijk is het dan zover, na een periode van 4,5 jaar onderzoek binnen de BPE (Biophysical engineering) zijn dit de laatste loodjes van mijn proefschrift.

Tevens is het ook een afronding van een aantal maanden schrijfwerk. Dit was voor mij niet de makkelijkste periode. Gelukkig geeft het uiteindelijk wel heel veel voldoening om tot een afgerond proefschrift te komen. Een proefschrift met de resultaten van een interessant en leuk onderzoek waar ik met heel veel plezier al die jaren aan gewerkt heb. Een dergelijk onderzoek doe je natuurlijk niet helemaal alleen, en ik wil dan ook een aantal mensen bedanken die hebben geholpen met het tot stand komen van dit proefschrift. Allereerst wil ik mijn twee promotoren Jan en Leon bedanken. Jan, jouw enthousiasme en interesse voor de cytometrie werken zeer aanstekelijk. Bedankt! Ook wil ik Leon bedanken als begeleider in de laatste periode van mij promotie en voor de nodige kennis over tumor cellen. Daarnaast natuurlijk het cytometrie groepje samen met Lilly, Aurel, Christiaan, Sjoerd en Tycho wat altijd zeer gezellig was. De nuttige discussies en kritische kanttekeningen gedurende de werkbeprekingen waren zeer leerzaam en hebben me altijd ontzettend gestimuleerd. In het bijzonder wil ik Tycho en Sjoerd bedanken. Tycho onze groeven man, was altijd wel in voor een leuk experimentje en we vulden elkaar daarbij goed aan. Bedankt! Sjoerd, wil ik bedanken voor het implementeren van de deconvolutie software tijdens zijn afstuderen. Dat leverde toch maar weer mooie plaatjes op die gretig aftrek vonden bij Jan en Leon. Voor mooie plaatjes heb je natuurlijk wel cellen nodig. Yvonne wilde altijd met veel plezier een slachtoffer voor me prikken en voor het kweken van de tumor cellen kon ik altijd bij Wilma terecht. Bedankt. Wat betreft de koffie, gezellige gesprekken en de verschillende hand-en spandiensten mag ik Frans en Sylvia natuurlijk niet vergeten. Al die jaren heb ik dan ook met heel veel plezier gewerkt en ik wil hiervoor alle BPE'ers bedanken voor de leuke gesprekken en prettige sfeer binnen de groep.

Daarnaast wil ik ook de mensen van Immunicon bedanken voor de goede samenwerking. Arjan, die ten eerste mijn begeleider was tijdens mijn afstuderen en mij later ook de mogelijkheid gaf om de nodige CTC samples te kunnen meten. Bedankt! Voor de nodige experimenten met de FISH probes wil ik vooral Joost ontzettend bedanken.

Tenslotte, wil ik mijn vader en moeder bedanken voor de kans die ze me hebben gegeven om te studeren en tevens ook verdere familie bedanken voor de nodige steun en interesse. Als laatste, maar zeker niet de minste wil ik Nienke bedanken voor alle steun, liefde en bemoedigende woorden.

Erik.





# Curriculum Vitae

Frederik Schreuder (Roepnaam Erik) geboren op 4 november 1975 te Rijssen. In 1993 behaalde hij zijn MAVO-diploma aan het CSG Reggesteyn te Rijssen. Vervolgens deed hij een proces techniek opleiding (MTS) aan het Dr. D.H. Groen College te Almelo, die hij in 1996 met gunstig gevolg afsloot. Aansluitend hierop begon hij de studie technische natuurkunde aan de HTS “Hogeschool Enschede” te Enschede. Na het behalen van de propedeuse in 1997 zette hij zijn studie technische natuurkunde voort aan de Universiteit Twente. In het kader van deze opleiding werd een stage gelopen bij Abbott Laboratories Diagnostics division, Santa Clara, USA en heeft hij een optisch instrument gebouwd voor het meten van hemoglobine concentraties. Bij de leerstoel Biophysical engineering (BPE), onder leiding van Prof. Dr. J. Greve verrichte hij zijn afstudeeropdracht op het gebied van cytometrie en behaalde in 2003 zijn doctoraal diploma. Aansluitend begon hij een promotie onderzoek aan het CellTracks project in samenwerking met Immunicon Corporation (Huntingdon Valley, PA, USA) onderleiding van Prof. Dr. J. Greve en Prof. dr. L.W.M.M. Terstappen. Het promotie onderzoek betrof de ontwikkeling van een image cytometer voor het karakteriseren van circulerende tumor cellen in bloed. De resultaten van dit werk zijn beschreven in dit proefschrift.